Design of elemental nanoparticles and their application in catalysis, lithography and biochemistry

by

Chiara Fasciani

Thesis submitted to the
Faculty of Graduate and Postdoctoral Studies
In partial fulfillment of the requirements for the degree of
Doctor in Philosophy in Chemistry

Ottawa-Carleton Chemistry Institute
Center for Catalysis Research and Innovation
Department of Chemistry, University of Ottawa

Université d'Ottawa – University of Ottawa

Candidate	Supervisor
Chiara Fasciani	Professor J. C. Scaiano

“Non e`, pei chimici
che un vago Au:
ma in questo simbolo
quante virtu`.

Si trova libero
L’oro in natura:
da sabbie aurifere
lo si depura.

Di cloruro aurico
la soluzione
nei corpi organici
si decompone;

e` riducibile
agevolmente,
rosso solubile
deliquescente,

ed anche in seguito
a calor lento
l’oro deposita
polverulento.

Questo la chimica
dice. Io vi dico
che l’oro e` l’unico
sincero amico;

che’e` d’ogni spirito
l’unica meta;
che per disgrazia
non l’ha il poeta

che` se al contrario,
ne avesse a iosa,
certo la chimica…
*restava in prosa!”**

Insieme all’oro
c’e` anche l’argento,
che di questa tesi
son argomento.

L’applicazione
con luce solare,
non e` magia! Ma,
e` a dir poco esemplare:

centinaia di Celsius
si posson ottenere
dopo che il Plasmon
si fa decadere.

Soli lor posson
catalizzare
processi termici,
per cominciare.

Nello specifico
per dirne una,
posson produrre
resorufina.

Ma anche quando
si metton insieme
oro e argento
lavoran bene!

Carbonio infine,
da meno non e`,
diamante o grafene
anche lui ha un perche`.

Graphene in ossido,
elettron trasporta
con argento e oro
non ugual si comporta.

Infin col laser
diventa rotondo.
Forse, energia
produrrà per il mondo!

Quanto descritto
m’ha affascianto
durante questi anni
di dottorato.

Se ti interssa
saperne di più
tutto ciò troverai
in prosa più giu`…

*The first column was taken from “*La chimica in versi*”* Alberto Cavaliere (1928). The last two columns have been inspired by this PhD work.

Abstract

The interest in metal nanoparticles has seen an exponential growth in the last twenty years, due to the astonishing properties these materials possess on the nanometer size scale. Compared to the bulk metal, nanoparticles present different optical and physical properties, which can be tuned according to their size or shape. As an example, colloidal solutions of 15 nm gold nanoparticles appear red, a very different tint as compare to the typical gold color of a gold brick. The reason for this variation is due to the fact that visible light wavelengths are bigger than the nanoparticles sizes. Therefore, after excitation, part of the light is absorbed and produces a coherent oscillation of the surface electrons, resulting in a phenomenon known as surface plasmon resonance. At this point the system tends to return to the initial state, following different pathways. One of the processes occurring is the local release of heat around the nanoparticle surface.

The aim of this thesis is to gain more insight into the actual temperature values achievable after plasmon irradiation and to explore the possible applications of the localized heat release. Synthetic procedures developed in the Scaiano group were used to synthesize and modify the nanoparticles. The applicability of these photochemical procedures was extended to the synthesis of bimetallic silver-gold (Ag/Au) core-shell materials *via* a controlled and facile synthesis method. Ag/Au core-shells combine the optical and physical properties of gold and silver together and they have shown promise as potential antimicrobial agents.

Information regarding the temperatures achievable after plasmon excitation has been obtained using dicumyl peroxide as a molecular thermometer and has indicated temperatures close to 500ºC near the nanoparticle surface. This finding was a precious guideline for the selection of thermal processes that can be performed after plasmon excitation. The catalytic reduction of resazurin to resorufin was one of the reactions chosen. This process, indeed, appears significantly faster (nanoseconds) when performed using AuNP irradiated at 530 nm.

The use of laser and LED irradiations has been a constant throughout this work with both systems being to suite the experimental needs.

The high temperature reached irradiating metal nanoparticles has also been used to

trigger the caprolactam polymerization, in such a way that only in the light exposed position AgNP favored nylon formation, presenting promising applications in lithography.

Moreover, DNA melting processes have been successfully studied, by employing a switch On/Off controllable irradiation of AuNP, aiming for eventual application in the polymerase chain reaction (PCR) process.

Finally, considerable work has been done in the functionalization and modification of carbon-based materials. Functionalization with silver and gold nanoparticles has been performed using a photochemical procedure, during which a different behavior was observed for the two metals. In addition, modification of the reduced graphene oxide morphology was obtained by laser irradiation without the use of any external template. The spherical reduced graphene oxide, thus obtained, has shown promising potential in water splitting catalysis. In this system, the evolution of hydrogen was observed by employing only spherical reduced graphene oxide and visible light (532 nm laser or LED irradiation).

In summary, this thesis describes how light can not only be used to synthesize and modify nanomaterials, but also to perform high energetic processes at room temperature, taking advantage of the nanoscale properties of the materials being used.

Acknowledgements

In the last four years I have been so lucky to know and work with very special persons, whom have taught me a lot about science, chemistry and above all life. First of all, I want to say thanks to Tito for being such a great supervisor and person. He welcomed me in his group and helped me during this beautiful adventure. His curiosity and interest for science made me love chemistry even more then before. I will never forget our long discussions about family, career and life and I will try to follow your advice: "You need to let you private life interfere with your career". I want to thank Tito and Elda also for their hospitality during the camping/ski weekends at their cottage; I will definitively miss their barbeques!

Thanks to all the Scaiano group actual and previous members, each of them left something in my memory and contributed to make this experience unforgettable. Thanks to the patience of Betty Yakimenko for whom I was the "special case" with all the bureaucratic complications. Thanks to Michel Granier for sharing with me his beautiful pictures and for helping me with all my laser/LED requests.

During these four years, Tito offered me the occasion of visiting different international laboratories and I will always be grateful for that. In those occasions I had the chance to keep alive my love for traveling and to know remarkable scientists/friends. For this reason, I want to thank Prof. Hermenegildo Garcia and Prof. May Griffith, from Instituto de Tecnologia Quimica (Spain) and Linkoping Universitate (Sweden) respectively and their group members, which are now good friends. Both have been experiences that I will never forget.

In addition to the real travels, I have got the opportunity to get to know a little more the world just being part of Tito's group and meeting people coming from very different countries. Thank you all for sharing with me your traditions, culture and experiences.

Moreover, I really want to thank this beautiful country, which is Canada, for being such a charming, welcoming and multicultural place.

A special thank goes to my friends, those that I left back home, those that I met here in Canada and those that wherever they are, I feel their support and friendship.

Thanks to my mom Angela, my sister Martina, nonno Elio, nonna Giovannina and all my

family for being always at my side and trusting me in every decision I take. They are the best present I have got in my life! Thanks to Marco for teaching and proving me how an ocean can be small as a puddle when you love somebody.
Finally, I want to thank and dedicate this thesis to my beloved uncle Marco who I felt and keep feeling always close to me. He encouraged me to come to Canada, both as a professional and personal experience, and to feed my curiosity in life. I will always be grateful for that and for all you gave us during your short existence.

Thank you all!

Table of Contents

List of Figures

partial pressures of an air sample (first column); after 30 min + 30 min of laser irradiation (532 nm) of rGO (second column); after 30 min + 30 min of LED irradiation (532 nm) of rGO (third column); and after consecutive 30 min laser irradiation (532 nm) and 30 min LED irradiation (532 nm) of a rGO dispersion in $H^{18}O$ (fourth column). The values are obtained comparing the areas of traces referred to each gas detected to the area of the trace relative to water vapor and multiplying the value obtained for the water partial pressure (3.2 KPa) at 25ºC. 163

List of Schemes

List of Tables

List of Abbreviations

AFM	Atomic Force Microscopy
AgNP	Silver Nanoparticles
APTES	3-Aminopropyltriethoxysilane
AuNP	Gold Nanoparticles
CHA	Cyclohexylamine
CuNP	Copper Nanoparticles
DCP	Dicumyl Peroxide
DLS	Dynamic Light Scattering
DNA	Deoxyribonucleic Acid
dsDNA	Double Strain Deoxyribonucleic Acid
EDC	1-Ethyl-3-(3-dimethylaminopropyl) Carbodiimide
EDS	Energy Dispersive X-Ray Spectroscopy
Et_3N	Triethylamime
FLIM	Fluorescent Lifetime Imaging Microscopy
G	Graphene
GO	Graphene Oxide
GB	Gain in Brightness
GC-MS	Gas Chromatograph Mass Spectroscopy
GC-TCD	Gas Chromatograph-Thermal Conductivity Detector
4-HEBA	4-Hydroxyethoxy Benzoic Acid
HPLC	High-Pressure Liquid Chromatography
HRTEM	High-Resolution Transmission Electron Microscope
I-2959	1-[4-(2-hydroxyethoxy)phenyl]-2-hydroxy-2-methyl-1-propane-1-one, or Irgacure-2959
K_{sv}	Stern-Volmer Constant
k_q	Quenching Rate Constant

λ	Light Wavelength
LCST	Lower Critical Solution Temperature
LED	Light Emitting Diode
MB	Methylene Blue
MeOH	Methanol
MES	2-(*N*-Morpholino)Ethanesulfonic Acid
MIC	Minimum Inhibitory Concentration
n	Refractive Index
Nd:YAG	Neodymium-Doped Yttrium Aluminum Garnet
NP	Nanoparticles
PBS	Phosphate Buffered Saline
PCeT	Proton Coupled Electron Transfer
PCR	Polymerase Chain Reaction
PDEAM	Poly(N,N-diethylacrylamide)
PMMA	Poly(methyl methacrylate)
PNIPAM	Poly(N-isopropylacrylamide)
QMS	Quadrupole Mass Spectrometer
RBEI	Rutherford backscattered electron imaging
rGO	Reduced Graphene Oxide
SEI	Secondary Electron Imaging
SEM	Scanning Electron Microscopy/Micrograph
SERS	Surface-Enhanced Raman Scattering
SPR	Surface Plasmon Resonance
ssDNA	Single Strain Deoxyribonucleic Acid
STEM	Scanning Transmission Electron Microscope
sulfo-NHS	Sulfo-*N*-Hydroxysulfosuccinimide
τ	Fluorescence Lifetime

TED	Transmission Electron Detector
TEM	Transmission Electron Microscopy/ Micrograph
TIRF	Total Internal Reflection Fluorescence Microscopy
UCST	Upper Critical Solution Temperature
UVA	Ultraviolet Irradiation ranging from 315-400 nm
UVB	Ultraviolet Irradiation ranging from 280-315 nm
UVC	Ultraviolet Irradiation ranging from 100- 280 nm
UV-vis	Ultraviolet-Visible Irradiation

0.1 Contribution Statement

The projects presented in this thesis are the result of the work I have done under the membership of Professor Scaiano, whom has guided me throughout my PhD but whom also has given the required freedom to develop my scientific critical attitude. Being part of a big group consists in the possibility of exchanging ideas and having constructive confrontation. Therefore, this work is the outcome of a continuous brainstorming within the Scaiano group. In this section I want to highlight my direct contribution in addition to the contributions of my coworkers in each of the project presented.

The dicumyl peroxide project and the resazurin reduction were investigated in collaboration with Carlos Bueno-Alejo, a previous post-doc fellow in the Scaiano's group. We constantly worked and discuss together about the different systems which could possible furnish information about the plasmon heating.

The synthesis of silver/gold core shells using our photochemistry procedure was a fortunate finding resulted by an experiment driven by my curiosity. A previous member of the Scaiano group, Kathy McGilvray had studied a similar procedure for the controlled growth of individual AuNP. Therefore, the two projects became part of the same publication although independently developed.

The caprolactam polymerization using AuNP was an idea I had teaching an undergraduate course about polymers. After shearing my idea with Professor Scaiano, he suggested to use it for lithographic application. Kevin Stamplecoskie, a previous PhD student in our group, had at that time developed a methodology to trigger a radical polymerization using AgNP. This procedure was lacking of the spatial precision required in lithography, therefore, as Kevin used to say, I provided the missing piece of the puzzle.

DNA melting project was an ambitious work that started after instances conversation with Emilio Alarcon, a post-doc fellow in the Scaiano group. Important contributions to this work were given by Hasita Weerasekera, as part of his honor project and by Sabrina Simoncelli, who was our FLIM/TIRF expert.

The investigation of carbon-based materials and resulting projects were stimulated by the collaboration with Prof. Hermengildo Garcia and his group in Valencia, where I spent three months. The chemical modification and the morphological changes were all ideas that I independently developed however, Prof. Garcia's group provided the materials and Prof. Javier Giorgi helped in the analysis of the gas released after graphene irradiation.

The peer reviewed contributions coming from this thesis work are listed here, a separate section is reported after, indicating the projects not presented in this thesis.

Publication resulting from the work presented in this thesis:

1. **Chiara Fasciani,** Carlos J. Bueno Alejo, Michel Grenier, Jose` Carlos Netto-Ferreira, J. C. Scaiano; High-Temperature Organic Reactions at Room Temperature Using Plasmon Excitation: Decomposition of Dicumyl Peroxide, *Organic Letters*, **2011**, 13, 204-207.

2. Carlos J. Bueno Alejo, **Chiara Fasciani**, Michel Grenier, Jose` Carlos Netto-Ferreira, J. C. Scaiano; Reduction of Resazurin to Resorufin Catalyzed by Gold Nanoparticles: Dramatic Reaction Acceleration by Laser or LED Plasmon Excitation, *Catalysis Science and Technology*, **2011**, 1, 1506-1511.

3. Kevin Stamplecoskie, **Chiara Fasciani**, J. C. Scaiano; Dual-stage Sub-wavelength Lithographic Features from a Light Driven, Plasmon Assisted Process: A Hierarchical Approach to Subwavelength Features, *Langmuir*, **2012**, 28, 10957−10961.

4. Katherine L. McGilvray*, **Chiara Fasciani***, Carlos J. Bueno-Alejo, Rachel Schwartz-Narbonne and Juan C. Scaiano; Photochemical Strategies for the Seed-Mediated Growth of Gold and Gold-Silver Nanoparticles, *Langmuir*, **2012**, 28, 16148−16155. (*equal contribution)

5. Sabrina Simoncelli, Hasita Weerasekera, **Chiara Fasciani**, Christopher Boddy, Pedro Aramandia, Emilio I. Alarcon, Juan C. Scaiano; Thermoplasmonic ssDNA Dynamic Release Revealed with High Resolution Level. (In preparation)

6. **Chiara Fasciani**, Hermengildo Garcia, Juan C. Scaiano; Selective Growth of Silver Nanoparticles on Graphene Oxide Mediated by Proton-Coupled Electron Transfer (PCeT). (In preparation)

7. **Chiara Fasciani**, Javier Giorgi, Hermengildo Garcia, Juan C. Scaiano; Morphological Modification of Reduced Graphene Oxide Sheets Using Visible Light. (In preparation)

Publication resulting from work not presented in this thesis:

1. (alphabetical after professors) J.C. Scaiano, Jose` Carlos Netto-Ferreira, Emilio Alarcon, Paul Billone, Carlos J. Bueno Alejo, Charles-Oneil L. Crites, Matthew Decan, **Chiara Fasciani**, Mara Gonzalez-Bejar, Geniece Hallett-Tapley, Michel Grenier, Katherine L. McGilvray, Natalia L. Pacioni, Andrea Pardoe, Laetitia Rene-Boisneuf, Rachel Schwartz-Narbonne, M. Jazmin Silvero, Stamplecoskie, K.G. and Tse-Luen Wee; Tuning Plasmon Transition and their Applications in Organic Photochemistry, *Pure and Applied Chemistry*, **2011**, 83(4), 913-930.

2. Christopher McTiernan, **Chiara Fasciani**, Maria Gonzalez-Bejar, Daniel Roca, Emilio Alarcon, Jose` C. Netto-Ferreira; Ketorolac Beats Ketoprofen: Lower Photodecarboxylation, Photohemolysis and Phototoxicity, *Medicinal Chemistry Communications*, **2013**, 4, 1619-1622.

3. M. Luisa Marin, Geniece L. Hallett-Tapley, Stefania Impellizzeri, **Chiara Fasciani**, Sabrina Simoncelli, Jose Carlos Netto-Ferreira, Juan C. Scaiano; Synthesis, Acid Properties and Catalysis by Niobium Oxide Nanostructured Materials. (submitted)

4. **Chiara Fasciani**, Alexandra Anghel, Jazmin Silvero, Juan C. Scaiano Gold-Silver Hybrid Nanostructures Stabilized with Aspartame Show Antibacterial Properties that can Be Enhanced through Visible Light Irradiation. (In preparation)

5. **Chiara Fasciani,** Christopher McTiernan; Geniece L. Hallett-Tapley, Carlos J. Bueno Alejo, Juan C. Scaiano Efficient Oxidation of Aromatic Alcohols by Gold Nanoparticles Supported on nano-ZnO under Dark Conditions. (In preparation)

Chapter 1

Introduction

1.1 Metal nanoparticles from theory to application

Metal nanoparticles, such as those of Au, Ag and Cu, have been increasingly studied in the last few years due to their unique spectroscopic properties and potential applications. Commonly, nanoparticles are defined as a small cluster of atoms going from less than 100 atoms (~1 nm) to hundreds of thousands atoms (~100 nm). Usually known as "colloids",[1] nanoparticles have been used in glasses and ceramics since the Roman Empire. The Lycurgus cup represents one of the most famous examples of gold-silver colloidal nanoparticles used to create interesting optical effects in glasses (Figure 1.1). The color of the cup changes according to the light source: yellow-green when not illuminated and red when visible light is shined through the glass. Au-Ag colloids have also been employed during the Middle Age and Renaissance in stained glasses and pottery.[2] In 1857, Faraday published a contribution in which he recognized that the red color of colloidal gold derives from small aggregates of gold atoms.[3] Unfortunately,

electron microscopy techniques where not yet available and, therefore, no precise indication of the aggregate sizes could be obtained. Despite the fact that the use of nanosize materials has been known for centuries, nanotechnology officially became a new discipline after Richard Feynman's famous lecture in 1959. Feynman, at that time, was a physicist at Caltech and with the memorable sentence "*There's plenty of room at the bottom*" he forecasted the need of exploring the "nano-world" towards future technology and advancement.[4]

Figure 1.1 Lycurgus Cup dated during the 4th century AD. The cup presents a red tint (right) when light shines through the glass from the inside, it appears green (left) when the light is coming from the outside. [Pictures taken from the British Museum website: www.britishmuseum.org]

The revolutionary prospective opened by nanotechnology is derived from the fact that, at these dimensions, the properties and the behavior of materials change drastically compared to the same material on the macroscopic scale. The reduction of the material size has a considerable effect on the energy levels, meaning that the energy level distances increase by decreasing the material dimensions. Nanoparticles, indeed, can be considered as a *trait-d'union* between atomic and molecular structures. Unexpected properties arise when the material is in the nanosize. For example, some metals become semiconductors, other fluorescent. In the case of metal nanoparticles, such as AuNP, AgNP or CuNP, their small dimension gives rise to quantum effects due to electron confinement. When visible light is shined on metal nanoparticles, the electric field

induces a coherent oscillation of the surface electrons and the resulting phenomenon, surface plasmon resonance (SPR), is observed (Figure 1.2).

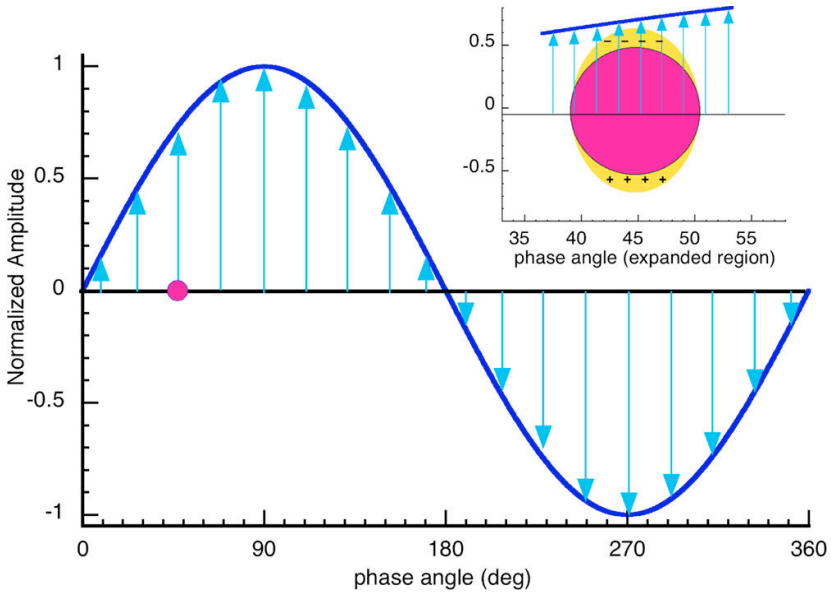

Figure 1.2 Schematic scale representation of a 20 nm metal nanoparticle under the effect of an electromagnetic wave of 530 nm. [Figure reproduced from ref. 5]

The origin of the bright colors of noble metal nanoparticle solutions is in fact determined by this specific phenomenon, as a consequence of the smaller size of the nanoparticle compared to the wavelength of the light used. Representative absorbance spectra for spherical AuNP, AgNP and CuNP in water are reported in Figure1.3. Variation of the absorption wavelength maxima can be obtained by changing the size or the shape of each metal nanoparticles, as will be described in the following discussion.

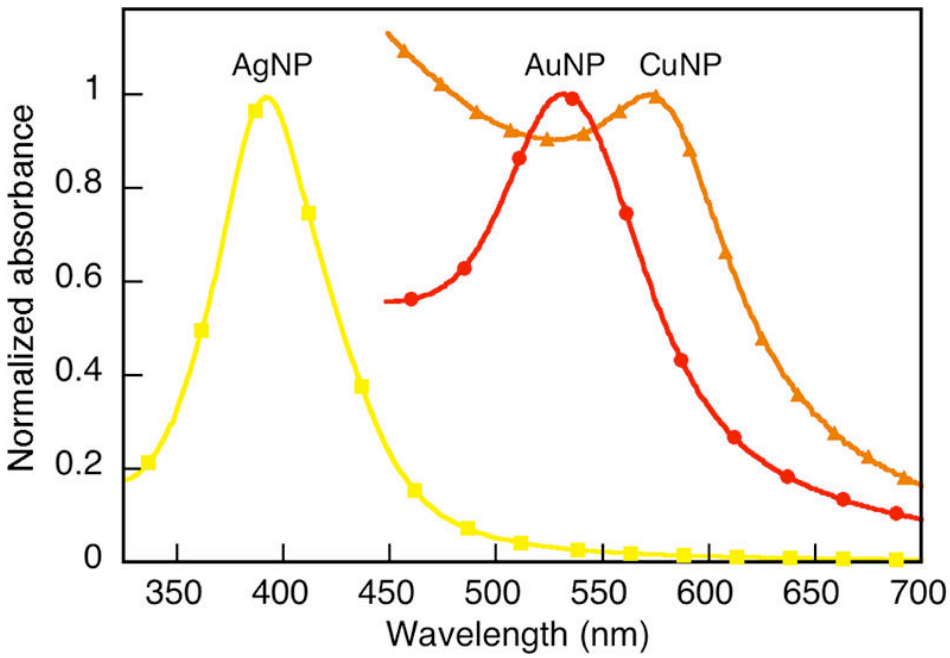

Figure 1.3 Representative SPB absorbance spectra for spherical AgNP, AuNP, and CuNP in water. [Figure reproduced from ref. 5]

The first to explain the origin of the SPR was Gustav Mie in 1908.[6] He considered the dipolar modes of spherical particles interacting with an electromagnetic light wave in homogeneous dielectric materials and solved the Maxwell's equations for this system. As a result of this calculation, the ability to absorb light, or polarizability (α), of a metal nanoparticle can be expressed as in equation 1.1:

$$\alpha = 3\varepsilon_0 V \frac{\varepsilon - \varepsilon_m}{\varepsilon + 2\varepsilon_m} \qquad (1.1)$$

where ε_0 is the permittivity in the vacuum, V is the volume of the particle, ε is the permittivity of the material and ε_m is the permittivity of the medium surrounding the particle. Resonance of the surface electrons and the SPR occurs when $\varepsilon \approx -2\varepsilon_m$. This dipolar approximation is valid for spheres and fails when considering big particles or different shapes. In these cases, more complex calculations are required.[7] The polarizability, expressed according to the previous equation, is comprised of absorption and scattering contributions. The absorption is due to collisions between oscillating

electrons, while the scattering is due to the light trajectory deviation resulting after interaction with a certain object, without the lost of energy. The total extinction can be expressed as:

$$\sigma_{tot} = \sigma_{abs} + \sigma_{scat} \tag{1.2}$$

$$\sigma_{abs} = k\,\mathrm{Im}(\alpha) \tag{1.3}$$

$$\sigma_{scat} = \frac{k^4}{6\pi}|\alpha|^2 \tag{1.4}$$

where k is the wave vector of light expressed as $[2\pi(\varepsilon_m)^{1/2}]/\lambda$ and Im is the imaginary part of the permittivity. The contribution of each of the two components depends on the size of the particles and on the wavelength of irradiation as reported in Figure 1.4.[8]

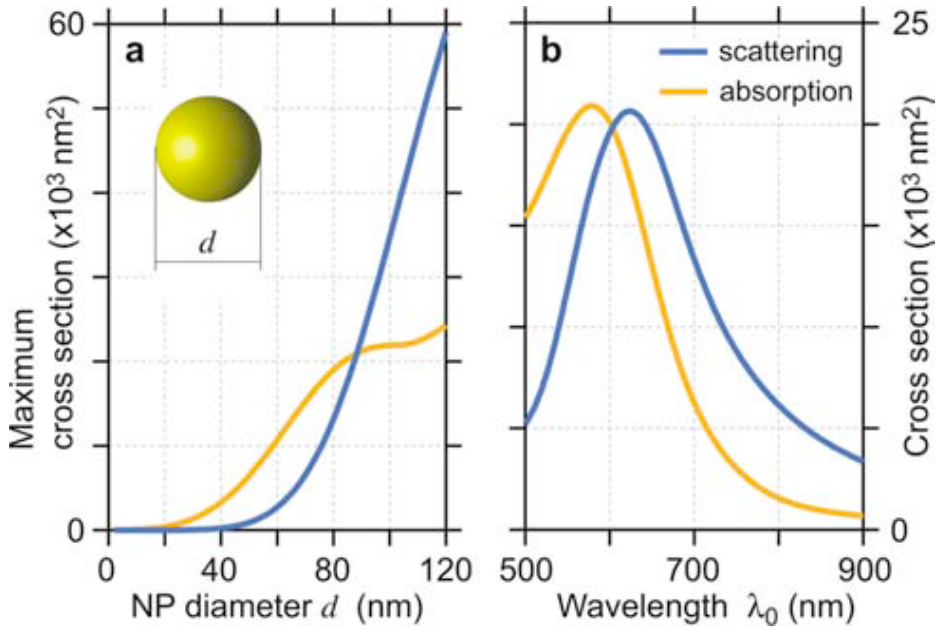

Figure 1.4 (a) Evolution of the maximum absorption and scattering for increasing diameters of AuNP. Spherical AuNP smaller than 90 nm are more efficient absorbers than scatterers. (b) Absorption and scattering cross-section spectra for a gold nanosphere in water, 88 nm in diameter. [Figure reproduced from ref. 8]

In general, metal nanoparticles are very efficient absorbers; however, the choice of size and shape appears crucial when used for different applications. The variation of the

nanoparticle size or shape translates into a variation in the optical properties, meaning that nanoparticles can absorb at different wavelengths, going from the visible to the infra-red according to their morphology. By increasing the size of the particles, a longer surface electron oscillation is obtained after irradiation, decreasing in such a way the frequency of the oscillation and determining a red-shift of the plasmon wavelength. In addition to the size, the synthesis of metal nano-structures with particular shapes, such as nanorods, nanostars, nanocages or nanshells allows for the synthesis of materials with even longer plasmon absorption wavelengths. (Figure 1.5)[9]

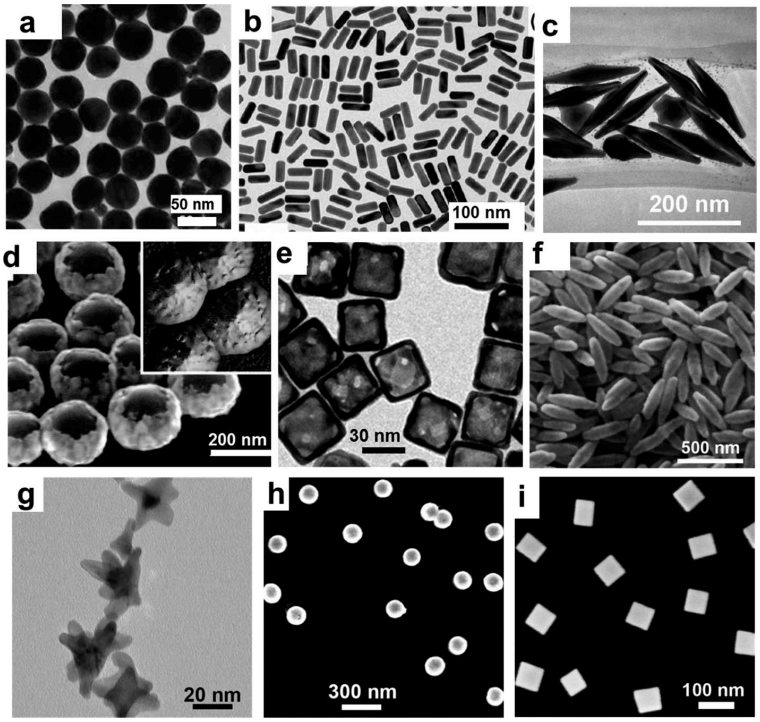

Figure 1.5 SEM and TEM micrographs of gold nanostructures of various shapes and sizes: (a) nanospheres, (b) nanorods, (c) nanobipyramids, (d) hollow interior nanosemishells, (e) hollow interior nanocages, (f) hematite core/Au shell nanorice, (g) nanostars, (h) silica core/Au shell nanoshells, and (i) nanocubes. [Figure reproduced from ref. 9]

For some shapes, the absorption spectra present multiple bands, such as in the case of nanorods where the two bands correspond to the longitudinal and the transversal absorption. In this specific case, increasing the length of the rods results in a bathochromic shift of the longitudinal absorption, as shown in Figure 1.6.

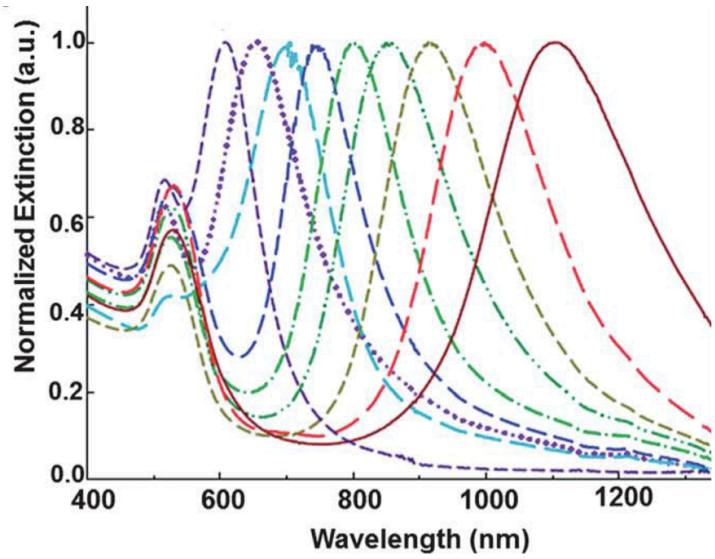

Figure 1.6 Plasmon resonances of nanorods with different sizes (size increases going from the purple trace to red trace). The two bands, observed for each spectrum, correspond to the longitudinal and transversal absorptions for the specific size of nanorods. A red-shift of the longitudinal absorption is obtained by increasing the size of the particles. [Figure reproduced from ref. 9].

The tunability of the plasmon absorption makes nanoparticles very attractive for electric field related applications, such as surface-enhanced Raman scattering (SERS), therapeutics and photocatalytic processes.[9,10] Therefore, several efforts have been made in the synthesis and the modification of such materials using chemical, thermal and photochemical procedures.[10,11]

1.2 Photochemical synthesis

Within all the synthetic procedures developed to control the morphological properties of metal nanoparticles, photochemical methods are very convenient in terms of temporal and spatial control, permitting the use of mild reducing agents and working at room temperature.[11,12] A facile photochemical methodology to synthesize metal nanoparticles was discovered in the Scaiano's group and consists of irradiating a benzoin compound, 1-[4-(2-hydroxyethoxy)phenyl]-2-hydroxy-2-methyl-1-propane-1-one (I-2959) with UVA light.[13]

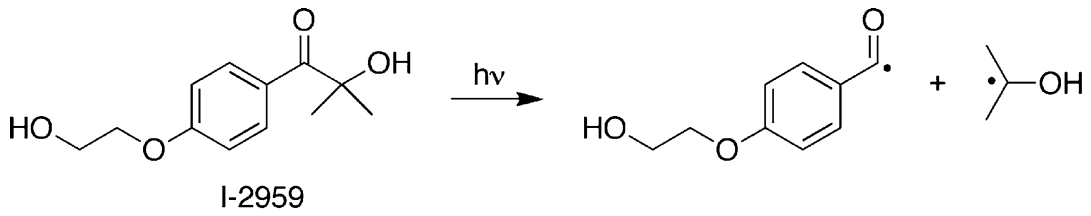

I-2959

Scheme 1.1 Photochemical Norrish type I α-cleavage of I-2959.

The UVA irradiation induces an α-cleavage of the I-2959 triplet excited state *via* a Norrish type I mechanism (Scheme 1.1). The quantum yield of the photodissociation is approximately 0.3 and the lifetime of the excited triplet state is 11 ns.[14] As a result, a benzoyl radical and a ketyl radical are obtained. The latter represents the reducing agent and can be used to reduce different metal salts, such as $AgNO_3$ or $HAuCl_4$. Stoichiometric amounts of I-2959 are required to carry out the metal ion reduction, therefore, a 1:1 ratio is used for Ag^+ and a 3:1 ratio for Au^{3+}. The remaining benzoyl radical will be oxidized by air and the resulting carboxylic acid contributes to the stabilization of the resultant particles.[15] In the case of Au, the reduction mechanism undergoes a series of disproportionation and reduction events, summarized in Scheme 1.2.[16]

$$HAuCl_4 \rightleftharpoons H^+ + AuCl_4^-$$

$$Au^{III}Cl_4^- + RC\dot{O}HR' \longrightarrow Au^{II}Cl_3^- + RCOR' + HCl$$

$$2\,Au^{II}Cl_3^- \longrightarrow Au^{I}Cl_2^- + Au^{III}Cl_4^-$$

$$Au^{I}Cl_2^- + RC\dot{O}HR' \longrightarrow Au^0 + 2\,Cl^- + H^+ + RCOR'$$

$$2Au^{I}Cl_2^- \longrightarrow Au^{II}Cl_3^- + Au^0 + Cl^-$$

$$n\,Au \longrightarrow AuNP$$

Scheme 1.2 Reduction of hydrogen tetrachloroaurate by ketyl radicals.

The formation of AgNP may appear more facile since only one electron is required.[17] However, oxidation of the resultant nanoparticles needs to be avoided using strong stabilizing agents and working under inert atmosphere. Detailed synthetic procedure will be discussed in the following chapters. A summary of the I-2959 photoreduction of Ag^+ is shown is Scheme 1.3.

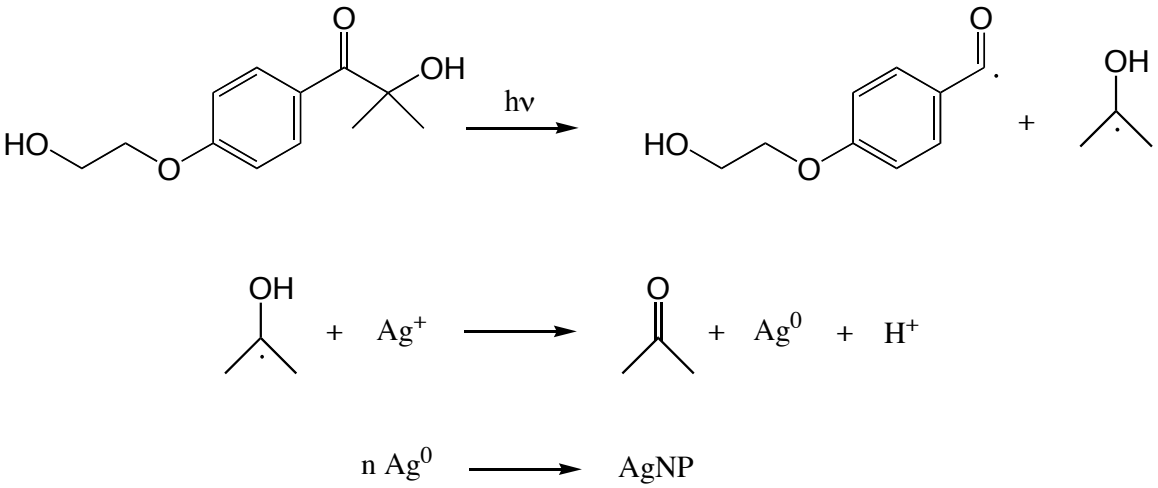

Scheme 1.3 Photocleavage of I-2959, followed by reduction of Ag^+ and formation of AgNP.

AgNP with different shapes can also be obtained by irradiating AgNP seeds of 3 nm with the appropriate LED wavelength. The localized electromagnetic field, created around the AgNP, induces the particle growth, as larger spheres, dodecahedra, nanoplates and nanorods, according to the wavelength of light used. The change in shape corresponds to a change in the absorption spectrum and, therefore, the properties of the particles can be easily tuned based on our needs. (Figure 1.7)[18]

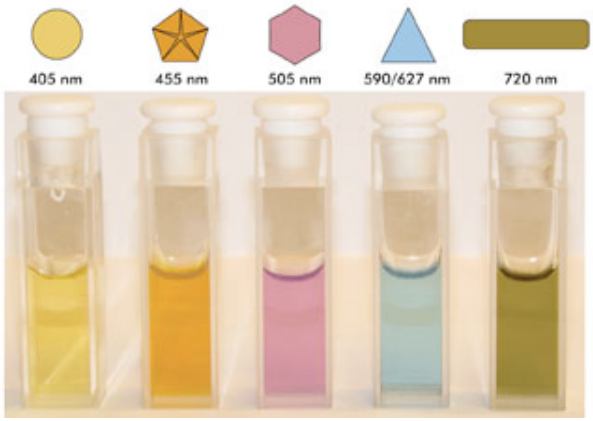

Figure 1.7 Picture of AgNP colloidal solutions produced under the corresponding LED irradiation at the wavelength indicated (in nm) at the top of each cuvette. [Figure reproduced from ref. 18]

The variation in the absorption maximum depends, not only on the size and shape of the nanoparticles, but also on the refractive index of the medium. A linear dependency of the λ_{max} and the refractive index can be obtained for refractive index values ranging from 1.3 to 1.6. However, this approximation fails when working outside this refractive index range. Underwood[19] and Mulvaley[20] derived an equation to calculate this dependence:

$$\lambda_{max}(nm) = 405.2 + 85.93 \times RI \qquad (1.5)$$

where RI is the refractive index of the media.

When working in metal nanoparticle synthesis, several parameters need to be taken into account in order to obtain materials with optimal performance. Size, shape, media and environment are crucial for successful applications, therefore, particular attention is required in the nanoparticle synthetic preparation and characterization.

Over the past 20 years, the Scaiano group has developed a considerable experience in the synthesis, modification and functionalization of metal nanoparticles. However, the final goal of our research group is not focused solely on the production of nanoparticles, but rather on their application. In other words, rather than being a "nanoparticles factory", our main goal is to investigate the potential of these materials in several fields. Therefore, in addition to the synthesis and the modification of metal nanoparticles, this

thesis will focus on some interesting examples of plasmon-mediated processes in catalysis, lithography and biochemistry.

1.3 What can we do with metal nanoparticles?

A recent publication from our research group stated that: *"Surface plasmons are described as the collective oscillations of conduction band electrons following variations of the electric field vector of the incident beam. Simplistic, yet correct, this description fails to give most chemists any idea of what these plasmons could be used for*."[5] This statement underlines how often the mere definition of the plasmon phenomenon does not give a direct explanation of the potential use for nanoparticles; therefore, a better understanding of the processes driven by plasmonic effects is required.

As an example, we can consider a 10 nm spherical gold nanoparticles, whose plasmon absorption is centered at 530 nm. As mentioned before, the excitation of the nanoparticle surface, in this specific case using green light, results in a collective motion of the electrons, which results in the polarization of the particle. Clearly the particle in this "highly energetic" state needs to lose the energy absorbed to return to the initial physical state. To do so, the system follows several pathways, according to the environmental conditions and to the presence of eventual neighbors, placed in its proximity. A schematic representation of the possible mechanisms that can occur after plasmon excitation is reported in Figure 1.8.[21]

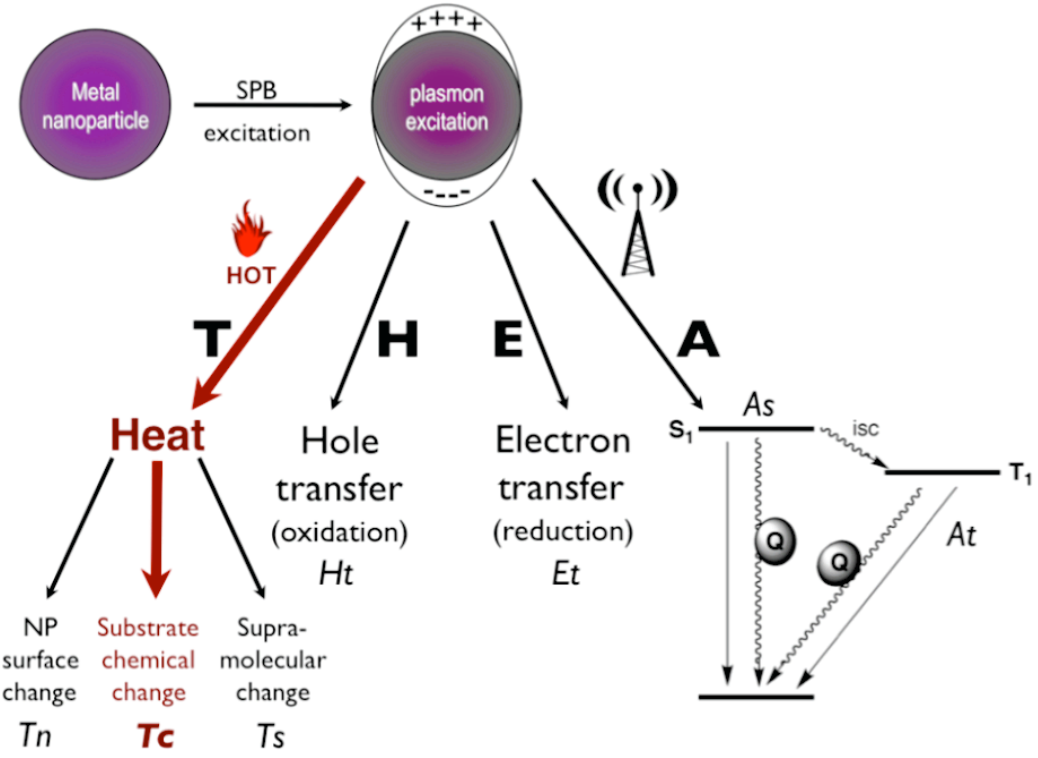

Figure 1.8 Plasmon excitation leads to a range of effects on molecules adsorbed, bound, or in proximity to a nanoparticle, as well as changes in the nanoparticle itself. In the presence of a suitable receiver, antenna effects (A) can result in excited state processes (As and At). Plasmon relaxation can lead to thermal effects (T) that can themselves induce supramolecular changes in guest molecules (Ts), chemical change (Tc) sometimes referred to as photocatalysis, or changes in the nanoparticle itself (Tn) of either a physical or chemical nature (e.g., oxidation). Under Plasmon excitation the nanoparticle can act as an electron donor (Et) or as an electron acceptor (Ht). Color arrows are used for mechanism Tc, the one explored in this paper. [Figure adapted from ref. 21]

Electronic excitation of molecules placed around the nanoparticles is one of the possible mechanisms triggered after plasmon excitation, in a pseudo-transmitter/receiver antenna interaction. (Figure 1.8, pathway A) An example of this phenomenon has been studied by previous members of the Scaiano group.[22] The formation of methylene blue (MB) triplet excited state is enhanced by the vicinity of 15 nm AuNP; however, quenching phenomena are also attributed to the proximity with the nanoparticles. As a result, a different effect is obtained according to the distance between AuNP-MB, as reported in Figure 1.9.[22]

For molecules located within distances >20 nm, the plasmon effect does not influence the photochemistry of the molecule. Enhancement and quenching effects are observable for distances between 2 and 20 nm. Finally, if the molecule is on the surface of the AuNP strong quenching of the singlet or triplet excited states can be observed.

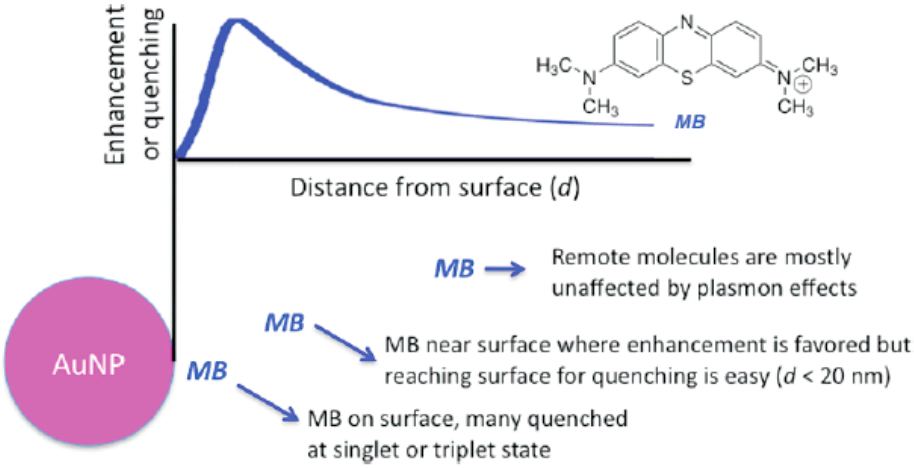

Figure 1.9 Qualitative representation of the methylene blue interaction with the AuNP surface. [Figure reproduced from ref. 22]

The transient particle polarization, as a result of plasmon irradiation, can also lead to electron or hole transfer, particularly in processes where the nanoparticles may behave as a shuttle between different species.[23] (Figure 1.8, pathways H and E) Several catalytic applications have recently been published, especially in processes where the nanoparticles act as an electron-storing/electron-releasing medium, according to the surrounding molecules.[24]

Fluorescence quenching processes, occurring by the proximity of a metal nanoparticle to the fluorophore, are often due to an electron transfer process from the excited fluorophore to the nanoparticle surface.[25] The use of metal nanoparticles for this class of application is limited by the extreme short lifetimes of the plasmon excitation process, in the subpicosecond range. Therefore, short distances between donor and acceptor are required to efficiently observe an electron/hole transfer. Lately several contributions have been published in the field of photovoltaic and water splitting using AuNP-decorated semiconductors, such as ZnO or TiO_2, where AuNP act as electron shuttles to

or from the semiconductors.[26] These processes can be very efficient as a result of the intimate contact of the supported nanoparticle on the semiconductor material.

Considering that the quantum yield of the emission occurring after the plasmon excitation is around 10^{-5} or less, the most efficient process that can occur after metal nanoparticle irradiation appears to be the conversion of energy, absorbed as light, into heat.[27] This process is of primary interest since the thermal energy released is able, not only, to induce morphological modification of the particles and supramolecular changes, but it can also trigger high energy chemical reactions. Within all possible events occurring after plasmon irradiation, the latter is the primary focus of my research project. The possibility of carrying out thermal reactions at room temperature with the only use of a light source appears to be a very intriguing and convenient pathway. Moreover, the high temperature values obtained after plasmon irradiation are extremely localized around the particles, meaning that the overall temperature of the system remains unchanged. In this manner, thermal processes can be performed in very short time scale (submicroseconds) and with exceptional spatial precision. An added advantage of this photochemically driven process is the ability to stop the process by simply turning off the light. Finally, the absorption of visible light makes this potential plasmonic application even "greener" due to the possibility of using solar energy as the source.

In summary, the optical properties of metal nanoparticles have an incredible potential when applied in catalysis, lithography and bio-related applications and this thesis will give a flavor of the promising uses of nanoparticles in those fields.

This general introduction is followed by short presentations of the different projects at the beginning of each chapter. However, for chapter 7 and 8 a more detailed description of the background has been reported in the respective introductive paragraphs due to the specificity of the topic presented.

1.4 References

(1) Schmid, G. Clusters and Colloids: From Theory to Application (Weinheim: VCH), **1994**.

(2) Sciau, P. Nanoparticles in Ancient Materials: The Metallic Lustre Decorations of Medieval, **2012**, Cap.25, DOI: 10.5772/34080.

(3) Faraday, M. Experimental Relations of Gold (and other Metals) to Light. *Philosophical Transactions of the Royal Society,* **1857**, 147, 145.

(4) Feynman, R. P. There's Plenty of Room at the Bottom. *Journal of microelectromechanical System,* **1992**, 1, 60.

(5) Scaiano, J. C.; Stamplecoskie, K. G. Can Surface Plasmon Fields Provide a New Way to Photosensitize Organic Photoreactions? From Designer Nanoparticles to Custom Applications. *Journal of Physical Chemistry Letters,* **2013**, 4, 1177-1187.

(6) Mie, G. Beitrage zur Optik Truber Medien, Speziell Kolloidaler Metallosungen. *Annallen der Physik*, **1908**, 25:377.

(7) (a) Bohren, C. F.; Huffman, D. R. Absorption and Scattering of Light by Small Particles. *Wiley interscience*, **1983**. (b) Baffou, G.; Rigneault, H. Femtosecond-Pulsed Optical Heating of Gold Nanoparticles. *Physical Review B,* **2011**, 84, 035415.

(8) Buffou, G.; Quidant, R. Thermo-Plasmonic: Using Metallic Nanostructures as Nanosources of Heat. *Laser Photonics Review,* **2013**, 7, 2, 171-187.

(9) Webb, J. A.; Bardhan, R. Emerging Advances in Nanomedicine with Engineered Gold Nanostructures. *Nanoscale,* DOI: 10.1039/c3nr05112a

(10) (a) Kumar, C. Metallic Nanomaterials; *Wiley: Weinheim*, **2009**; Vol. 1. (b) Shen, X. S.; Wang, G. Z.; Hong, X.; Xie, X.; Zhu, W.; Li, D. P. Anisotropic Growth of One-Dimensional Silver Rod-Needle and Plate-Belt Heteronanostructures Induced by Twins and Hcp Phase. *Journal of American Chemical Society,* **2009**, 131, 10812–3.

(11) (a) Huang, H. H.; Ni, X. P.; Loy, G. L.; Chew, C. H.; Tan, K. L.; Loh, F. C.; Deng, J. F.; Xu, G. Q. Photochemical Formation of Silver Nanoparticles in Poly(*N*-vinylpyrrolidone). *Langmuir* **1996**, 12, 909–912. (b) Krylova, G. V.; Eremenko, A. M.; Smirnova, N. P.; Eustis, S. Photochemical Preparation of Nanoparticles of Ag in Aqueous-Alcoholic Solutions and on the Surface of Mesoporous Silica. *Theoretical & Experimental Chemistry.* **2005**, 41, 105 110. (c) Sakamoto, M.; Fujistuka, M.; Majima, T. J. Light as a Construction Tool of Metal Nanoparticles: Synthesis and Mechanism. *Photochemistry and Photobiology C,*

2009, 10, 33–56.

(12) (a) Sant'Ana, A. C.; Rocha, T. C. R.; Santos, P. S.; Zanchet, D.; Temperini, M. L. A. Size-dependent SERS Enhancement of Colloidal Silver Nanoplates: the Case of 2-Amino-5-Nitropyridine. *Journal of Raman Spectroscopy,* **2009**, 40, 183–190. (b) Jin, R. Photoinduced Conversion of Silver Nanospheres to Nanoprisms. *Science,* **2001**, 294, 1901–1903. (c) Jin, R. C.; Cao, Y. C.; Hao, E. C.; Metraux, G. S.; Schatz, G. C.; Mirkin, C. A. Controlling anisotropic nanoparticle growth through plasmon excitation. *Nature*, **2003**, 425, 487–490. (d) Callegari, A.; Tonti, D.; Chergui, M. Photochemically Grown Silver Nanoparticles with Wavelength-Controlled Size and Shape. *Nano Letters,* **2003**, 3, 1565–8.

(13) McGilvray, K. L.; Decan, M. R.; Wang, D.; Scaiano, J. C. Facile Photochemical Synthesis of Unprotected Aqueous Gold Nanoparticles. *Journal of American Chemical Society,* **2006**, 128, 15980−15981.

(14) Jockusch, S.; Landis, M. S.; Freiermuth, B.; Turro, N. J. Photochemistry and Photophysics of α-Hydroxy Ketones. *Macromolecules,* **2001**, 34, 1619−1626.

(15) Alarcon, E. I.; Udekwu, K.; Skog, M.; Pacioni, N. L.; Stamplecoskie, K. G.; Gonzalez-Bejar, M.; Polisetti, N.; Wickham, A.; Richter-Dahlfors, A.; Griffith, M.; Scaiano, J. C. The Biocompatibility and Antibacterial Properties of Collagen-Stabilized, Photochemically Prepared Silver Nanoparticles. *Biomaterials,* **2012**, 33, 4947−4956.

(16) Marin, M. L.; McGilvray, K. L.; Scaiano, J. C. Photochemical Strategies for the Synthesis of Gold Nanoparticles from Au(III) and Au(I) Using Photoinduced Free Radical Generation. *Journal of American Chemical Society,* **2008**, 130, 16572−16584.

(17) Scaiano, J. C.; Billone, P.; Gonzalez, C. M.; Maretti, L.; Marin, M. L.; McGilvray, K. L.; Yuan, N. Photochemical Routes to Silver and Gold Nanoparticles. *Pure and Applied Chemistry,* **2009**, 81, 635−647.

(18) Stamplecoskie, K. G.; Scaiano, J. C. Light Emitting Diode Irradiation Can Control the Morphology and Optical Properties of Silver Nanoparticles. *Journal of American Chemical Society,* **2010**, 132, 1825−1827.

(19) Underwood, S.; Mulvaney, P. Effect of the Solution Refractive Index on the Color of Gold Colloids. *Langmuir,* **1994**, 10, 3427−3430.

(20) Mulvaney, P. Surface Plasmon Spectroscopy of Nanosized Metal Particles. *Langmuir,* **1996**, 12, 788−800.

(21) Fasciani, C.; Alejo, C. J. B.; Grenier, M.; Netto-Ferreira, J. C.; Scaiano, J. C. High-Temperature Organic Reactions at Room Temperature Using Plasmon

Excitation: Decomposition of Dicumyl Peroxide. *Organic Letters*, **2011**, 13, 204−207.

(22) Pacioni, N. L.; Gonzalez-Bejar, M.; Alarcon, E.; McGilvray, K. L.; Scaiano, J. C. Surface Plasmons Control the Dynamics of Excited Triplet States in the Presence of Gold Nanoparticles. *Journal of American Chemical Society,* **2010**, 132, 6298–6299.

(23) Barazzouk, S.; Kamat, P. V.; Hotchandani, S. Photoinduced Electron Transfer between Chlorophyll *a* and Gold Nanoparticles. *Journal Physical Chemistry B,* **2005**, 109, 716-723.

(24) (a) Chen, S.; Ingram, R. S.; Hostetler, M. J.; Pietron, J. J.; Murray, R. W.; Schaaff, T. G.; Khoury, J. T.; Alvarez, M. M.; Whetten, R. L. Gold Nanoelectrodes of Varied Size: Transition to Molecule-Like Charging. *Science,* **1998**, 280, 2098. (b) Chen, S.; Murray, R. W. Electrochemical Quantized Capacitance Charging of Surface Ensembles of Gold Nanoparticles. *Journal of Physical Chemistry B,* **1999**, 103, 9996. (c) Baum, T.; Brust, M.; Bethell, D.; Schiffrin, D. J. Electrochemical Charge Injection into Immobilized Nanosized Gold Particle Ensembles: Potential Modulated Transmission and Reflectance Spectroscopy. *Langmuir,* **1999**,15, 866.

(25) (a) Ipe, B. I.; George Thomas, K.; Barazzouk, S.; Hotchandani, S.; Kamat, P. V. Photoinduced Charge Separation in a Fluorophore−Gold Nanoassembly. *Journal of Physical Chemistry B,* **2002**, 106, 18. (b) Kamat, P. V.; Barazzouk,S.; Hotchandani, S. Electrochemical Modulation of Fluorophore Emission on a Nanostructured Gold Film. *Angewandte Chemie International Edition,* **2002**, 41, 2764.

(26) (a) Gomes Silva, C.; Juárez, R.; Marino, T.; Molinari, R.; Garcia, H. Influence of Excitation Wavelength (UV or Visible Light) on the Photocatalytic Activity of Titania Containing Gold Nanoparticles for the Generation of Hydrogen or Oxygen from Water. *Journal of American Chemical Society,* **2011**, 133, 595−602. (b) Choi, H.; Chen, W. T.; Kamat, P. V. Know Thy Nano Neighbor. Plasmonic versus Electron Charging Effects of Metal Nanoparticles in Dye-Sensitized Solar Cells. *ACS Nano,* **2012**, 6, 4418−27.

(27) Coronado, E.; Encina, E.; Stefani, F. Optical Properties of Metallic Nanoparticles: Manipulating Light, Heat and Forces at the Nanoscale. *Nanoscale,* **2011**, 3, 4042.

Chapter 2

Experimental Setup and Instrumentation

In this chapter I will present a brief description of the different instrumentation used either for the performance of a specific process or for the analysis of the results obtained. The materials and methods used for each project will be presented in the corresponding chapter, however all the general technical and experimental setup information are reported in the following paragraphs.

2.1 Light Irradiation Sources

2.1.1 Laser Drop setup

The laser-drop system employed is shown in Figure 2.1. This setup was first used in Scaiano's group in the early nineties[1] and then modified and optimized at the beginning of my graduate studies, thanks to the technical support of Michel Grenier. It consists of a computer-controlled syringe pump that can deliver the sample to the exposure region through a Teflon needle with an external diameter of 1.6 mm (used as a ruler to measure the drop size). The volume delivered and the number of laser pulses per drop (delivered

at 1 Hz) is programmable. Laser excitation was performed with the frequency doubled 532 nm (~ 8 ns) pulses from a Nd:YAG laser, with a power of 50 mJ/pulse; in order to prevent drop explosions and multiple laser pulse exposures the beam was concentrated, but not focused on the sample drops. Images were captured with a Nikon D90 DSLR camera, equipped with a Sigma 105 mm f 2.8 macro lens, controlled by the laser-drop system. A 532 nm notch filter was used in front of the camera lens, to make it "blind" to the green laser beam and to prevent camera damage.

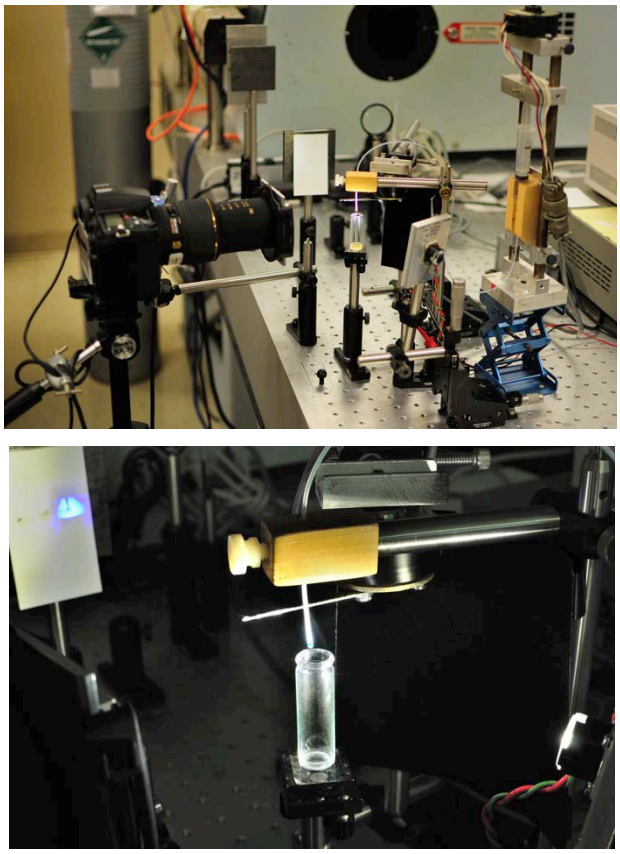

Figure 2.1 (top) Pictures of the laser drop. (bottom) Vial placed under the Teflon tube to collect the irradiated drops.

2.1.2 Light Emitting Diodes

LED irradiation was performed using a custom-designed LED irradiator, consisting of four LedEngin 10 W LZ4-40G110 emitters attached to an aluminum heat sink and a fan cooling system. (Figure 2.2)

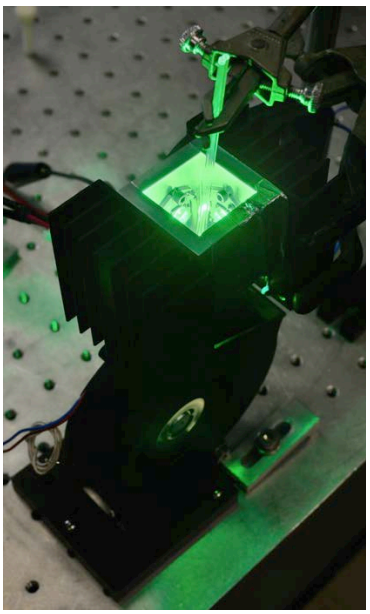

Figure 2.2 530 nm LED irradiator connected to a fan cooling system.

The maximum of the emission is centered at λ_{exc} = 530 nm as reported in Figure 2.3 The flux of the LED at the intensity used in the experiment (~1 A) is 625 lumens per LED, for a total flux received by the sample with the 4 LED set up of 2500 lumens.

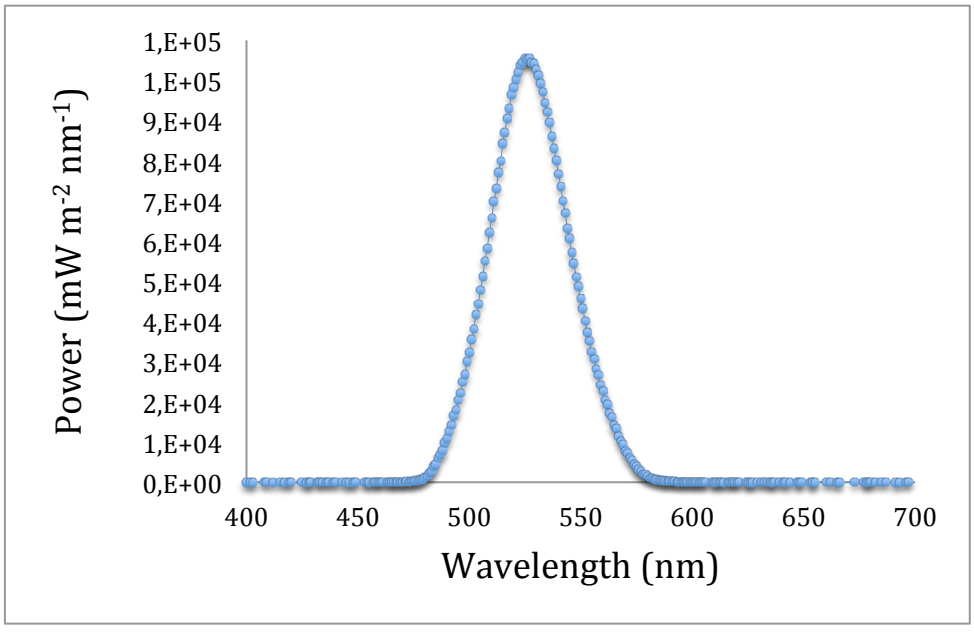

Figure 2.3 Emission spectrum of the 530 nm LED used.

2.1.3 Photoreactor

Luzchem LZC-4 (Luzchem Research, Inc.) photoreactor with 14 UVA lamps was used as irradiation source for the nanoparticles preparation. The power dose obtained range from 9 to 60 W/m^2. When the 14 lamps are in use the temperature inside the photoreactor was measured to be 31°C. Samples were irradiated in quartz cuvettes with a rotating carousel or in a 24 well plate, both centered in the LZC-4.

2.2 Steady-State Spectroscopy

2.2.1 UV-Vis Absorption Spectroscopy

Absorbance spectra were measured using a Cary 50 UV-Vis spectrophotometer, using a quartz cuvette with a path length of 1 cm. Occasionally, the absorbance was taken using a Molecular Devices SpectraMax M5 well plate absorbance reader in a well plate mode.

2.2.2 Spectrofluorimeter

Emission spectra were collected using a Photon Technology International (PTI) spectrofluorimeter. Specific information on the excitation and emission wavelengths is reported in each chapter where this technique was employed.

2.2.3 Raman Spectroscopy

Raman spectra were collected for the structural analysis of carbon-based materials as reported in Chapter 9. For these experiments a Reinshaw In Via apparatus with a 750 nm laser was used. An Olympus optical microscope was adapted to the instrument. Typically, the sample suspended in water, was sonicated for 15 min and drop-casted on a quartz plate. The solvent was evaporated before recording the spectra. For the graphene analysis, an area of 10 μm^2 was selected and an average of 24 scans were performed.

2.3 Microscopy

2.3.1 Scanning Electron Microscopy (SEM)

Particle size, shape and distribution were examined by analysis of representative scanning electron microscopy and transmission electron microscopy (TEM) images. SEM images were obtained using a JSM-7500F field emission scanning electron microscope from JEOL Ltd in either transmission electron detector (TED) mode with a bright field (accelerating voltage 20 kV, emission current 20 mA, 8 mm working distance), secondary electron imaging (SEI) mode (accelerating voltage 4.0 kV, emission current 20 μA, working distance 2-6 mm) or in Rutherford backscattered electron (RBEI) mode (accelerating voltage 20 kV, emission current 20 μA, working distance 8 mm). RBEI detector was used to obtained sample surface composition information using the COMPO mode. Energy dispersive X-ray spectroscopy (EDS) was used in conjunction with SEM. This chemical microanalysis technique detects x-ray emitted from the sample during bombardments by electron beam to characterize the elemental composition of the analyzed volume. The EDS detector from Oxford Instrumentation was employed to quantify the silver and gold ratio for the core-shell project reported in Chapter 3. The analysis of the data was done using INCA software.

2.3.1 Transmission Electron Microscopy (TEM)

TEM micrographs were collected using a high-resolution transmission electron microscope (HRTEM). A JEOL JEM-2100F field emission transmission electron microscope equipped with an ultrahigh-resolution pole piece operating at 200 kV was used to collect TEM and HRTEM images. Preparation of the samples was as follows: approximately 10 μl of solution were deposited on a copper grid coated with carbon film (400 mesh) and dried under vacuum (~ 10^{-3} Pa).

Cryo-SEM images were occasionally taken for the dsDNA plasmon-mediated melting project reported in Chapter 7. For this purpose images of a cover glass slip functionalized with AuNP were taken using Tescan – VegaII XMU microscope,

available at Carleton University. Prior to the SEM measurements the samples were uniformly coated with ~1 nm gold, using a Hummer VII sputter (Anatech Ltd.). A chamber pressure of 9.8 x 10^{-3} Pa and a voltage of 20 kV were used in the analysis.

2.3.3 Atomic Force Microscopy (AFM)

This scanning probe microscopy technique was used to have surface information regarding our lithography application of plasmon. The information is obtained from the probe's interaction with the surface. Topographic imaging was performed under air on various areas from several exposed films after washing with water, using a Molecular Imaging PicoPlus Atomic Force Microscope working in non-contact mode. The AFM probes used for imaging had a nominal resonance frequency of 150 kHz, force constant of 5 N/m and were manufactured by Budget Sensors (Tap150-G).

2.3.4 Fluorescence Lifetime Imaging Microscopy (FLIM)

Fluorescent Lifetime Imaging System (FLIM, PicoQuant) instrument is equipped with a frequency doubled picosecond pulse diode laser (530.6 nm, 78 ps, 40 MHz, LDH-P-FA-530L, PicoQuant). The laser beam was collimated and focused through a fiber-coupling unit. A beam splitter Z532rdc (Chroma) was used to reflect the excitation light into the oil immersion TIR (total internal reflection) objective (100X, NA1.45, Olympus, PLAPO). The epi fluorescent signal is passed through a 560 nm long pass filter and was collected by Spectrograph (Shemrock 163, Andor).

2.3.5 Total Internal Reflection Fluorescence (TIRF) Microscopy

Fluorescence imaging was performed with an Olympus FV1000 TIRF (Olympus, Japan). The instrument is equipped with a CW laser (543 and 633 nm He-Ne laser). The laser beam is collimated and focused through a fiber-coupling unit and the excitation light is reflected into the oil immersion TIR (total internal reflection) objective (100X, NA 1.45, Olympus, PLAPO). Fluorescence filter cubes were used on occasion. The signal was collected onto a Rolera EM-C^2 (Q-Imaging) camera.

2.4 Chromatography

2.4.1 High Pressure Liquid Chromatography (HPLC)

A Waters Integrity high pressure liquid chromatograph in tandem with a reverse phase C18 Zorbax column was employed to analyze reaction products in the case of dicumyl peroxide decomposition project (Chapter 4), using a 80:20 CH_3CN/MilliQ H_2O eluent mixture and a 0.5 mL/min flow rate.

2.4.2 Gas Chromatography Coupled to Thermal Conductivity Detector (GC-TCD)

Gas evolution produced after reduced graphene oxide irradiation (reported in Chapter 9) was investigated using a PerkinElmer Clarus 480 gas chromatograph in line with a thermal conductivity detector (TCD). For a typical analysis, 1 mL of gas sample was manually injected for a 12-minute run. The gases were carried on argon, due to its high sensitivity for hydrogen gas. A packed column (9' Molecular Sieve 13X, 45/60 mesh, 1/8" SF), maintained at constant temperature of 60°C, was used to separate all the light gases (O_2, N_2, H_2, etc.). Detection of the gases was possible using a thermal conductivity detector at a constant temperature of 150°C.

2.5 Other Instrumentation

2.5.1 Quadrupole Mass Spectrometer (QMS)

The apparatus consists of an ultra high vacuum chamber equipped with an AccuQuad residual mass analyzer and a leak valve connected to a gas reservoir. The base vacuum pressure of ~ $1x10^{-8}$ mbar as monitored by an ion gauge (Granville-Phillips) is achieved by a turbomolecular pump (Pfeiffer TMU 071, 60L/s) backed up by a mechanical pump (Edwards E5). The mass spectrometer head consists of an electron impact ionization source (70eV), a quadrupole for mass selection and a Faraday Cup detector. The analyzer range is 1-200 amu. The QMS was calibrated prior to each measurement using a two point range (m/z = 2 and 44) and the resolution was adjusted such that the FWHM of a single mass peak was 0.6 mass units.

The gas sample to analyze was injected into a 50 cm^3 reservoir maintained under vacuum (~10^{-1} mbar) with a roughing pump. A leak valve connected the reservoir to the high vacuum where the mass spectrometer resides, such that the vacuum was maintained at 1x10^{-5} mbar. Upon injection of the sample, chemical species were identified using an AccuQuad residual mass analyzer. Concentration of species was internally calibrated using the known vapor pressure of water during the reaction.

2.5.2 Microwave

A CEM Discover Microwave was used as a comparison with the LED and laser irradiation sources for the projects presented in Chapter 4 and Chapter 5. For these experiments, the solution was placed in a CEM 10 mL Pyrex reaction tube and sealed with a Teflon cap; each sample was irradiated for 20 min at 80°C (300 W).

2.5.3 Dynamic Light Scattering and Z-potential

Dynamic light scattering and Z-potential measurements were obtained using a Malvern Zetasizer Nano (ZEN3500) fitted with a 633 nm laser (DPSS, 50 mW).

In the first case, particle sizes were determined based on the fluctuations in scattered light of a sample. For these measurements 200 μL aliquot of nanoparticles was added to 1.5 mL of distilled deionized water in a plastic, disposable cuvette. 12-15 measurements were performed per samples to determine the hydrodynamic radius.

For the Z-potential measurements, electrophoretic mobility of the particles was measured by taking the average of three consecutive measurements obtained analyzing the colloid solution in disposable folded capillary cells.

2.6 References

(1) Banks, J. T.; Scaiano, J. C. The Laser-Drop Method: A New Approach To Induce Multiple Photon Chemistry with Pulsed Lasers. Examples Involving Reactions of Diphenylmethyl and Cumyloxyl Radicals. *Journal of American Chemical Society,* **1993**, 115, 6409–6413.

Chapter 3

Modification of Noble Metal Nanomaterials

3.1 Introduction

Noble metal nanoparticles have been successfully employed in a wide range of fields, from catalysis to biomedicine, due to their unique and distinct properties compared to the bulk material.[1-3] Critical aspects to take under consideration when using metal nanoparticles in different application are related to size, shape and not least composition of the colloids.[4,5] Therefore, several efforts have been made in order to tune their morphological properties and, in recent years, different preparation methods have been developed to achieve the desired morphology;[6] among all these methods, "seeding" procedures have been commonly adopted to grow metal particles in a controllable manner. This approach takes advantage of surface catalysis, in which the surface of the nanoparticle acts as a preferred site for the metal ion to be reduced, avoiding a new nucleation.[6,7] Natan et al. have shown that it is possible to increase the size of gold nanoparticles used as seeds by adding subsequent layers, ending with a uniform size distribution.[8] In this strategy metal nanoparticles are added to a mixture of the metal salt and a mild reducing agent, giving rise to a process in which the nucleation phase is

separated from the growth period. I tried to take advantage of this observation and combine it with the use of a photochemical strategy to grow Au/Ag core shell materials. Independently, a previous member of Scaiano's group, Kathy McGilvray was developing a procedure to photochemically control the growth of gold nanoparticles using a seeding approach. The controlled synthesis of AuNP and the formation of Au/Ag core shell particles using the photo-seeding method have been published as a single contribution since both are based on the same approach and represent a facile and efficient method for making nanomaterial with defined size and composition (Figure 3.1).[9]

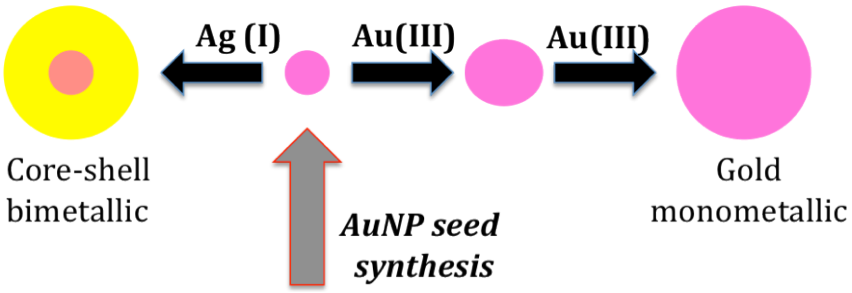

Figure 3.1 Cartoon representation of the controllable growth of AuNP or Au/Ag core-shell particles using the photoseeding approach. [Figure reproduced from ref. 9]

3.2 Materials and Methods

3.2.1 Materials

$HAuCl_4 \cdot 3H_2O$, $AgNO_3$ and sodium citrate were purchased from Sigma-Aldrich and used as received. I-2959 was obtained as generous gift form BASF supplied by Dempsey Corporation Canada and recrystallized by ethanol. For all the samples distilled deionized water was obtained from Millipore MilliQ water filtration system with a measured resistivity of 18.2 Ω.

3.2.2 Preparation of AuNP seeds

AuNP used as seeds were synthesized following a common procedure used in Scaiano group.[9] Briefly, an aqueous solution of 0.33 mM $HAuCl_4$ and 1.0 mM I-2959 were irradiated in a 24-well plate using 14 UVA lamps (59.2 W/m^2) for 15 min. In order to reduce particle size variance, the reagent solutions were prepared in large volumes and then distributed into the 24-well plate, 2.5 mL of solution in each well. After irradiation the solution was left for a minimum time of an hour in the dark before the functionalization with silver. One-exposure irradiation of I-2959/$AuCl_4^-$ of 3:1 stoichiometry gives particles of ~ 12 nm in diameter.

3.2.3 Seed mediated growth

1 mL of AuNP seeds was added to a growth solution of $AgNO_3$ and I-2959. Different concentration of $AgNO_3$ and I-2959 were used with respect to the AuNP, in order to modify the relative thickness of the gold core or silver shell. In particular, three different proportions were chosen: Au/Ag= 65/35; Au/Ag= 50/50; Au/Ag= 35/65. To get those ratios we used the following concentration: 0.11 mM $HAuCl_4$: 0.059 mM $AgNO_3$ for the 65:35 ratio; 0.11 mM $HAuCl_4$: 0.11 mM $AgNO_3$ for the 50:50; 0.11 mM $HAuCl_4$: 0.2 mM $AgNO_3$ for the 35:65. The mixture was purged with N_2 for 15 min and irradiated for 10 min with 14 UVA lamps using a photoreactor.

3.3 Photochemical strategies for the seed-mediated growth of gold-silver core-shell nanoparticles

3.3.1 I-2959 as Reducing Agent

A critical aspect when making metal nanoparticles and, therefore, synthesizing metal core-shell structures, is the choice of the reducing agent. Indeed, the use of very strong reducing agents can favor a second nucleation process, leading to the formation of new nuclei in solution and ending with a sample containing particles with different sizes and composition.[6-8, 10-13] Ascorbic acid, hydroxylamine hydrochloride and hydrazine are

some of the most common reducing agents used, to name a few. In this photochemical approach to make Au/Ag core-shell, the choice of the reducing agent fell on the molecule 1-[4-(2-hydroxyethoxy)phenyl]-2-hydroxy-2-methyl-1-propane-1-one, commercially known as Irgacure-2959. This benzoin compound has a strong UV absorption with ε_{280nm}= 1000 M^{-1} cm^{-1}. When I-2959 is irradiated with ultraviolet light a triplet excited state of the α-hydroxy ketone with a lifetime of 10 ns is obtained.[14] This short lifetime makes the excited state more difficult to be quenched by the metal salts. A Norrish type I cleavage occurs after excitation (Scheme 3.1).

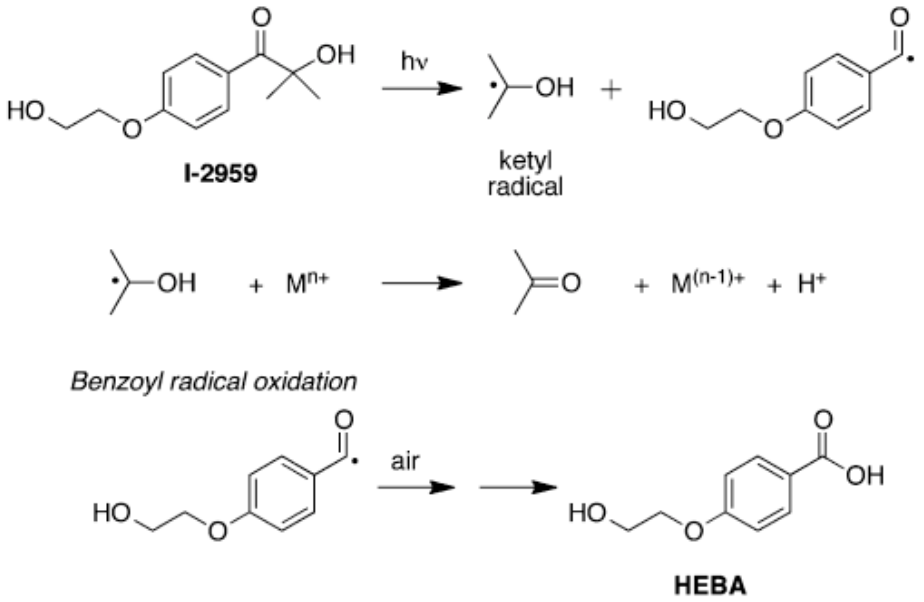

Scheme 3.1 Schematic representation of the synthesis of metal nanoparticles, obtained by I-2959 photolysis and subsequent oxidation of its radial products.

The photocleavage leads to the formation of a benzoyl radical and a 2-hydroxylpropyl radical or "ketyl" radical.[15] The latter can be considered as a "caged electron", responsible for the reduction of the metal ions to metal nanoparticles. The final products obtained after UV irradiation of I-2959 are acetone and 4-hydroxyethoxy benzoic acid (4-HEBA). 4-HEBA acts as a mild stabilizing agent for the particles and can be easily removed. No covalent bonds between the nanoparticle surface and the stabilizer are formed, leaving the particles largely unprotected while sufficiently stable. All those properties, in addition to the good solubility in water, make I-2959 a great candidate for

the photochemical synthesis of metal nanoparticles.[16] In a recent publication of the Scaiano's group, it has been shown how the process occurring during the reduction of metal ions to metal nanoparticles using I-2959 is in fact a proton coupled electron transfer (PCeT), in which the presence of a proton receptor is crucial for the successful completion of the process.[17]

3.3.2. Core-shell *vs*. alloys or individual nanoparticles

Bimetallic nanoparticles have gained increasing attention in the last years, due to the possibility of combining the properties of the different metals used and to the variety of structures that can be obtained. Within the bimetallic particles, we can distinguish between "alloys" and "core-shell" particles. The former can be defined as particles with a homogeneous distribution of two kinds of metals, while in the core-shell the two types of metals are disposed in a heterogeneous arrangement in which one of the metals is surrounding the other one (Figure 3.2).[18]

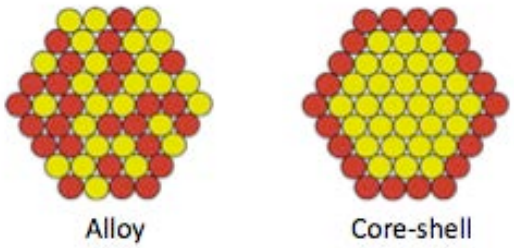

Figure 3.2 Cartoon of an alloy and a core-shell type of structures.

In this photoseeding approach, the AuNP seeds are added to a degassed mixture of $AgNO_3$, citrate and I-2959 and then irradiated. The reduction of Ag(I) on the AuNP seeds surface occurs within few minutes. Addition of citrate to the growth solution stabilizes the particles for several months. Figure 3.3 shows the color of the solution before and after irradiation. The comparison of the orange tint is an indication of the effective reduction of Ag^+. In addition, no evidence for the precipitation of AgCl was observed, probably due to its stabilization as $AgCl_2^-$. However, no indication about the nature of the particles obtained can be derived from this observation. Three possible nanostructures such as, individual nanoparticles, core-shells or alloys, could have been

formed.

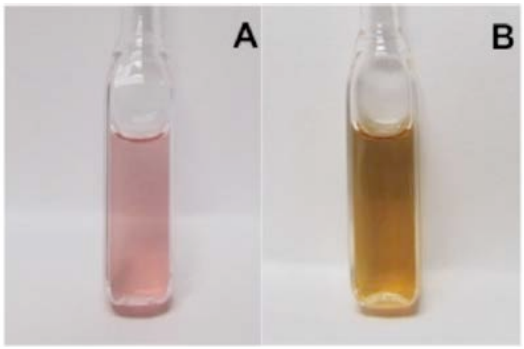

Figure 3.3 Pictures of the sample before (A) and after 10 min irradiation (B).

In order to further investigate if bimetallic particles (Au/Ag core shells or Au-Ag alloys) or individual AgNP and AuNP were formed, UV-Vis analysis was performed before and after irradiation. The SPR band of Au spherical nanoparticles centered at 522 nm is the only one observed in the visible range before irradiation, as expected. In case individual AgNP are formed, we should expect their SPR band at ~ 400 nm and no shift of the one corresponding to AuNP. In contrast, the formation of alloys particles would give a UV-Vis spectrum where only one band located between those of pure AuNP and AgNP is observed. Finally, if core shells are synthesized, a shift on the maxima of the two SPR bands is expected, due to the surface modification of the core particle. More specifically, the addition of a silver shell around the AuNP surface results in a variation of the refractive index around the AuNP seeds, which influences the overall polarizability of the superficial electrons and induces an hypsocromic shift of the AuNP SPR band. By looking at the UV-vis analysis, shown in Figure 3.4, the latter case appears to be the one occurring. Indeed, after irradiation, the AuNP plasmon band shifts from 522 nm to 489 nm and a new band at 400 nm appears. These details clearly indicate the presence of core-shell type of structures.

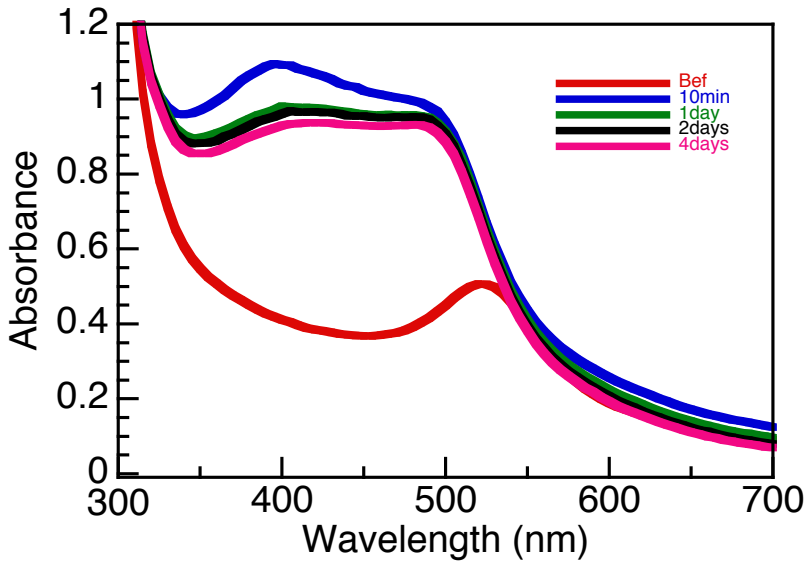

Figure 3.4 UV absorption spectra of the Au/Ag core-shell nanoparticles (50:50) right after the synthesis (10 min) and days after the reaction. For this experiment the concentration of $HAuCl_4$ and $AgNO_3$ used was 0.11 mM.

In order to confirm that the UV-Vis spectra obtained do not correspond to the presence of separate AuNP and AgNP, a mixture of independently synthesized particles was analyzed and the UV-Vis absorption was compared to the 50/50 photoseeded Au/Ag core-shell (Figure 3.5). In the mixture of individual AuNP and AgNP the UV-Vis spectrum shows two bands centered at the maxima expected for silver and gold particles obtained using I-2959 (410 nm and 520 nm respectively). In contrast, the aspect of UV-Vis spectra obtained analyzing our core-shell sample presents the expected shifts for the two maxima, due to a surface modification.

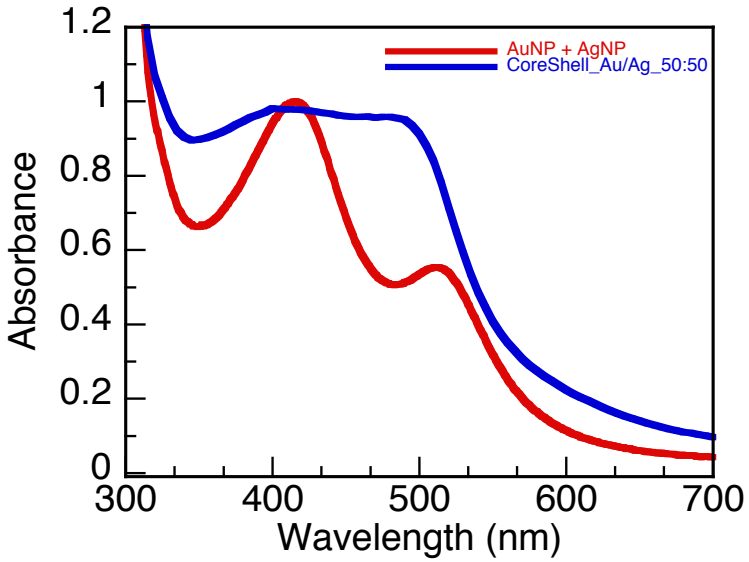

Figure 3.5 Normalized UV absorption spectra of 50:50 Au/Ag core shell (blue trace) and the mixture of AuNP and AgNP (red trace).

An additional confirmation of the presence of core-shells was also provided by TEM microscopy. Figure 3.6 shows a representative example of a 50/50 Au/Ag core-shell sample, where a darker core surrounded by a lighter shell is clearly distinguishable. The inner portion of the core shell particle can be attributed to the AuNP seed used, since it appears darker at the TEM image compared to the external layer, which is the silver shell. The previous observation is based on the consideration of the different electron density of the two metal nanolayers.[19,20] Finally TEM images provided information about the average size of the nanomaterials obtained, which appears to be 15 nm, and the thickness of the silver layer, which ranges from 2 to 5 nm.

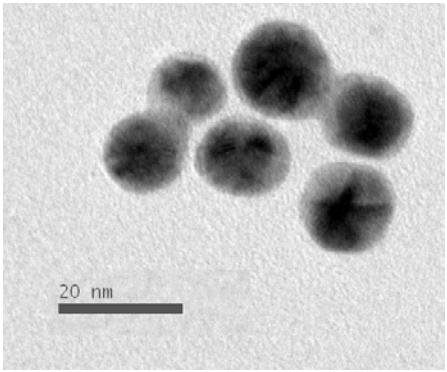

Figure 3.6 TEM images of core-shell nanoparticles solution.

For a more comprehensive characterization of the particles obtained, Energy Dispersive Spectroscopy (EDS) measurements were carried out. The elemental analysis confirms that the ratio between Au and Ag reflects the initial proportions used and no newly formed monometallic AgNP were observed (see results in Table 3.1).

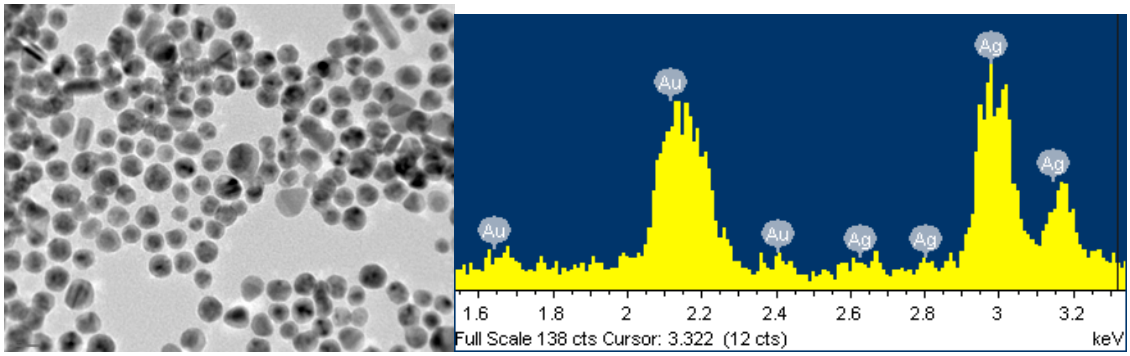

Figure 3.7 TEM images and electron energy spectrum for the Au/Ag 50:50 core-shell sample.

The core-shells synthesized using the described photoseeding procedure appear to have a cleaner structure compared to those prepared in surfactant media.[18-20]

In the following section will be discussed how this approach provides a reproducible way to control the overall composition and size of both the core and the shell.

3.3.3. Core-shell structural variation

One of the major aspects related to core shell structure is the distribution of the two metals. By varying the proportion of each layer it is possible to tune the SPR and in case, for example, of bio-application it is possible to combine the antimicrobial effect, provided by AgNP, with the photothermal effect of AuNP (as discussed in chapter 9).
In order to modify the thickness of the two metals layers, we investigated the effect of the Au/Ag ratio variation. The proportion chosen were: Au/Ag = 50/50 (0.11 mM $HAuCl_4$ and 0.11 mM $AgNO_3$); Au/Ag = 65/35 (0.11 mM $HAuCl_4$ and 0.059 mM $AgNO_3$), and Au/Ag = 35/65 (0.11 mM $HAuCl_4$ and 0.2 mM $AgNO_3$). Citrate concentration of 0.83, 0.69, and 1.08 mM were used for 65:35, 50:50, and 35:65 Au/Ag

ratios, respectively. A difference in the solution tint between the three samples was first noticed, going to a brighter orange color with increasing the silver shell thickness. Figure 3.8 shows how the SPR bands reflect the ratio of metals used. Compared to the AuNP seeds, the Au/Ag = 65/35 solution presents a small shifts from 522 to 520 nm for the AuNP maximum and an increase in absorption in the region between 350 and 500 nm.

For the 50:50 Au/Ag solution a stronger hypsochromic shift from 522 to 489 nm is observed, in addition to a band around 400 nm. The intensities of the two maxima are comparable, as expected from the initial ratio used between Au and Ag. Finally, the Au/Ag = 35/65 proportion displays a more intense band around 405 nm, attributed to the stronger Ag absorbance in the core-shell structure, compared to the other shoulder at 490 nm attributed to the Au contribution. The changes are in line with those observed in other Au/Ag bimetallic systems.[21-24]

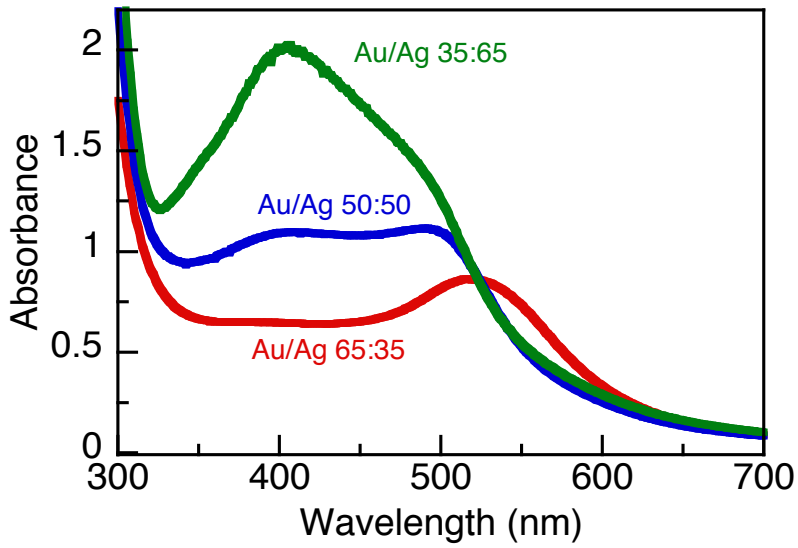

Figure 3.8 UV absorption spectra of core-shell nanoparticles synthesized with different Au/Ag proportions. The ratios were obtained using a different proportion of $HAuCl_4$ and $AgNO_3$ (Au/Ag 35:65−0.11 mM $HAuCl_4$ and 0.2 mM $AgNO_3$, Au/Ag 65:35−0.11 mM $HAuCl_4$ and 0.059 mM $AgNO_3$, Au/Ag 50:50−0.11 mM $HAuCl_4$ and 0.11 mM $AgNO_3$).

In addition, analysis of the core-shell sizes was performed using TEM and DLS. Representative TEM micrographs for the three different solutions are reported in Figure 3.9.

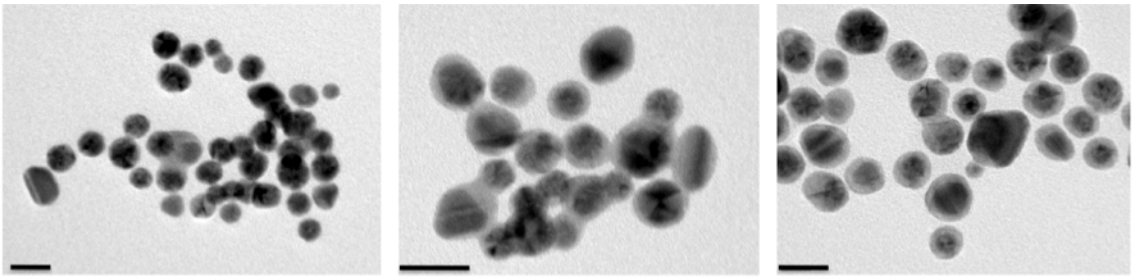

Figure 3.9 TEM images of core-shell nanoparticles solutions synthesized using different Au/Ag proportions: 65/35 (left); 50/50 (central); 35/65 (right). The size bar is 20 nm.

An increasing thickness of the lighter shell is observed by lowering the Au/Ag ratio. Moreover, looking at the hydrodynamic radii, reported in Table 3.1, a decrease in the size of the overall core-shell structure, including the hydrodynamic layers, is observed when decreasing the content of Au in the bimetallic system. These values were measured analyzing a large ensemble of particles by dynamic light scattering (DLS) technique.

Table 3.1 Summary of Physical and Chemical Properties of the Core−Shell Nanoparticles with Different Au/Ag Atomic Ratios (Citrate Present)[a]

Au/Ag ratio	Au/Ag ratio (measured by EDS)	λ_{max}	Size (nm)[c]	Zeta potential (mV)[b]
100:0	100:0	522	10	-30
65:35	65.8:34.2	520	18.8 ± 6.9	-35.1
50:50	52.8:47.2	400; 489	13.8 ± 1.2	-35.9
35:65	36.8:63.2	405	14.1 ± 3.5	-41.0

[a] Citrate concentration of 0.83, 0.69, and 1.08 mM were used for 65:35, 50:50, and 35:65 Au/Ag ratios, respectively. [b] Typical errors for Z-potential measurements are ~10%. [c] Hydrodynamic radii were collected using dynamic light scattering from a large ensemble of particles.

Furthermore, Z-potential measurements were performed in order to obtain more information regarding the surface charges of the core-shells synthesized. AuNP, prepared by the I-2959 method in water with pH 3.0, produced zeta potentials of approximately -30 mV. By subsequently increasing the amount of Ag on the surface of the AuNP seeds, the Z-potential became more negative, reaching a value of -41 mV when the Au/Ag ratio analyzed is 35/65 (see Table 3.1). The decreasing value of the Z-potential when increasing the amount of silver is due to the higher concentration of

citrate added as a stabilizer. AgNP are indeed more prone to oxidation compared to AuNP and therefore by increasing the thickness of the silver layer an increasing concentration of citrate is employed. The Z-potential of monometallic AgNP has been measured as -40 mV.

Moreover, the stability of the core-shells made using the three different Au/Ag ratios was tested following the absorption spectra over time, as reported in Figure 3.10. After the first 5 min of irradiation the particles are already formed but not yet stabilized. Leaving the sample in the dark overnight is sufficient to allow the growth to be completed and obtained a stable nanomaterial. Minimal changes in the absorbance intensity are observed from 2 to 4 days after the initial irradiation.

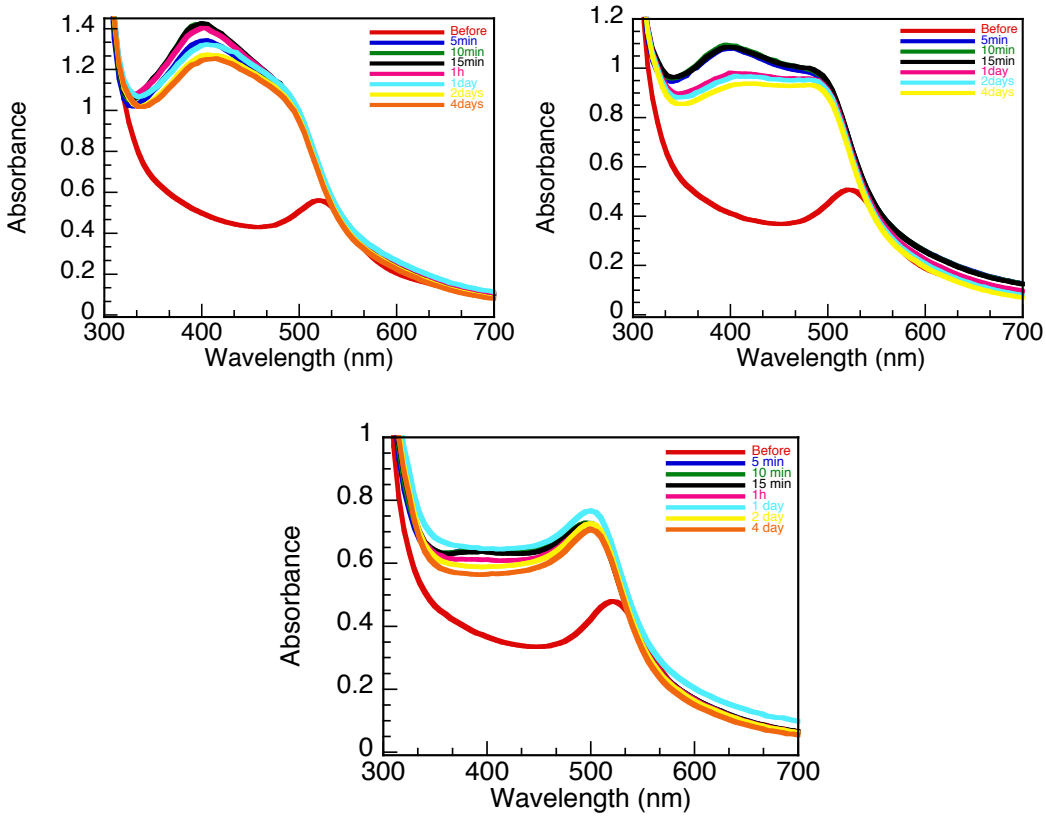

Figure 3.10 UV absorption spectra of the core-shell nanoparticles recorded at different times. (Top left) Au/Ag 35:65 0.11 mM $HAuCl_4$ and 0.2 mM $AgNO_3$. (Top right) Au/Ag 50:50 −0.11 mM $HAuCl_4$ and 0.11 mM. (Bottom) Au/Ag 65:35−0.11 mM $HAuCl_4$ and 0.059 mM.

3.3.4. Light irradiance dependence

Having established the dependence of the thickness layer on the amount of metal used, we tried to investigate the effect of the light dose in the synthesis of the core-shell nanoparticles. In order to explore this aspect we used a Luzchem photoreactor equipped with a different number of UVA lamps and we recorded a UV-Vis spectrum after 2 min of irradiation for each light dose used. A spectroradiometer, consisting in a spectrometer connected to a detector head by a fiber optic cable, was used to quantify the light used in each experiments (Figure 3.11). Therefore, a power spectrum, reporting the energy distribution as a function of the wavelength, can be obtained by disposing the detector head inside the photoreactor with the selected number of lamps (2, 4, 8, 14 lamps respectively). Four different irradiances were used ranging from 9.2 to 59.2 W/m^2.

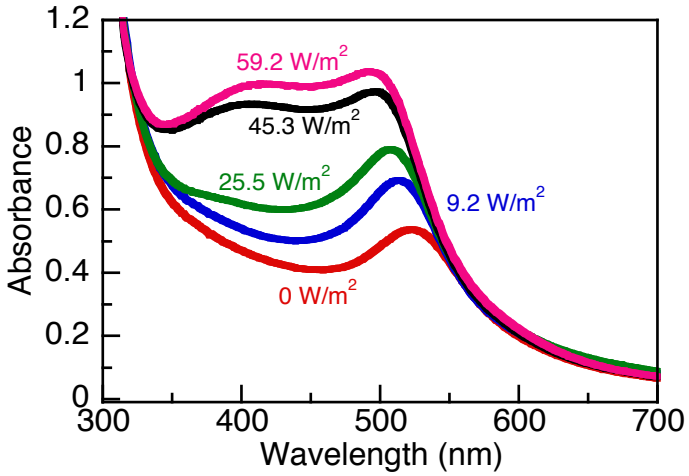

Figure 3.11 UV absorption spectra of 50:50 Au/Ag core shell after 2 min irradiation at different light irradiances.

Increasing the UVA dose leads to an approximately linear growth of the SPR at 400 nm and a proportional shift of the AuNP SPR, which goes from 522 nm when not irradiated to 490 nm when irradiated using an irradiance of 59.2 W/m^2. This experiment suggested that the light irradiance is crucial for the core-shell synthesis process and therefore particular care must be taken when choosing the proper light power to get the best performance.

3.4 Summary

The synthesis of Au/Ag core-shell nanoparticles using a photo-seeding approach was successfully investigated and a facile method for a better control of the core-shell layers thickness and composition was derived. Variation of the precursors concentration allowed simple and reproducible growth of core-shells with low polydispersity to be achieved.

By varying the irradiance dose a defined photochemical control can be obtained. Although silver was chosen as a representative, in principle other metals reducible with ketyl radicals can be exploited to form a shell on the surface of a given AuNP seed. A comprehensive study of the core-shell properties has been realized, in terms of optical properties, morphology and composition. This information allows us to easily select the conditions required to obtained core-shell nanoparticles with precise properties.

Au/Ag core-shell described in this chapter have been used for biological application, reporting astonishing potential due to the combination of both metal nanoparticles properties. A more detailed presentation of this application will be discussed in chapter 9.

3.5 References

(1) Corma, A.; Garcia, H. Supported Gold Nanoparticles As Catalysts for Organic Reactions. *Chemical Society Reviews,* **2008**, 37 (9), 2096−2126.

(2) Scaiano, J. C.; Netto-Ferreira, J. C.; Alarcon, E.; Billone, P.; Bueno-Alejo, C. J.; Crites, C. O. L.; Decan, M. R.; Fasciani, C.; Gonzalez-Bejar, M.; Hallett-Tapley, G. L.; Grenier, M.; McGilvray, K. L.; Pacioni, N. L.; Pardoe, A.; Rene-Boisneuf, L.; Narbonne-Schwartz, R.; Silvero, J.; Stamplecoskie, K. G.; Wee, T. L. Tuning Plasmon Transitions and Their Applications in Organic Photochemistry. *Pure and Applied Chemistry,* **2011**, 83, 913−930.

(3) Alarcon, E. I.; Udekwu, K.; Skog, M.; Pacioni, N. L.; Stamplecoskie, K. G.; Gonzalez-Bejar, M.; Polisetti, N.; Wickham, A.; Richter-Dahlfors, A.; Griffith, M.; Scaiano, J. C. The Biocompatibility and Antibacterial Properties of Collagen-Stabilized, Photochemically Prepared Silver Nanoparticles. *Biomaterials,* **2012**, 33 (19), 4947−4956.

(4) Burda, C.; Chen, X.; Narayanan, R.; El-Sayed, M. A. Chemistry and Properties of Nanocrystals of Different Shapes. *Chemical Reviews,* **2005**, 105 (4), 1025−1102.

(5) Eustis, S.; El-Sayed, M. A. Why gold Nanoparticles Are More Precious than Pretty Gold: Noble Metal Surface Plasmon Resonance and Its Enhancement of the Radiative and Nonradiative Properties of Nanocrystals of Different Shapes. *Chemical Society Reviews,* **2006**, 35 (3), 209−217.

(6) Tao, A. R.; Habas, S.; Yang, P. D. Shape Control of Colloidal Metal Nanocrystals. *Small,* **2008**, 4 (3), 310−325.

(7) Jana, N. R.; Gearheart, L.; Murphy, C. J. Seeding Growth for Size Control of 5−40 nm Diameter Gold Nanoparticles. *Langmuir,* **2001**, 17 (22), 6782−6786.

(8) Brown, K. R.; Walter, D. G.; Natan, M. J. Seeding of Colloidal Au Nanoparticle Solutions. 2. Improved Control of Particle Size and Shape. *Chemistry of Materials,* **2000**, 12 (2), 306−313.

(9) McGilvray, K. L.; Fasciani, C.; Bueno-Alejo, C. J.; Schwartz- Narbonne, R.; Scaiano, J.C. Photochemical Strategies for the Seed-Mediated Growth of Gold and Gold-Silver Nanoparticles. *Langmuir*, **2012**, 28, 16148−16155.

(10) Cao, L.; Zhu, T.; Liu, Z. Formation Mechanism of Nonspherical Gold Nanoparticles during Seeding Growth: Roles of Anion Adsorption and Reduction Rate. *Journal of Colloid and Interface Science,* **2006**, 293(1), 69−76.

(11) Meltzer, S.; Resch, R.; Koel, B. E.; Thompson, M. E.; Madhukar, A.; Requicha,

A. A. G.; Will, P. Fabrication of Nanostructures by Hydroxylamine Seeding of Gold Nanoparticle Templates. *Langmuir,* **2001**, 17 (5), 1713−1718.

(12) Scaiano, J. C.; Billone, P.; Gonzalez, C. M.; Maretti, L.; Marin, M. L.; McGilvray, K. L.; Yuan, N. Photochemical Routes to Silver and Gold Nanoparticles. *Pure and Applied Chemistry,* **2009**, 81 (4), 635−647.

(13) Zeng, Q. H.; Jiang, X. C.; Yu, A. B.; Lu, G. Q. Growth Mechanisms of Silver Nanoparticles: a Molecular Dynamics Study. *Nanotechnology,* **2007**, 18 (3), 255706.

(14) Jockusch, S.; Landis, M. S.; Freiermuth, B.; Turro, N. J., Photochemistry and Photophysics of α-Hydroxy Ketones. *Macromolecules*, **2001**, 34 (6), 1619-1626.

(15) Norrish, R. G. W., Appleyard, M. E. S., Primary Photochemical Reactions. Part IV. Decomposition of Methyl Ethyl Ketone and Methyl Butyl Ketone. *Journal of the Chemical Society.* **1934**, 874-880.

(16) McGilvray, K. L., Decan, M. R., Wang, D., Scaiano, J. C., Facile Photochemical Synthesis of Unprotected Aqueous Gold Nanoparticles. *Journal of American Chemical Society,* **2006**, 128, 15980-15981.

(17) Scaiano, J. C.; Stamplecoskie, K. G.; Hallett-Tapley, G. L. Photochemical Norrish Type I Reaction As a Tool for Metal Nanoparticle Synthesis: Importance of Proton Coupled Electron Transfer. *Chemical Communications,* **2012**, 48 (40), 4798−4808.

(18) Gonzalez, C. M.; Liu, Y.; Scaiano, J. C. Photochemical Strategies for the Facile Synthesis of Gold-Silver Alloy and Core-Shell Bimetallic Nanoparticles. *Journal of Physical Chemistry C,* **2009**, 113 (27), 11861−11867.

(19) Mallik, K.; Mandal, M.; Pradhan, N.; Pal, T. Seed Mediated Formation of Bimetallic Nanoparticles by UV Irradiation: A Photochemical Approach for the Preparation of "Core-Shell" Type Structures. *Nano Letters,* **2001**, 1 (6), 319−322.

(20) Rodriguez-Gonzalez, B.; Burrows, A.; Watanabe, M.; Kiely, C. J.; Liz Marzan, L. M. Multishell Bimetallic AuAg Nanoparticles: Synthesis, Structure and Optical Properties. *Journal of Materials Chemistry,* **2005**, 15(17), 1755−1759.

(21) Steinbruck, A.; Csaki, A.; Festag, G.; Fritzsche, W. Preparation and Optical Characterization of Core–Shell Bimetal Nanoparticles. *Plasmonics,* **2006**,1: 79–85.

(22) Hodak, J. H.; Henglein, A.; Giersig, M.; Harland, G. V. Laser-Induced Inter-Diffusion in AuAg Core-Shell Nanoparticles. *Journal of Physical Chemistry B,* **2000**, 104, 11708.

(23) Tsuji, M.; Matsuo, R.; Jiang,P.; Miyamae, N.; Ueyama, D.; Nishio, M.; Hikino, S.; Kumagae, H.; Nor Kamarudin,K. S.; Tang, Z.-L. Shape-Dependent Evolution of Au@Ag Core-Shell Nanocrystals by PVP-Assisted N,N-Dimethylformamide Reduction. *Crystal Growth & Design,* **2008**, 8, 2528-2536.

(24) Han, H.; Fang, Y.; Li, F.; Xu, H. Tunable Surface Plasma Resonance Frequency in Ag Core/Au Shell Nanoparticles System Prepared by Laser Ablation. *Applied Physics Letters.* **2008**, 92, 023116.

Chapter 4

High-Temperature Organic Reactions at Room Temperature Using Plasmon Excitation

4.1 Introduction

Nanoparticles of noble metals such as silver, gold, and copper have characteristic colors due to the presence of plasmon absorption. Upon excitation, the surface plasmon band (SPB) can be viewed as a collective motion of electrons that result in transient polarization of the particle.[1,2] It has been recently recognized that metal nanoparticles plasmon transitions can provide a mechanism to deliver energy to molecules in their proximity. The energy delivered through these transitions can form excited states, or simply provide "thermal" energy to molecules in the proximity of the particle surface.[3,4] In the latter scenario, high temperature reactions can formally occur at or near room temperature. Nonetheless, concerns related to the possibility for a certain molecules to approach the nanoparticle surface need to be taken under consideration; in addition,

assuming that a molecule can be placed within proper distance from the nanoparticle, several other aspects need to be considered in order to perform a thermal process using plasmon transitions. Two main questions can be formulated: which is the thermal energy that the plasmon excitation can provide? And therefore, which high-energy transformations could be triggered at room temperature by using plasmon transitions? In order to answer these questions, the principal goal in this work was to identify the range of temperatures that can be reached by irradiating nanoparticles with visible light. Due to the nanometer size of the material it is very difficult to measure directly the amount of thermal energy released after plasmon irradiation. Moreover, time resolved-studies indicated that energy is released from the nanoparticle in less than 1 ns[5,6] and fast dissipation of that energy makes impossible to sense an increase of the bulk solution temperature. The identification of the temperatures that can be reached upon excitation of the metal nanoparticles SPR band is paramount for any further thermal catalytic application. Our goal was to find an alternative and more versatile way to obtain this information; for this purpose, we investigated the thermal decomposition of dicumyl peroxide (DCP) as a test reaction. This system was used as a "molecular thermometer", meaning that the temperature reachable by plasmon excitation was identified according to the conversion of dicumyl peroxide, as reported in the following pages.

4.2 Materials and Methods

4.2.1 Materials

Tetrachloroaurate and dicumyl peroxide were purchased from Sigma-Aldrich and used as received. I-2959 was obtained as generous gift form BASF supplied by Dempsey Corporation Canada and recrystallized by ethanol. Gold nanoparticles with a main diameter of 12 nm and a typical concentration of 1 nM were prepared photochemically, according to a procedure reported in literature and described in the previous chapters (chapter 1: paragraph 1.2; chapter 3: paragraph 3.2.2).[7]

4.2.2 Laser drop experiment

The laser drop system was optimized from an existing system, previously customized in the Scaiano group.[8] For the description of the laser drop setup referred to Chapter 2, paragraph 2.1.1. In a typical experiment a mixture of AuNP and dicumyl peroxide (1 mM) was introduced in a 10 ml syringe and forced to pass through a teflon tube, forming a drop in the opposite side. The experiments were conducted in H_2O with 5% of MeOH, and the samples were irradiated with different number of shots per drop. The resulting solution was collected using a cuvette placed below the teflon tube (Figure 4.1).

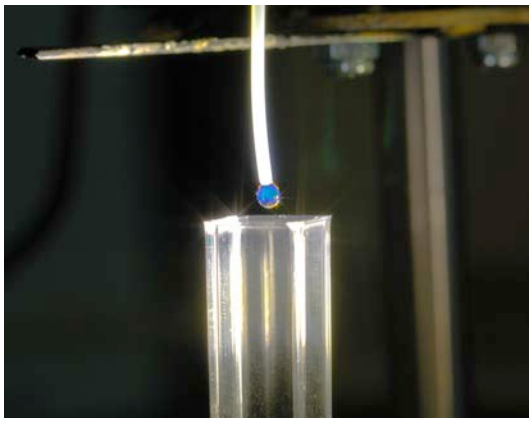

Figure 4.1 Picture of the solution drop irradiated using the laser drop system.

4.3 Decomposition of Dicumyl Peroxide

In order to have a better understanding of the light-to-heat conversion achievable upon plasmon excitation, AuNP were tested as catalyst in the decomposition of dicumyl peroxide (Scheme 4.1). The choice of AuNP within the other metal nanoparticles (AgNP or CuNP) was based on the superior stability of gold versus oxidation. The reaction chosen is quite endothermic; indeed, at room temperature, dicumyl peroxide is stable for months, but can be thermally or photochemically decomposed.[9,10] The photochemical process requires ultraviolet irradiation to trigger the reaction. On the other side,

prolonged heating at temperature higher then 140°C are needed to thermally decompose the dicumyl peroxide.

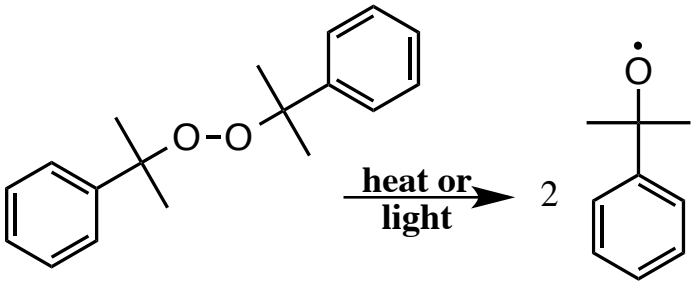

Scheme 4.1 Dicumyl peroxide dissociation.

The activation energy of the process can be estimated by using Arrhenius parameters derived from lifetime data in the temperature range of 128-158 °C and published by Kharasch in 1951.[11] Figure 4.2 shows the resulting plot, where *k* is the rate constant of the dissociation process and T is the temperature. A value of 34.2 Kcal/mol has been estimated as the activation energy required for the decomposition of the DCP and it is attributed to the dissociation of the peroxide bond.

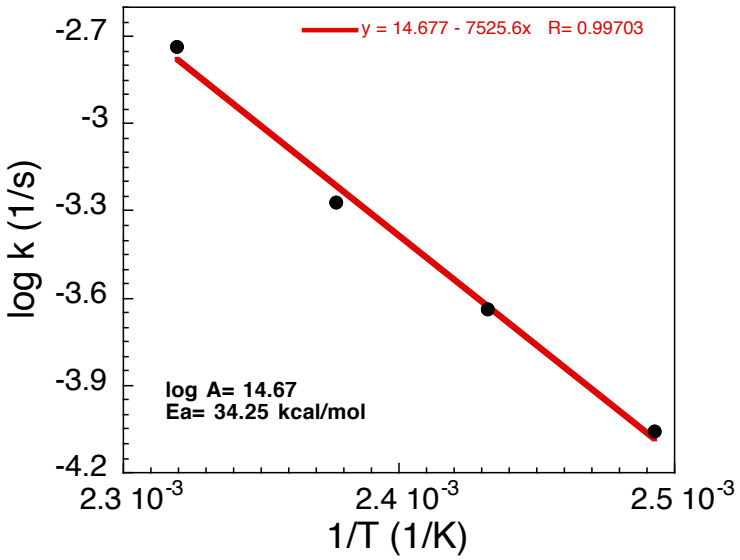

Figure 4.2 Arrhenius plot for the dicumyl peroxide decomposition.

This reaction represents an excellent candidate to challenge the limits of plasmon heating effects, and can be used as a "thermometer" to identify the temperature ranges achievable after plasmon irradiation of metal nanoparticles. After the initial decomposition, two pathways are possible, as reported in the Scheme 4.2.

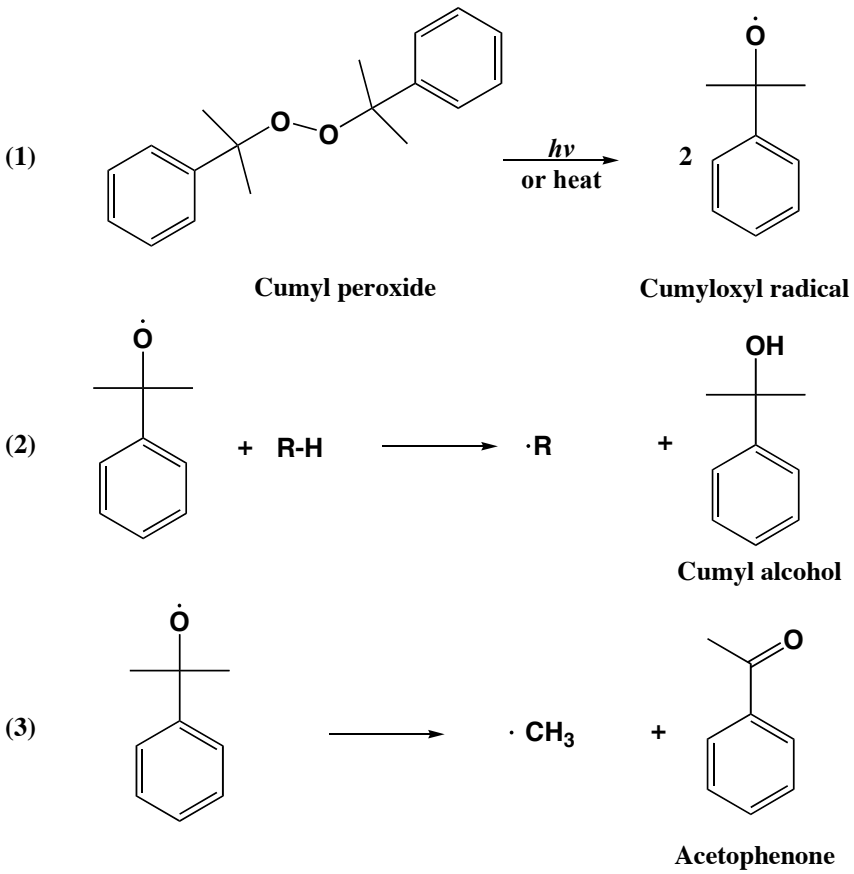

Scheme 4.2 Formation and possible pathways of cumyloxyl radicals.

The cumyloxyl radical, obtained after the initial decomposition, can lead to the formation of cumyl alcohol, in the presence of a hydrogen donor (i.e. methanol, reaction 2), or acetophenone (reaction 3).[10]

For the investigation of this particular thermal reaction using plasmon irradiation we employed AuNP largely unprotected. Those AuNP absorb light right around 530 nm, corresponding to the green light in the middle of the visible spectrum (Figure 4.3).[7]

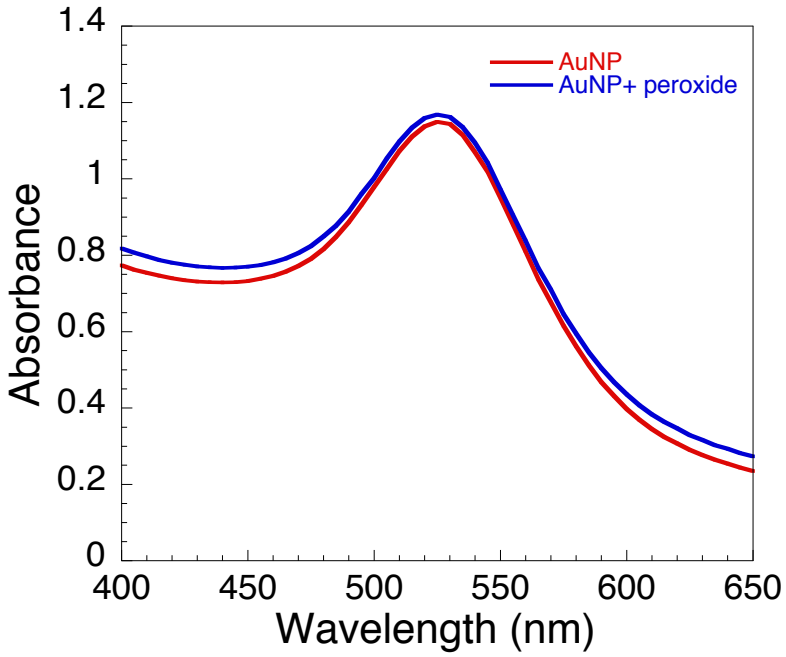

Figure 4.3 UV spectrum of AuNP Plasmon band with and without dicumyl peroxide.

The reaction was performed using the laser drop system described before and analyzed by HPLC, collecting the products at different amount of shots per drop (s/d). Pictures of the sample before, during and after few milliseconds of 532 nm laser excitation were recorded; as reported in Figure 4.4, a change in color, towards a blue tint, can be noted. The blue shift observed can be attributed to a surface modification or aggregation of the nanoparticles, however it persists just few milliseconds during irradiation and it does not remain after the experiment.

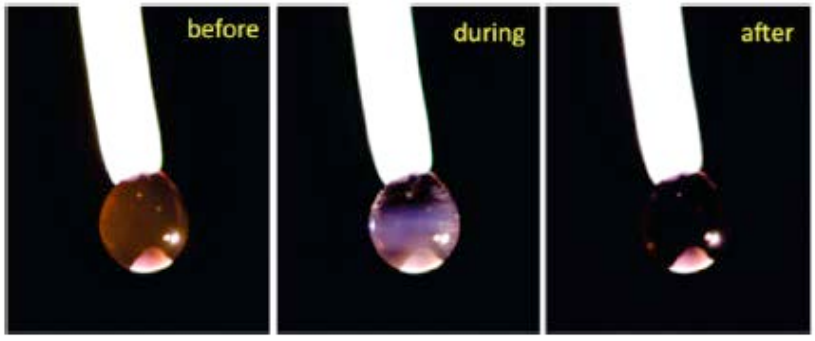

Figure 4.4 Laser drop pictures before, during, and a few milliseconds after 532 nm laser excitation. Note a slight bluish tint during excitation.

A typical HPLC trace is reported in Figure 4.5 and shows the result obtained collecting the solution after 50 laser pulses per drop.

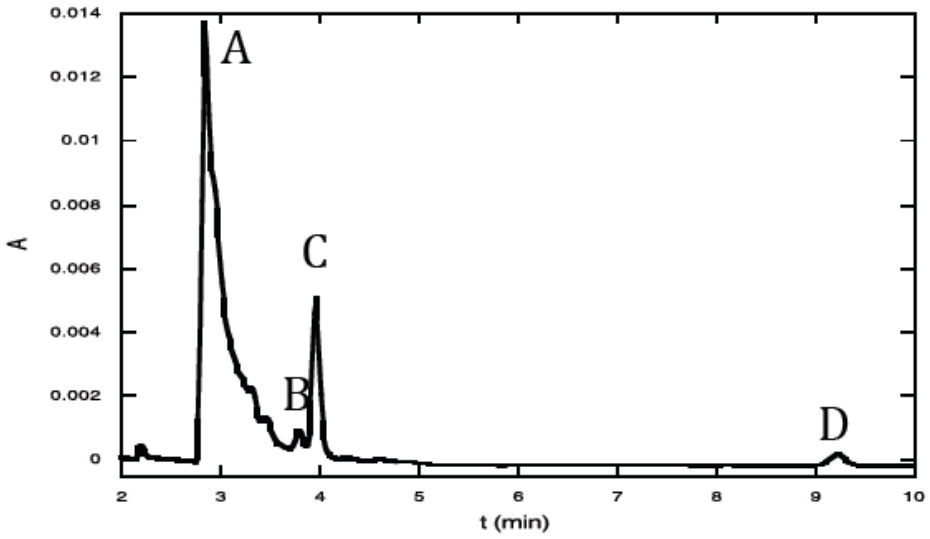

Figure 4.5 HPLC traces of the experiment after 50 shots per drop irradiation. The peaks observed were attributed as follows: A- AuNP solution (4-HEBA, I-2959 remaining in solution); B- 2-phenyl-2-propanol; C- Acetophenone; D- Dicumyl peroxide.

In addition to the starting material, dicumyl peroxide (peak D), and the two possible products, 2-phenyl-2 propanol (peak B) and acetophenone (peak C), a peak attributed to 4-HEBA and the leftover I-2959 can be also observed (peak A).

The results of the different laser drop experiments are summarized in Figure 4.6. In the presence of AuNP, complete conversion of the peroxide is obtained after approximately 75 laser shots. However, in absence of AuNP, more than 60% of peroxide still remains even after 200 shots per drop. (Figure 4.6) When the experiments are conducted using a 5% and 0.5% methanol the only product isolated was 2-phenyl-2-propanol, in fact the required condition under which acetophenone was detected was that no hydrogen donor was present in solution.

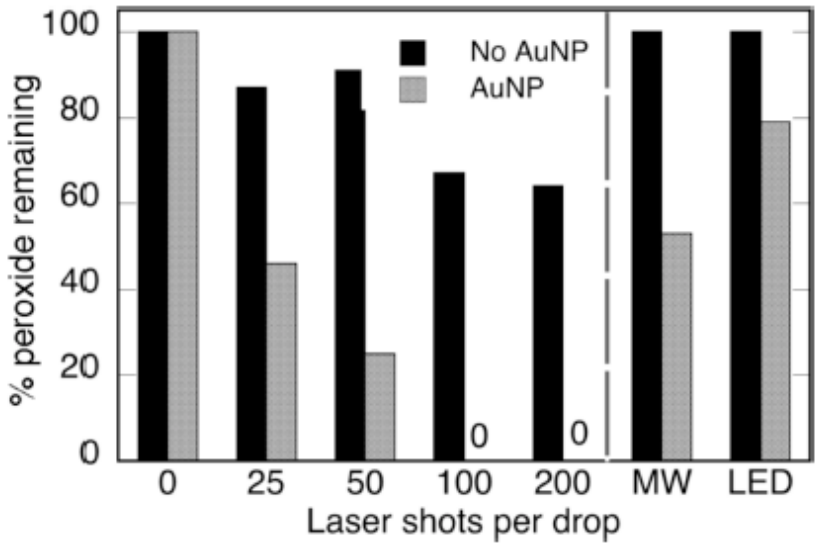

Figure 4.6 Graph of conversion *vs.* number of shots per drop of 1 mM dicumyl peroxide in H_2O with 5% of MeOH irradiated with a 532 nm laser (50 mJ/shot) with different number of shots per drop (0, 25, 50, 100, 200 s/d). The right panel in the graph shows the results using a microwave (300 W, 20 min) and a 530 nm set of LED (4 x 15 W, 35 °C, 60 min).

The data obtained clearly indicate that the presence of AuNP is essential to perform the decomposition of dicumyl peroxide. In other words, we are assisting to a photothermal effect produced by the excitation of the plasmon absorption band.

In order to confirm these observations, comparison with other techniques such as microwave (MW) and LED were performed. In the first case, solutions of DCP with and without AuNP were irradiated in a microwave for 20 min at 300 W, reaching a bulk solution temperature of 80°C. No conversion was observed in absence of AuNP; nonetheless, a 47% conversion was obtained when AuNP were present in the solution vessel. Those results proved that temperatures of 80°C are not sufficient to perform the dissociation unless in presence of AuNP. Indeed, AuNP are good microwave absorbers, thus some conversion is possible. Interestingly, the conversion obtained after 20 min of microwave irradiation in the presence of AuNP, equal to 47%, does not reach the same value of conversion obtained using the laser irradiation after only 25 s (25 shots/drop), which is equal to 55%.

The effect of the AuNP was also confirmed by performing the reaction using 530 nm

LED irradiation. The experiments were conducted for 1 h, at 35°C, employing a total light power of 60 W (4 LED x 15 W each). Despite the lower power used compared to the laser drop system, 21% of conversion was obtained in presence of AuNP; instead, in absence of AuNP, 100% of peroxide remained in the mixture. The LED experiments, other than confirming the photothermal effect exerted by the metal nanoparticles, represent also an inexpensive alternative to catalyze organic reaction using plasmon irradiation. The comparison between laser drop, microwave and LED are reported in Figure 4.6. The evolution of the bulk solution temperature during LED irradiation was monitored using a thermocouple. After an initial increase, the temperature remained stable at about 40°C during the all experiment.

4.4 AuNP morphology before and after laser drop treatment

The study of the plasmon-mediated effect of AuNP in the decomposition of dicumyl peroxide appears to be very promising, especially when using the laser drop apparatus. However, possible modification in the AuNP structure could occur. Figure 4.7 shows the colors of a AuNP [1.4 nM] and DCP [1 mM] solution before and after laser irradiation. The initial solution is characterized by a bright pink tint due to the plasmon band absorption of the AuNP, but an attenuation of that color is obtained after the laser treatment. This variation is probably related to the formation of smaller AuNP, generated by an ablation process and resulting in a weaker plasmon transition.

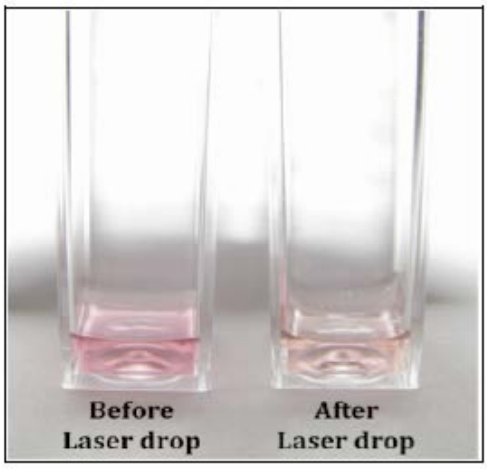

Figure 4.7 Pictures of AuNP and DCP solution before and after laser drop irradiation.

Indeed, laser ablation phenomena are likely to occur when metal nanoparticles are irradiated using visible light.[12] In the last few years several works have been published regarding this matter, including a recent contribution from the Scaiano's group which describes the possibility of functionalizing or modifying AuNP surface using laser ablation.[13] In order to further investigate the effect of the light on the AuNP morphology during the decomposition of dicumyl peroxide, we analyzed the sample before and after irradiation using SEM microscopy. The size of the AuNP in the initial solution is 12 nm on average, as confirmed by analyzing more than 100 particles from representative SEM pictures. As expected, the size is drastically reduced to one forth, reaching an average value of 4 nm, after 50 laser shots. The same effect is observed when DCP is present in the AuNP solution, going from an average diameter of 12.7 nm to 3 nm, after 100 shots per drop. (Figure 4.8)

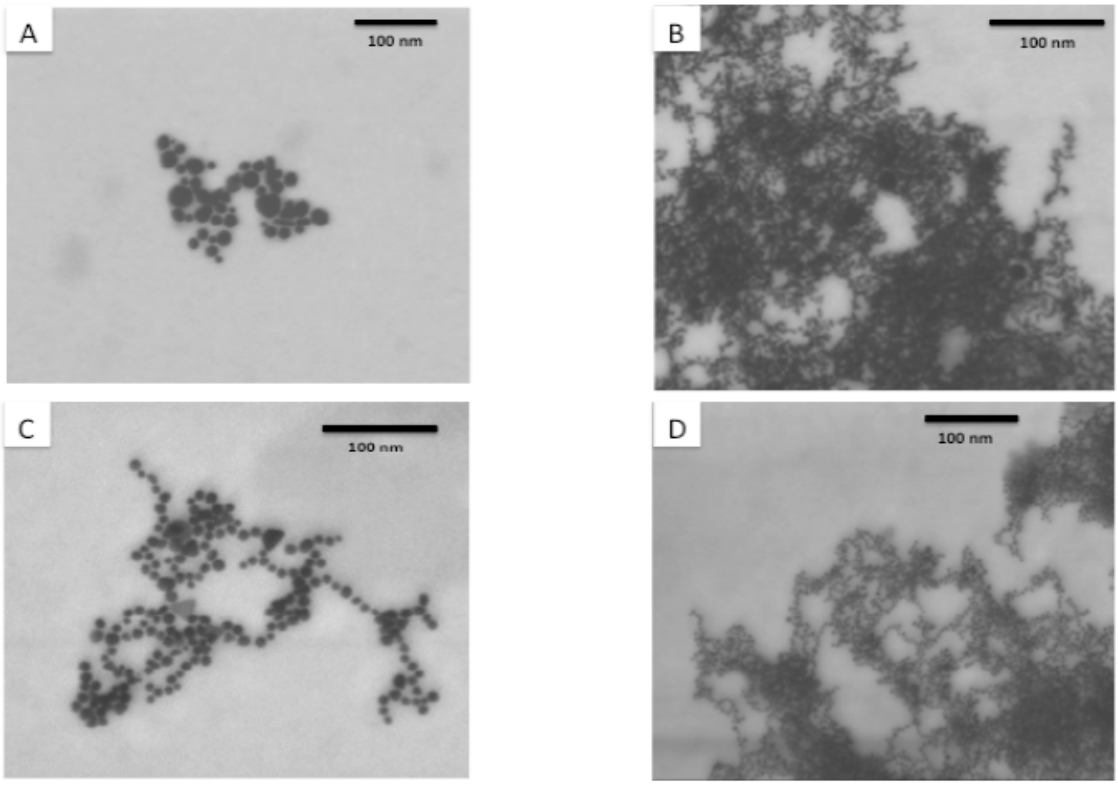

Figure 4.8 SEM images of AuNP before (A: in presence of DCP; C: in absence of DCP) and after (B: in presence of DCP; D: in absence of DCP) ablation.

This observation returns useful in the investigation of the temperature range achievable after plasmon irradiation, as results in the next section.

4.5 Plasmon mediated energy release: from practice to theory

According to the results obtained, the decomposition of dicumyl peroxide seems to be a feasible process when catalyzed by SPB photoexcitation; however, a study of the temperature limits related to this methodology need to be performed. In order to address this aspect, several calculations and observations need to be taken into account. As a first approach, we decided to identify the possible increase of temperature attributed to the bulk heating of the solution, rather then the plasmon photothermal effect. We based our approach on the assumption that our system is adiabatic, an approximation that appear to be good only considering a single drop, and not realistic for a minutes lasting

experiment. Knowing the volume of a drop, corresponding to 7 μl, the heat capacity (C_p) and density of water, we estimated a bulk heating of 1.7 K for 50 mJ laser pulse, according to equations 4.1 and 4.2.

$$\Delta T(K) = \frac{energy(J)}{C_p(J/gK) \times mass(g)} \tag{4.1}$$

$$\Delta T(K) = \frac{0.05J}{4.2(J/gK) \times 0.007(mL) \times 1.0(g/mM)} \cong 1.7K \tag{4.2}$$

This low value is in accordance with the high stability of DCP observed during the microwave experiments and corroborates our idea that bulk heating of the drops cannot explain the chemistry observed.

Once the bulk heating of the solution has been ruled out as the responsible for the decomposition of DCP, we moved on considering the contribution of the AuNP plasmon excitation. In this prospective we assumed that AuNP could act as an adiabatic units themselves, meaning that they did not exchange heat with the surrounded medium during the laser pulse (8 ns). Considering AuNP as an ideal gas, an extreme limit of the temperature reachable after plasmon excitation can be obtained by using equation 4.1 and considering that each drop (7 μL) contains around 10^{-7} g of gold. The calculation gave us a $\Delta T > 10^6$ K, a value that stays in the same order if we consider an incomplete absorption of the light (absorbance ~0.05 in the drop) and it appears extremely unrealistic, probably due to the assumption done.

We considered at this point that the AuNP used in this experiment undergo some surface modification after laser treatment, as shown in the previous section. This observation suggests that temperatures near the melting point are achievable. Indeed, it is well known that the melting point of metal nanoparticle is lower than the melting point of the corresponding metal bulk material, and in the case of bulk gold the melting point is 1337 K, while for 12 nm AuNP the value is estimated to be around 1200 K.[14]

With that in mind, we can state that high temperature, lower than the melting point of AuNP, can be reached after plasmon excitation. As an extreme temperature limit we can,

therefore, fix a value below 1200 K.

The temperature range can be reduced, by considering the results obtained during the laser drop experiment. The idea is to relate the conversion obtained at each shot per drop to the amount of energy that the dicumyl peroxide need to "feel" in order to give that conversion. We were able to calculate the activation energy (E_a= 34.3 kcal/mol) and the pre-exponential factor (4.7 x 10^{14} s^{-1}) relative to the dicumyl peroxide dissociation by looking at the kinetic data reported in literature.[11] Therefore, from those parameters, the Arrhenius equation can be applied to obtain the rate constant as a function of the temperature, as reported in Figure 4.9.

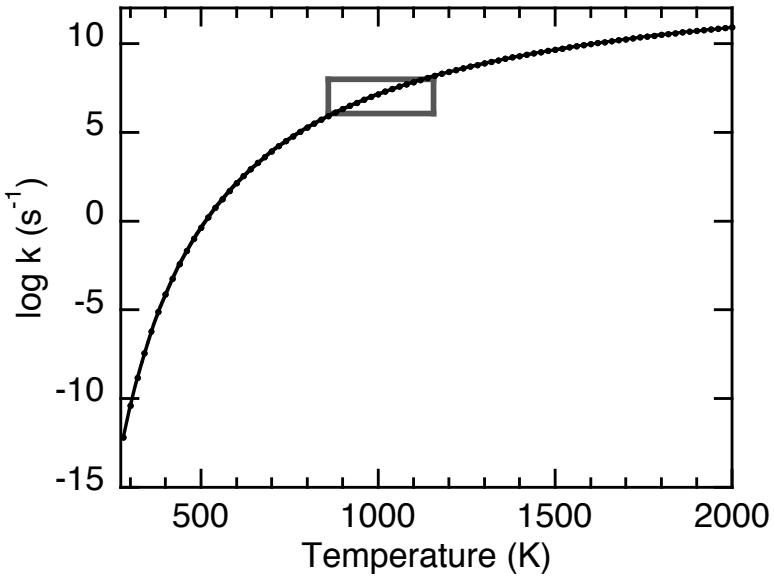

Figure 4.9 Calculated rate constant for the decomposition of the dicumyl peroxide at various temperatures, based on E_a=34.25 kcal/mol and log A=14.67. The rectangle shows the range of temperatures where the lifetime of DCP would be between 10 ns and 1 μs.

Our empirical results showed that 100% of conversion is obtained after around 75 shots, meaning that at each laser pulse 1.3% of dicumyl peroxide is decomposed. Assuming that the SPR heating lasted 100 ns around the AuNP, we can conclude that a temperature value of around 760 K was "sensed" by the DCP, as reported in the following calculation:

$$\log\frac{C_o}{C} = \log\frac{100}{98.7} = 0.0057 = kt = k \times 10^{-7} s \Rightarrow k = 57000 s^{-1} \quad (4.3)$$

$$\log(57000) = 14.67 = \frac{34250}{2.3 \times R \times T} \Rightarrow T \approx 760K \quad (4.4)$$

As specified above, this result is referred to a plasmon effect lasting 100 ns; nonetheless, if we extend the same approach from 10 ns to 1 ms, the temperature range required to have a 1.3% of conversion after each laser shot is between 680 and 830 K. This temperature range must be considered as an indication, in other words it represents a "nominal" temperature required to have the decomposition of peroxide happening. Moreover, the data obtained were plotted as an exponential decrease curve from which we obtained a conversion of 1.7% after the very first laser pulse. A value for which the temperature range identified remains still valid.

It also has to be noticed that the value obtained is based on the assumption that all DCP molecules are exposed to the plasmon energy released by the AuNP. However, not all the reactant molecules are likely placed on the right distance from the AuNP surface, and as a consequence the temperature values obtained are lower than the one expected to have the same conversion for a reduced amount of DCP exposed to AuNP. In addition, our calculation is based on the assumption that the dicumyl peroxide interaction with AuNP does not affect the peroxide dissociation energy, and therefore that the AuNP does not act as a conventional catalyst.

4.6 Summary

In conclusion, the analysis of the dicumyl peroxide decomposition by plasmon irradiation of AuNP gave us a nominal temperature range achievable. With our experiment we proved that an unimolecular process, requiring activation energies around 35 kcal/mol, can be performed employing SPR excitation of AuNP, even when the molecules studied are not covalently bound to the surface of the particles. Values around 500°C ± 100°C, for a submicrosecond times of irradiation, were obtained. El-Sayed et al.

reported temperatures >80°C during cancer cell treatment with AuNP.[15] Therefore, our contribution represents the first attempt to identify a range of temperatures for plasmon-assisted photothermal effect in organic chemistry and can serve as an indication to select organic reactions that could be performed with this methodology. The laser drop setup was paramount in the study of the system selected, however, for practical application, LED light sources represent a convenient and promising alternative for the catalysis of thermal reaction using plasmon-mediated energy delivery. The possibility to use these inexpensive sources of light, in addition to the possibility to use plasmon-assisted catalysis processes have been explored in other projects during my PhD. Nonetheless, the decomposition of dicumyl peroxide represents a fundamental achievement for my research since it provided the required knowledge to thoroughly investigate plasmon-mediated energy release effect and its application in several fields. Examples in catalysis, lithography and biochemistry will be presented in the following chapters.

4.7 References

(1) Burda, C., Chen, X., Narayanan, R., and El-Sayed, M. A. Chemistry and Properties of Nanocrystals of Different Shapes. *Chemical Reviews,* **2005**, 105, 1025-1102.

(2) Eustis, S., and El-Sayed, M. A. Why Gold Nanoparticles are More Precious than Pretty Gold: Noble Metal Surface Plasmon Resonance and its Enhancement of the Radiative and Nonradiative Properties of Nanocrystals of Different Shapes. *Chemical Society Reviews,* **2006**, 35, 209-217.

(3) Bakhtiari, A. B. S., Hsiao, D., Jin, G., Gates, B. D., Branda, N. R. An Efficient Method Based on the Photothermal Effect for the Release of Molecules from Metal Nanoparticle Surfaces. *Angewandte Chemie International Edition,* **2009**, 48, 4166-4169.

(4) Pacioni, N. L., González-Bejar, M., Alarcón, E., McGilvray, K. L., and Scaiano, J. C. Surface Plasmons Control the Dynamics of Excited Triplet States in the Presence of Gold Nanoparticles. *Journal of American Chemical Society,* **2010**, 132, 6298-6299.

(5) Hu, M.; Hartland, G. V. Heat Dissipation for Au Particles in Aqueous Solution: Relaxation Time versus Size. *Journal of Physical Chemistry B,* **2002**, 106, 7029–7033.

(6) Mohamed, M. B.; Ahmadi, T. S.; Link, S.; Braun, M.; El-Sayed, M. Hot Electron and Phonon Dynamics of Gold Nanoparticles Embedded in Gel Matrix. *Chemical Physics Letters,* **2001**, 343, 55–63.

(7) Marin, M. L., McGilvray, K. L., and Scaiano, J. C. Photochemical Strategies for the Synthesis of Gold Nanoparticles from Au(III) and Au(I) Using Photoinduced Free Radical Generation. *Journal of American Chemical Society,* **2008**, 130, 16572-16584.

(8) Banks, J. T.; Scaiano, J. C. The Laser-Drop Method: A New Approach To Induce Multiple Photon Chemistry with Pulsed Lasers. Examples Involving Reactions of Diphenylmethyl and Cumyloxyl Radicals. *Journal of American Chemical Society,* **1993**, 115, 6409–6413.

(9) Baignée, A., Howard, J. A., Scaiano, J. C., and Stewart, L. C. Absolute Rate Constants for Reactions of Cumyloxy in Solution. *Journal of American Chemical Society,* **1983**, 105, 6120-6123.

(10) Neville, A. G., Brown, C. E., Rayner, D. M., Lusztyk, J., and Ingold, K. U. Direct Measurement of the Rate Constant for b-Scission of the Cumyloxyl Radical by Laser Flash Photolysis with Time Resolved IR Detection. *Journal of American Chemical Society,* **1989**, 111, 9269-9270.

(11) Kharasch, M. S.; Fono, A.; Nudenberg, W. The Chemistry of Hydroperoxides. v. the Thermal Decomposition of Tert-alkyl Peroxides. *Journal of Organic Chemistry,* **1951**, 16, 105–112.

(12) Boyer, P.; Ménard, D.; Meunier, M. Nanoclustered Co/Au Particles Fabricated by Femtosecond Laser Fragmentation in Liquids. *Journal of Physical Chemistry C,* **2010**, 114, 13497−13500.

(13) Bueno-Alejo, C. J.; D'Alfonso, C.; Pacioni, N. L.; González-Béjar, M.; Grenier, M.; Lanzalunga, O.; Alarcon, E. I.; Scaiano, J. C. Ultraclean Derivatized Monodisperse Gold Nanoparticles through Laser Drop Ablation Customization of Polymorph Gold Nanostructures. *Langmuir,* **2012**, 28, 8183−8189.

(14) Dick, K.; Dhanasekaran, T.; Zhang, Z.; Meisel, D. Size-Dependent Melting of Silica Encapsulated Gold Nanoparticles. *Journal of Organic Chemistry***, 2002**, 124, 2312–2317.

(15) El-Sayed, I. H.; El-Sayed, M. A. Determination of the Minimum Temperature Required for Selective Photothermal Destruction of Cancer Cells with the Use of Immunotargeted Gold Nanoparticles. *Photochememistry and Photobiology,* **2006**, 82, 412–417.

Chapter 5

Plasmon-Mediated Catalysis: Resazurin Reduction

5.1 Introduction

As reported in the previous chapters, noble metal nanoparticles possess peculiar optical and physical properties. Among all of them, the possibility of releasing thermal energy after plasmon excitation represents a promising feature. After identifying a temperature range reachable by irradiation of spherical AuNP,[1] our next interest was focused on the application of that thermal energy release in catalysis. A plasmon-mediated oxidation process using LED irradiation of AuNP was investigated by other members of the Scaiano group.[2] To further explore the potential of the plasmon-mediated catalysis, we decided to study a reduction process employing different irradiation techniques, such as laser drop and LED. For this purpose, we chose the reduction of resazurin, also known as Alamar Blue,[3] to resorufin (Scheme 5.1), which is a very well known process and has been thoroughly studied in the past.[4-8]

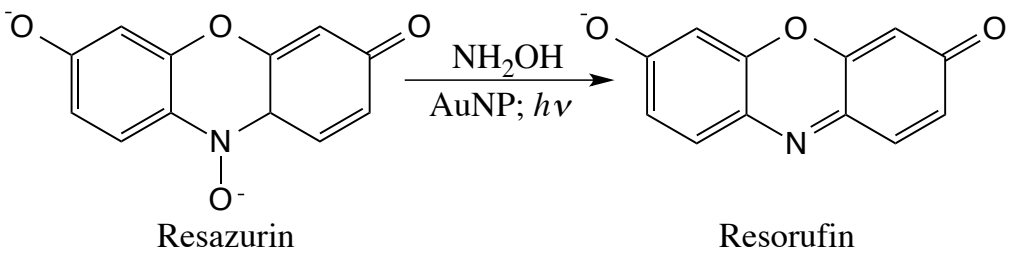

Scheme 5.1 Resuzurin reduction.

The choice of this reaction is due to the fact that this process can be easily followed either using colorimetric methods, as the color changes from blue (resazurin λ_{max}= 603 nm) to pink (resorufin λ_{max}= 570 nm) (Figure 5.4), or by analysis of the high fluorescence emission of resorufin (λ_{em}= 582 nm) compared to the weak emission of resazurin[3-5] (Figure 5.1).

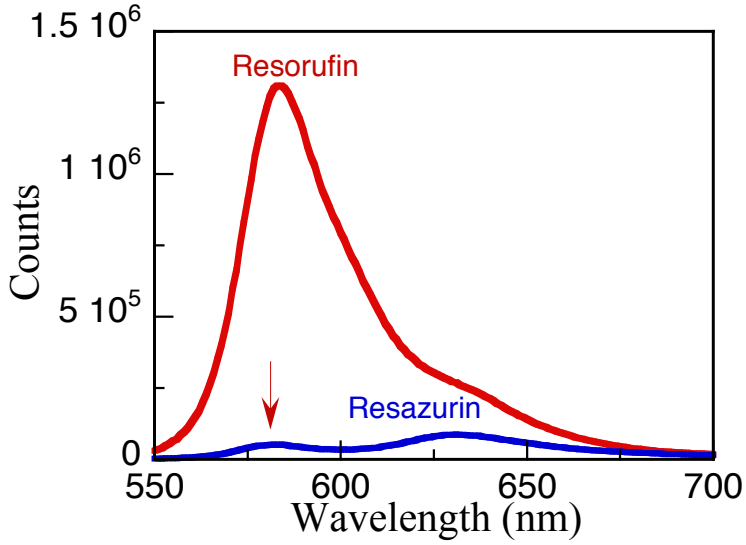

Figure 5.1 Fluorescence emission spectra for resazurin (blue) and resorufin (red). Both solutions were diluted to 0.1 absorbance at the excitation wavelength (532 nm) under basic conditions. The red arrow indicates the emission due to traces of resorufin in the resazurin sample.

This reaction can be performed using several methods such as photochemical, electrochemical or biocatalytic methods, to name a few.[5-7] Lately, Bueno et al. described a photoreduction of resazurin to resorufin using different types of amines upon irradiation at 615 nm.[8]

In our attempt we use AuNP as catalyst and hydroxylamine as reducing agent, in order

to verify if a plasmon-mediated catalysis process, at room temperature, was feasible for this specific reduction. Previous contributions reported the use of AuNP in the catalytic reduction of resazurin, however they adopted electrochemical methods to perform this transformation. Moreover, they were able to follow the fate of the reaction by using single molecule fluorescence on the surface of the metal nanoparticles.[9-10]

In our work, we used LED irradiation and laser-drop excitation, a technique developed in our group,[1,11] to irradiate the plasmon band of AuNP and we compared those results with the use of conventional heating techniques, such as microwave irradiation and thermal bath. In addition, a comprehensive study on the resorufin fluorescence emission quenching by AuNP has been performed in order to have a better understanding of the interaction between the metal nanoparticle and the fluorescent system analyzed.

5.2 Materials and Methods

5.2.1 Materials

Resazurin, resorufin, hydroxylamine, and tetrachloroaurate were purchased from Aldrich and used as received. Irgacure 2959 was a gift from BASF supplied by Dempsey Corporation Canada and it was recrystallized from ethyl acetate. All the solutions were prepared in Millipore water (resistivity 18.2 MW at 25°C).

5.2.2 Sample preparation

In a typical experiment, 200 μL of a 10 mM solution of resazurin (6.3 mg in 2.5 mL of water) and 40 μL of a 0.1 M solution of NH_2OH in water were added to AuNP solution (1.76 mL, 1.4 nM). Spherical AuNP, with a mean diameter of 13 nm and a SPB absorption at 530 nm (Figure 5.2), were prepared photochemically as reported in the previous chapters (chapter 1: paragraph 1.2; chapter 3: paragraph 3.2.2).[12]

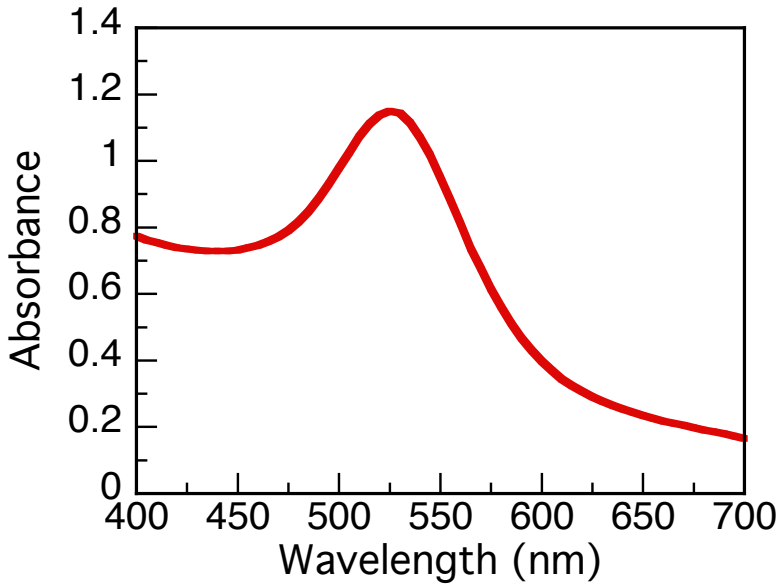

Figure 5.2 AuNP [1.4 nM] absorption spectrum.

The resulting solution of resazurin, NH_2OH and AuNP was irradiated using different light sources as follows.

5.2.3 Laser drop experiment

For this specific project two different laser powers (50 and 80 mJ per pulse) and different numbers of shots per drop (1 and 10) were used. When 10 shot per drop were used for irradiating the sample, the laser beam was not focused on the drop, this detail is important since when the laser is concentrated and focused, the drop is destroyed after only 1 shot, Figure 5.3 illustrates how, when the laser beam is focused on the drop, an explosion occurs after a single shot.

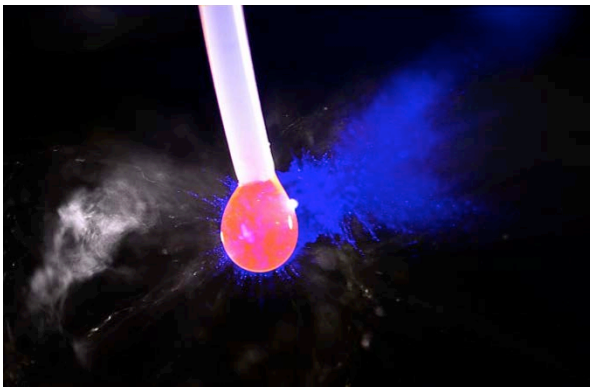

Figure 5.3 Explosion of the drop after a single focused laser shot. The camera exposure aperture time is of 1 s, therefore, in the picture we have the superimposition of the initial drop and the splashed drop after the laser shot. The fluorescence emission can be observed on the drop, as a result of the laser irradiation at 532 nm. However, the droplets appear blue due to the use of a blue flash (355 nm).

The irradiated samples were collected in a cuvette and analyzed after addition of NaOH to ensure a basic pH.

5.2.4 Light emitting diodes

In this experiment 1 mL of solution was placed in a cuvette of 0.5 x 0.5 cm path. The sample is centered in the LED irradiator and is irradiated to induce the reduction of resazurin to resorufin. To follow the reaction aliquots were taken every 2 min.

5.2.5 Microwave

The solution was placed in a CEM 10 mL Pyrex reaction tube and sealed with a Teflon cap; each sample was irradiated for 20 min at 80 ºC.

5.2.6 Sample analysis

The irradiated samples were diluted to an absorbance of 0.1 at 532 nm, using Cary-50-Bio UV-visible spectrophotometer and then analyzed recording the product emission spectrum, using a Photon Technology International (PTI) spectrofluorimeter. AuNP morphology before and after laser irradiation was analyzed using electron microscopy (see Appendix, Figure 5.18).

5.3 Reduction of Resazurin to Resorufin Catalyzed by Gold Nanoparticles

As reported in the in the previous paragraph, solutions containing 1 mM resazurin and an excess of NH_2OH in water were added to aqueous solution of AuNP, synthesized photochemically.[12] The solution was irradiated using the laser drop system, exciting the surface plasmon band at 532 nm. Interestingly, after each shot we noticed an instantaneous change of the drop color, going from red to orange. Pictures and videos of the drop color change were taken during the experiment. Figure 5.4 shows the emission color variation during a single laser shot.

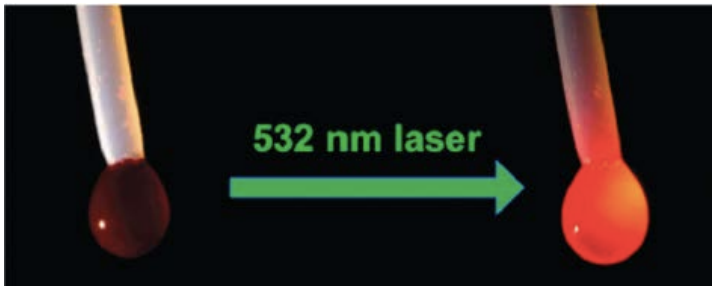

Figure 5.4 Pictures of the drop before (resazurin) and during laser excitation (resorufin); the bright point on the left of the drops is due to a reflection of the light source illuminating the drop, and the bright orange color of the right drop incorporates extensive product fluorescence.

The solution obtained collecting the irradiated drops in a cuvette was diluted to an absorbance equal to 0.1 at 532 nm and subsequently analyzed with a spectrofluorimeter. The percentage of resorufin fluorescence emission is reported as an indication of the completeness of the reaction. A quantitative conversion of resorufin to resazurin, corresponding to an intense emission of the product, is observed after a single shot of irradiation (Figure 5.5 b). The apparently different conversion obtained after 10 shots is due to experimental errors and reproducibility factors, since the experiments were run on different days.

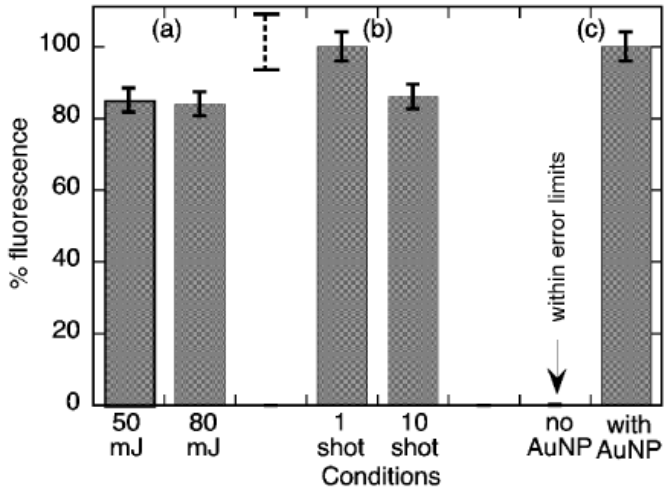

Figure. 5.5 Percent fluorescence emission increment relative to the maximum fluorescence emission of resorufin (λ = 582 nm) for three different experiments: (a) different laser energies (1 s/d); (b) different number of shots (50 mJ per pulse); (c) absence and presence of AuNP (50 mJ per pulse, 1 s/d); conditions for the experiments: resazurin 1 mM, NH_2OH 2 mM and AuNP 1.4 nM, exception made for the control where AuNP were not employed. The individual error bars in each column show the errors within a single set of experiments, while the dashed error bar shows the reproducibility between different sets of experiments ('a', 'b' and 'c'), frequently run on different days.

To further investigate the effect of the setup conditions on the resazurin conversion, we vary the laser pulse energy used from 50 to 80 mJ, keeping the number of laser shots constant (Figure 5.5 a). No difference in the fluorescence emission was observed; indicating that the energy applied with a 50 mJ single pulse is enough to get full conversion of resazurin to resorufin.

Furthermore, in the absence of AuNP no emission of the product was detected (Figure 5.5 b). The complete inefficiency of the reaction in absence of AuNP was observed despite the fact that the resazurin solution at the high concentration used has a reasonable absorption at 532 nm (Figure 5.6).

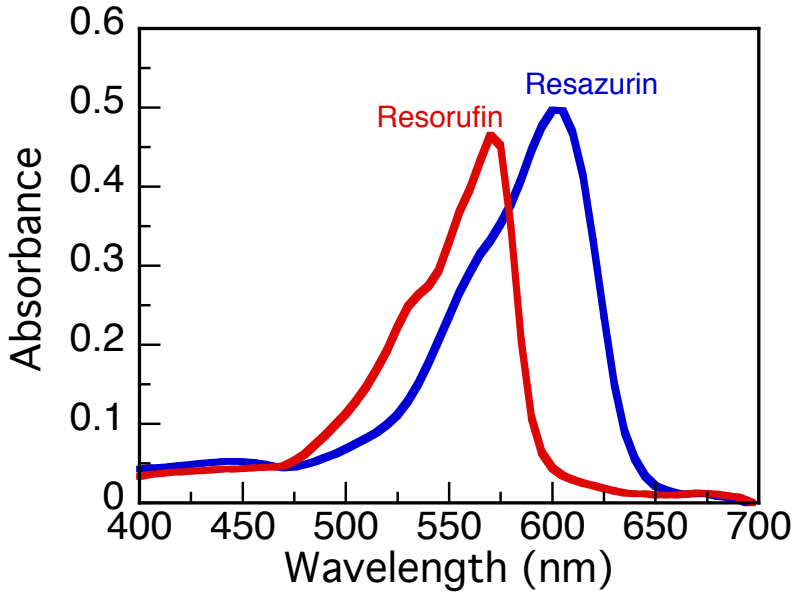

Figure 5.6 Absorption spectra of resazurin and resorufin at 0.001 mM concentration.

The fluorescence spectra corresponding to the results mentioned until now are reported in the Appendix at the end of the chapter.

From the different experiments performed, the resazurin reduction appears to be a very efficient process when performed in presence of AuNP using the laser drop technique. Indeed, with a single 10 ns laser pulse, 50,000 to 100,000 resazurin molecules are reduced per AuNP, using a laser pulse of 50 mJ. This surprising result proves that a plasmon-mediated catalysis can be performed in a nanosecond time range using laser excitation. In the following paragraph comparisons with conventional thermal methods and LED irradiation are presented.

5.3.1 LED irradiation *vs.* thermal methods

In order to establish if the irradiation of the AuNP plasmon band was required for the catalysis of the resazurin reduction, we performed several experiments using light emitting diodes, microwave oven and thermal bath. In the case of the thermal bath experiments, we analyzed the results obtained placing the sample at two different temperatures, 50 and 80°C. As expected, the system at higher temperature gave the better conversion, confirming that the reaction is temperature controlled. Comparable

results were obtained using a microwave irradiation for 20 min at 80°C. Surprisingly, the LED irradiation, gave a higher conversion compared to the traditional thermal methods used. The fluorescence emission for the experiments obtained after 10 min and employing the different techniques are reported in Figure 5.7.

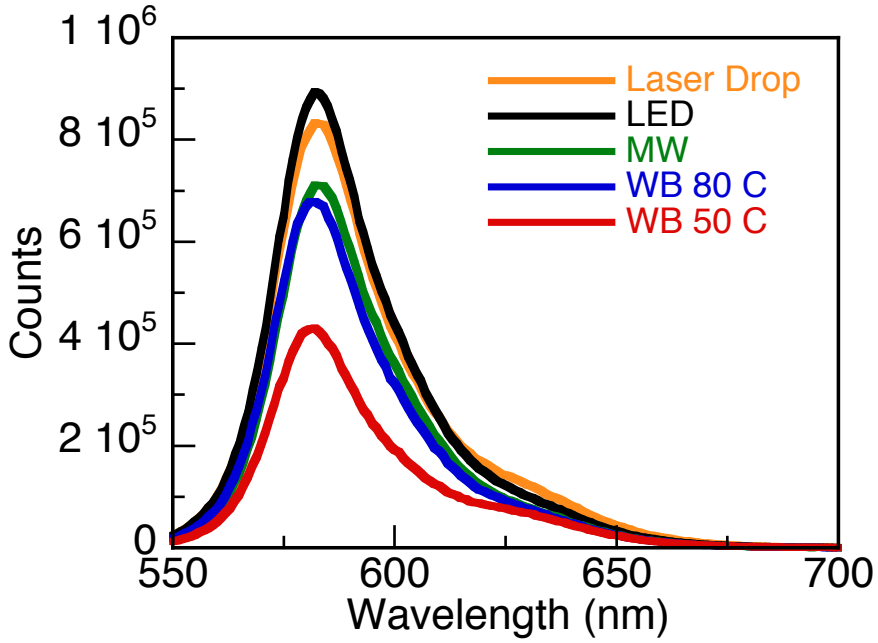

Figure 5.7 Fluorescence emission at a given time (10 min) for the different experiments (except the Laser Drop experiment in which it corresponds to a single ~ 8 ns shot exposure.

Kinetic profiles for the LED and thermal bath experiments showed how the reaction is faster and more efficient using the light emitting diodes even at the lower power. (Figure 5.8) This observation represents an encouraging result for the potential application of the plasmon-mediated catalysis in organic synthesis due also to the convenience of the light source used.

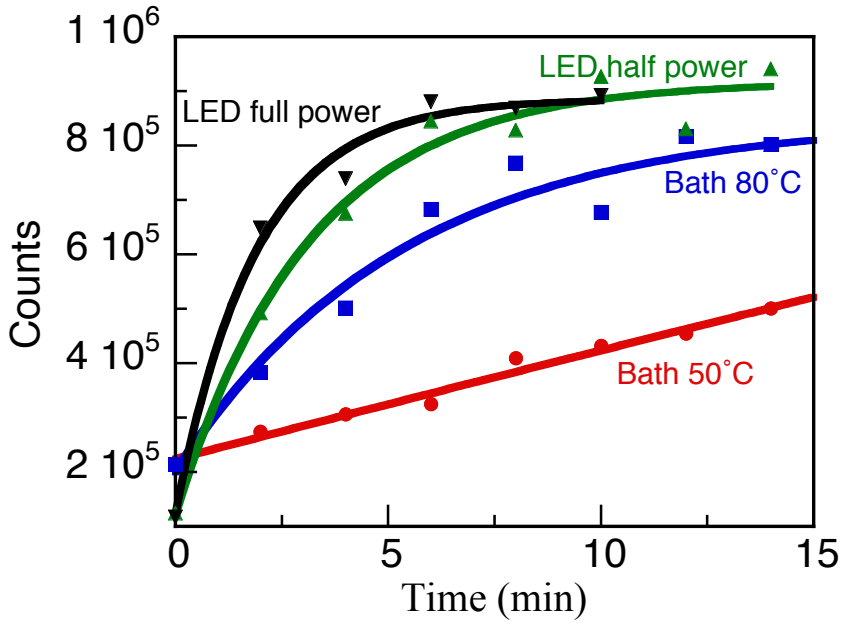

Figure 5.8 Kinetic traces of the experiments in the LED irradiator and the thermal bath. Solutions of resazurin (1 mM), NH_2OH (2 mM) and AuNP (1.4 nM), were submitted to either the LED irradiator or a thermal bath. Samples were taken every 2 min, diluted to 0.1 absorbance and analyzed in a spectrofluorimeter to record its emission spectrum. The experiment was done at two different power settings of the LED irradiator (full nominal power: 4 x 10 W; half nominal power: 4 x 5 W) and at two different temperatures of the thermal bath (80 and 50°C).

5.3.2 Role and concentration effect of NH_2OH as a reducing agent

As mentioned before all the experiments were conducted employing NH_2OH (2 mM) as a reducing agent. In order to have more insights on the role of this amine in the resazurin reduction process few comparative experiments were performed replacing NH_2OH with triethylamine. In this case only a very small fluorescence increase, under the same laser drop exposure conditions, was observed, as reported in Figure 5.9. Therefore, quenching experiments were performed to find out if the lack of emission was due to an emission quenching by the triethylamine or to an actual inefficiency of the latter as a reducing agent for this process. More specifically, the fluorescence of 1 mM resazurin solutions was analyzed, using λ_{ex}= 532 nm, in presence of different concentrations of Et_3N (0.5, 1 and 2 mM) (see Appendix, Figure 5.17). No variation in the emission spectra was

noticed using concentration of Et_3N up to 2 mM, suggesting that this amine does not quench the resorufin fluorescence and confirming that, when used instead of NH_2OH, it does not reduce resazurin to resorufin.

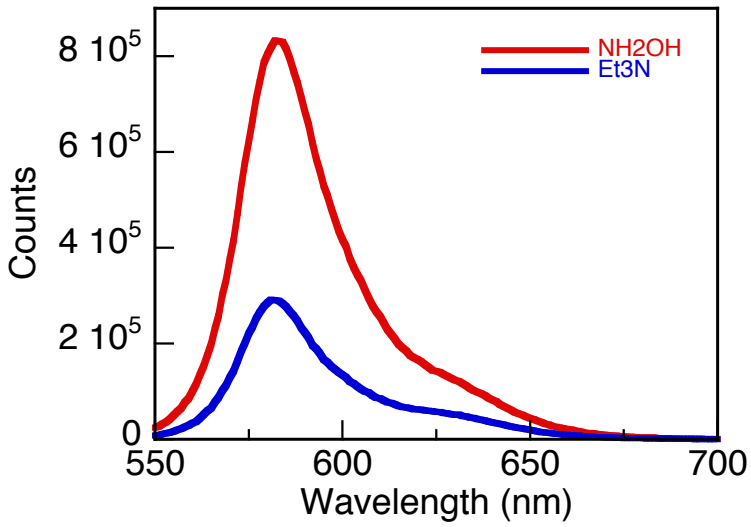

Figure 5.9 Fluorescence spectra from the experiment in the presence of Et_3N and NH_2OH. Laser pulse energy 50 mJ and 1 shot/drop.

These results show as the NH_2OH is a necessary component for the reaction to occur. The different conversions obtained when using the two reducing agents might be due to their distinct affinities for the surface of AuNP and therefore for the catalytic site.

Moreover, we decided to investigate the effect of varying NH_2OH concentration in the reaction mixture. For this purpose, we used the LED irradiation method to have a considerable conversion in a reasonable time (2 min), since the laser drop technique is too fast to provide a kinetic profile. Solutions with different concentrations of NH_2OH ranging from 0.5 to 2 mM, keeping constant the concentration of the other compounds (1 mM of resazurin and 1.4 nM of AuNP) were irradiated and analyzed using the spectrophotometer. In Figure 5.10 is reported the linear dependence of the resorufin emission with the increase of the NH_2OH concentration.

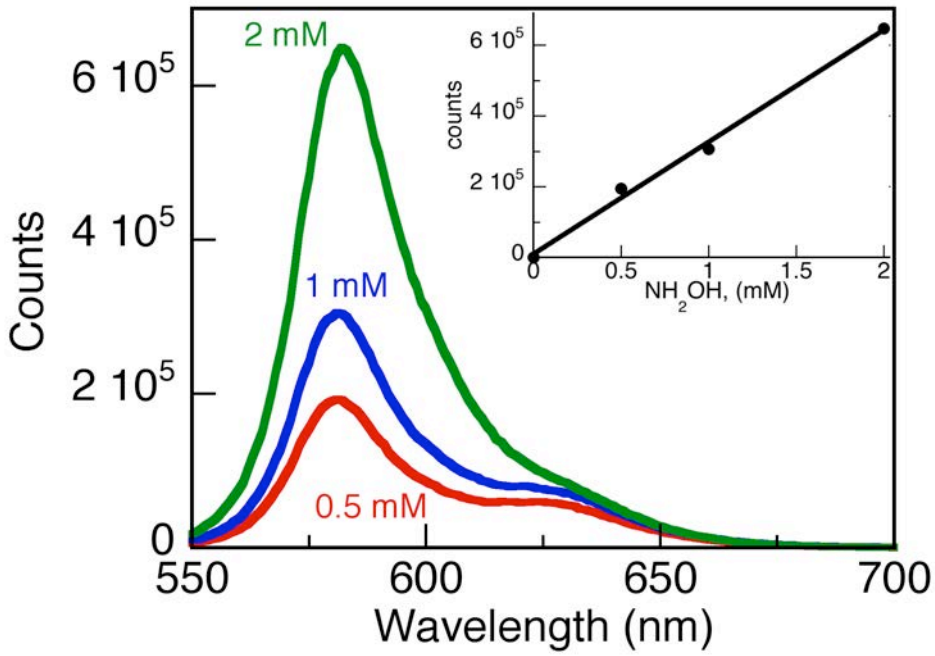

Figure 5.10 Fluorescence intensity of resorufin after LED irradiation of resazurin as a function of hydroxylamine concentration (0.5, 1 and 2 mM) keeping constant the concentration of the other compounds (1 mM of resazurin and 1.4 nM of AuNP); inset: fluorescence intensity vs. NH_2OH concentration (0.5, 1 and 2 mM) after 2 min of irradiation.

Previous publication reported the use of hydroxylamine as a reducing agent, however, its role in the mechanism was not exhaustively examined.[10] With our results we can suggest that the NH_2OH is likely involved in the rate-determining step of the reaction. Therefore the hydroxylamine needs to either reach the resazurin molecule at the reactive site on the AuNP during the brief period of plasmon-induced heating,[1] or assist in the departure of the product (resorufin) following reduction. Chen et al. proposed that product departure occurred either by substitution of fresh resazurin or 'spontaneously';[13] we suggest that the 'spontaneous' product release could be in fact assisted by NH_2OH.

5.4 Stern–Volmer analysis of the fluorescence quenching by AuNP

A dependence study of the resazurin reduction on the AuNP concentration, similar to the one performed for the NH_2OH, was conducted in order to have more mechanistic information on this process. Interestingly, we noticed that with AuNP concentration of 0.7 nM the reaction appears to work better than when using 1.4 nM, since we obtain a stronger fluorescence emission (Figure 5.11). The result obtained can appear unusual, nonetheless, it has been proven that metal nanoparticles can quench the fluorescence of molecules in their vicinity.[14,15]

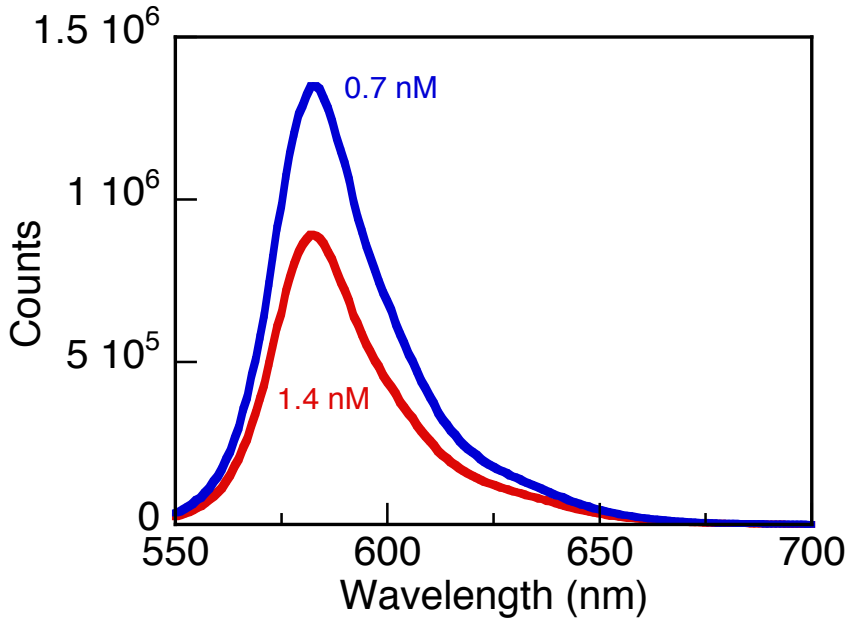

Figure 5.11 Fluorescence intensity of resorufin after LED irradiation of resazurin as a function of AuNP concentration (0.7 and 1.4 nM), keeping constant the concentration of the other compounds (1 mM of resazurin and 2 mM of NH_2OH).

A comprehensive study of the possible resorufin quenching by AuNP was performed, analyzing the emission of the dye at different concentration of particles and employing the Stern-Volmer analysis.[16,17] Figure 5.12 shows the decrease of the resofurin emission

by increasing the AuNP concentration.

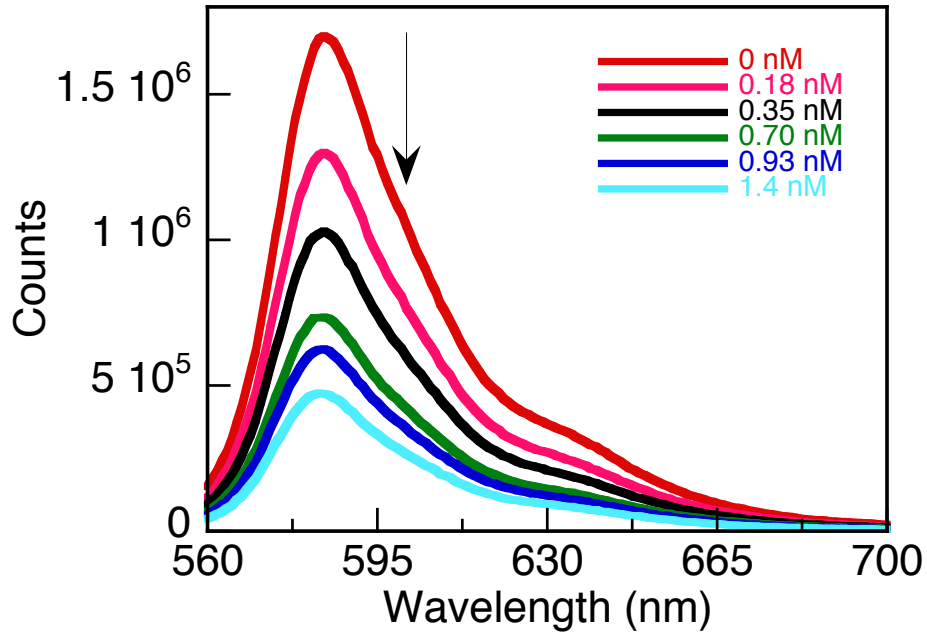

Figure 5.12 Fluorescence emission of resorufin (0.01 mM) with different concentrations of AuNP.

From the spectra obtained we can get a linear Stern-Volmer plot, by reporting the ratio of fluorescence emission in absence (F_0) and in presence (F) of AuNP versus the corresponding AuNP concentration, based on equation 5.1:

$$\frac{F_0}{F} = 1 + K_{SV}[AuNP] \tag{5.1}$$

where K_{SV} is the Stern-Volmer constant. From the slope of the linear Stern–Volmer plot shown in Figure 5.13, we can obtain K_{SV} values of 1.9 x 10^9 and 1.0 x 10^9 L mol^{-1} for excitation at 532 and 560 nm, respectively. The difference between the two values obtained at different excitation wavelength is probably due to some competitive absorption by AuNP at 532 nm and reagent higher absorption when exciting at 560 nm.

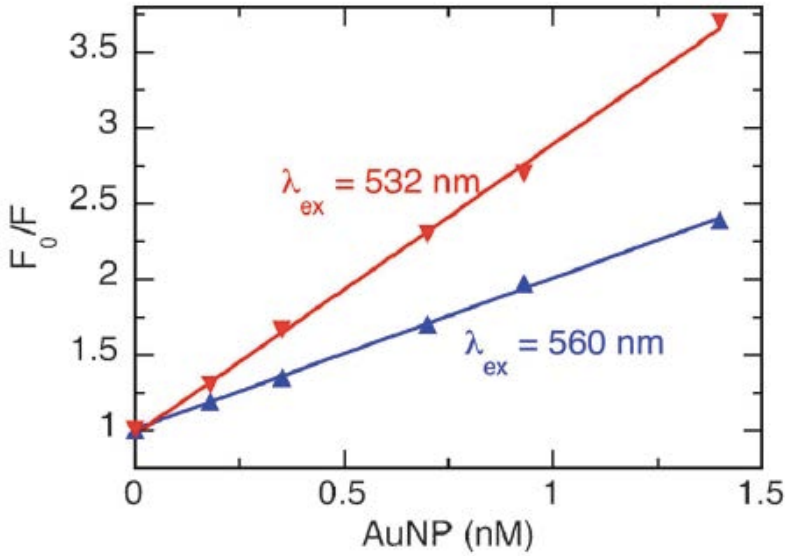

Figure 5.13 Stern–Volmer plots for the quenching of the emission due to the AuNP with excitation at 532 nm (red) and 560 nm (blue).

In the case of dynamic quenching, the Stern-Volmer constant can be expressed as:

$$K_{sv} = k_q \tau \tag{5.2}$$

where k_q is the quenching rate constant and τ the fluorescence lifetime for resorufin (τ= 2.8 ns).[18]

Using the average K_{SV} value, a $k_q \approx 5 \times 10^{17}$ L mol^{-1}s^{-1} can be calculated. This value results to be bigger than the diffusion-controlled rate constant in water ($k_{diff} = 7.4 \times 10^9$ L mol^{-1}s^{-1}),[17] therefore a faster process than the diffusion should be happening. The quenching constant obtained suggests a static quenching occurring between the resorufin and the AuNP, probably due to their pre-association in the ground state. This is a good indication that many excited fluorophores are formed in the vicinity of the nanoparticles. In addition, we can confirm that the dynamic quenching plays a minor role since the resorufin fluorescence lifetime is reduced to 2.6 ns (from an initial 2.8 ns) in the presence of 1.4 nM AuNP.

Moreover, from the fluorescence emission quenching reported in Figure 5.13 it can be estimated that when AuNP concentration of 1.4 nM is employed more than half of the resofurin molecules are bound to the nanoparticle. Therefore, about 3760 molecules

should be associated to each nanoparticle, and since the average AuNP size is 13 nm, an area of ~15 $Å^2$ per dye molecule can be estimated. This value appears to be too small to have the molecules flat on the surface of the AuNP. Most likely the resazurin is associated "head on" on the AuNP surface.

In Table 5.1 are reported fluorescence data at different AuNP and NH_2OH concentrations, obtained either using LED irradiation at 530 nm or a water bath at 80 and 50°C. We calculate the half-lives ($t_{1/2}$) based on the exponential growth analysis of the resorufin fluorescence monitored every 2 minutes for 20 minutes, except for the systems were the plateau level was already achieved.

Table 5.1 Catalytic reduction of 1 mL samples containing 1 mM resazurin exposed to either LED irradiation or a water bath.

Energy source	**[AuNP]/nM**	**[NH_2OH]/mM**	**$t_{1/2}$/ seconds**	**Plateau reached**
LED, 530 nm	0.7	2.0	180	Yes
LED, 530 nm	1.4	2.0	132	Yes
LED, 530 nm	1.4	1.0	186	Yes
LED, 530 nm	1.4	0.5	(700)[a]	No
80 °C water bath	1.4	2.0	225	Yes
50 °C water bath	1.4	2.0	(>1000)[a]	No

(a) Values given in brackets when the fluorescence intensity after 20 minutes was less than 80% of the plateau value, as extrapolated from the exponential growth analysis.

In the fastest case presented (second row), about 500 J mL^{-1} are absorbed to achieve 50% conversion; this value is obtained if we consider four LED at full power, 4 x 4.6 watt, or ~ 18 watt and assume that about 20% is absorbed by the sample. When compared with the laser drop, the LED irradiation appears to be less efficient. Indeed in the case of laser excitation about 10 J mL^{-1} (50 mJ per pulse, ~10 μL drop, estimated 50% light absorption) is enough to achieve over 80% conversion. The higher efficiency of the laser excitation most likely derives from the fact that, during the 8 ns laser pulse, each AuNP absorbs many photons and thus the particle surface temperature can be quite high; this observation can be corroborated considering the findings reported in the previous chapter.[1]

Therefore, we believe that AuNP behave both as a heating element through photoexcitation of their surface plasmon band, as well as a true catalyst, being the

reactive site where the resazurin attached is reduced by the NH_2OH.

When analyzing these results, it is inevitable to consider that the lower conversion obtained with the LED irradiation compared to laser excitation is abundantly compensated by the convenience of the LED source, in terms of cost, installation, maintenance and required technical training.

Recently, mechanistic insights on the deoxygenation of phenoxazine group containing resazurin by hydrazine and catalyzed by platinum nanoparticles have been published.[19] By considering the literature data in addition to our results, we have proposed an initial coordination of the resazurin by the surface of AuNP. The interaction is most probably occurring though the N-oxide group, since this is the only structural difference between reagent and product and the latter does not have a good affinity for AuNP. After the initial coordination, an electron transfer from the AuNP to the resazurin occurs. At this point, NH_2OH assists the dissociation between AuNP and resazurin, providing an electron. This step is identified as the rate determining step of the reaction, due to the conversion dependence on the NH_2OH concentration. The electron transfer is followed by a proton transfer from the reducing agent to the resazurin and finally the release of a molecule of water is obtained as a consequence of a hydrogen atom transfer. Scheme 5.2 summarizes the principal steps of the mechanism proposed.

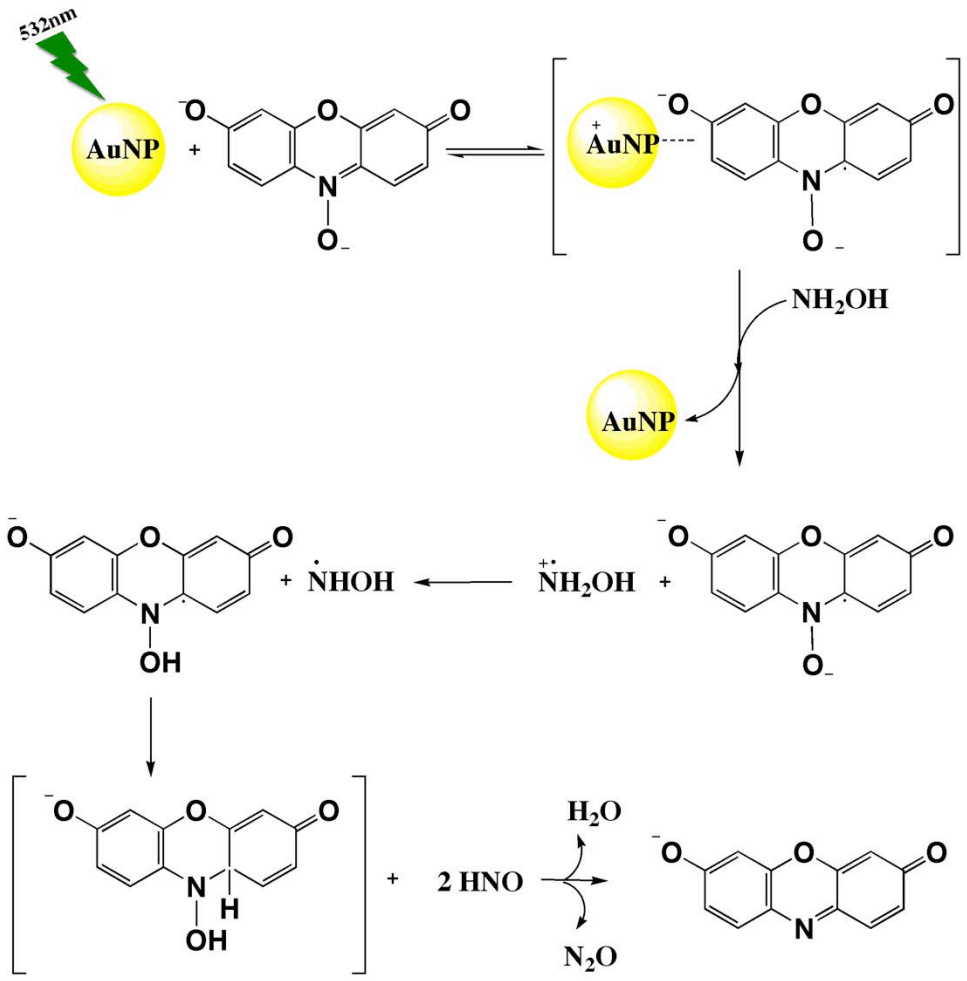

Scheme 5.2 Schematic representation of the proposed resazurin reduction mechanism, using NH_2OH as reducing agent and AuNP as catalyst.

5.5 Summary

In conclusion, we were able to study the resazurin reduction mediated by the plasmon irradiation of spherical AuNP. A comparison between different experimental techniques was provided. Thermal bath and microwave experiment evidenced that the reduction studied is a thermal process; LED and laser drop irradiation were proven to be the most efficient techniques used. The laser drop system furnished the best results in the time range of nanoseconds, corresponding to the duration of a single laser pulse, despite the minutes-long experiments required in the other cases.

However, LED irradiation has been demonstrated to be a competitive source when used for photothermal processes, being inexpensive, easy to use and relatively fast.

A better understanding of the resazurin reduction process was possible by the concentration dependence studies performed for both NH_2OH, the reducing agent, and for AuNP. Finally mechanistic insights were obtained from the fluorescence quenching study, from which a static quenching between the resazurin and the AuNP was derived.

This project represents a successful application of AuNP plasmon excitation in the catalysis of thermal processes and the first example in the Scaiano group of reduction processes catalyzed by AuNP.

5.6 Appendix

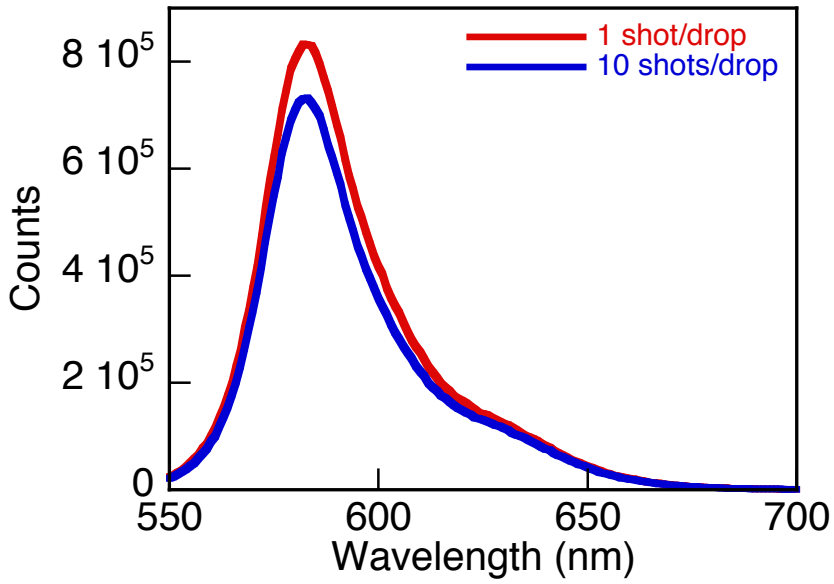

Figure 5.14 Fluorescence spectra from the experiments obtained with different shots/drop and constant laser pulse energy (50 mJ).

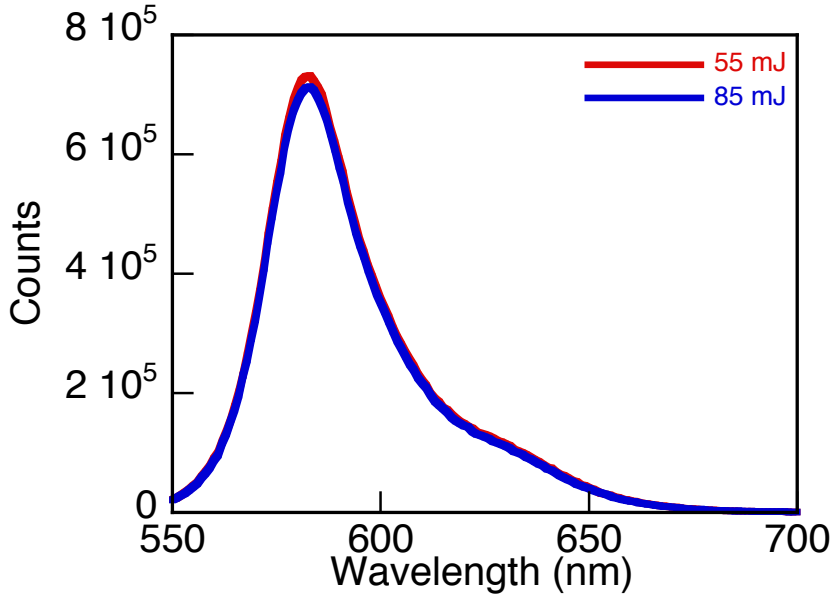

Figure 5.15 Fluorescence spectra from the experiments obtained with different laser pulse energies and constant number of laser pulse per drop (1 shot/drop).

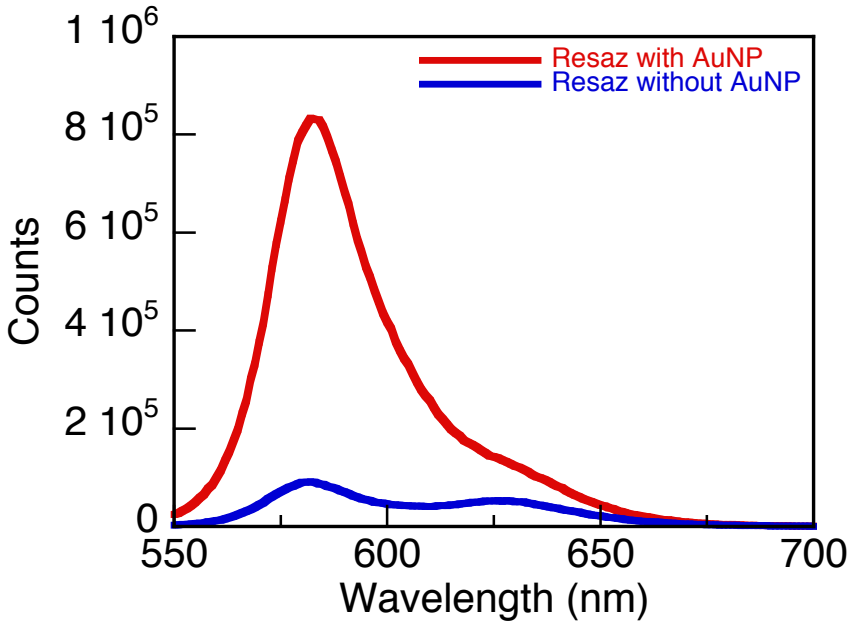

Figure 5.16 Fluorescence spectra from the experiments obtained in the presence and absence of AuNP, using laser pulse energy of 50 mJ and 1 shot/drop.

Figure 5.17 shows the quenching experiment performed using different concentrations of Et_3N (0.5, 1 and 2 mM) into the 1mM resorufin solution at λ=532 nm, confirming that at the concentrations used the lack of fluorescence enhancement is not due to the amine quenching.

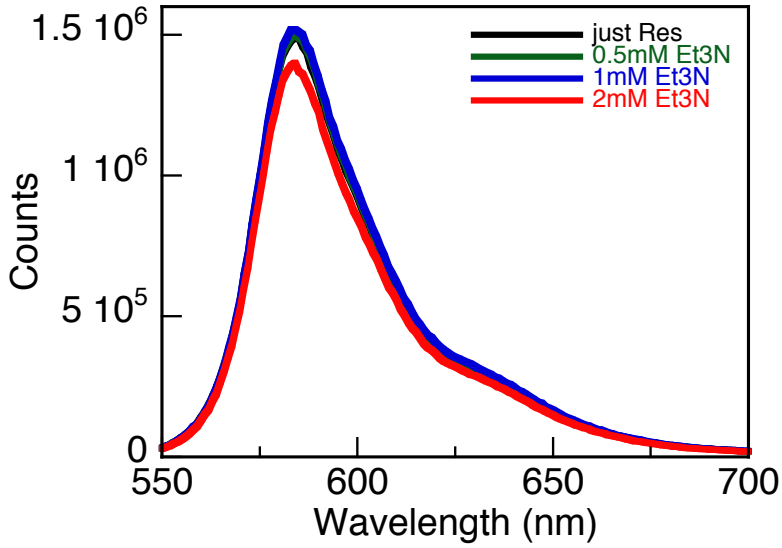

Figure 5.17 Resorufin (1mM) fluorescence with different concentrations of Et_3N in water, λ_{ex} = 532 nm.

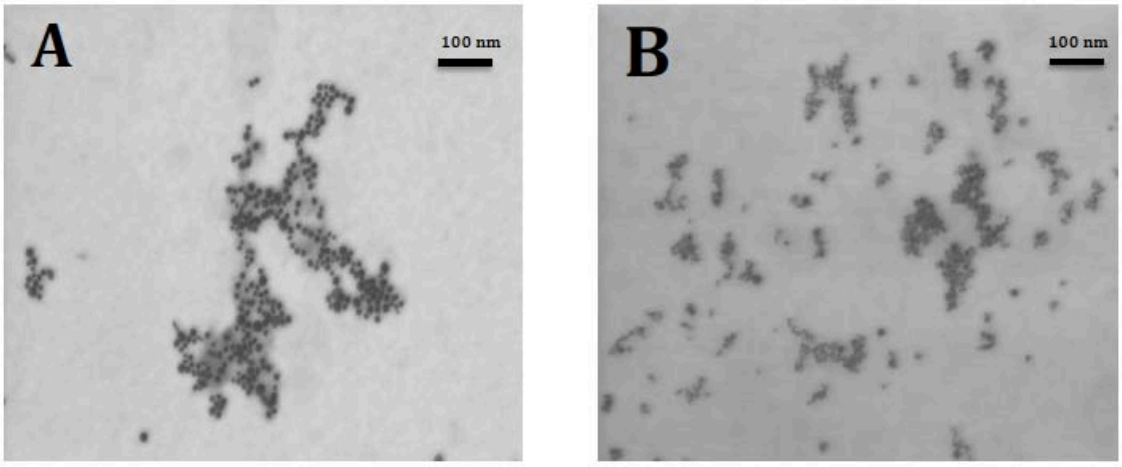

Figure 5.18 SEM pictures of AuNP before (A) and after (B) laser drop irradiation (1 s/d).

5.7 References

(1) Fasciani, C.; Bueno-Alejo, C. J.; Grenier, M.; Netto-Ferreira, J. C.; Scaiano, J. C. High-Temperature Organic Reactions at Room Temperature Using Plasmon Excitation: Decomposition of Dicumyl Peroxide. *Organic Letters,* **2011**, 13, 204.

(2) Hallett-Tapley, G. L.; Silvero, M. J.; Gonzalez-Bejar, M.; Grenier, M.; Netto-Ferreira, J. C.; Scaiano, J. C. Plasmon Mediated-Catalytic Oxidation of sec-Phenethyl and Benzyl Alcohols. *Journal of Physical Chemistry C*, **2011**, 115, 10784.

(3) O'Brien, J.; Wilson, I.; Orton, T.; Pognan, F. Investigation of the Alamar Blue (Resazurin) Fluorescent Dye for the Assessment of Mammalian Cell Cytotoxicity. *European Journal of Biochemistry*, **2000**, 267, 5421.

(4) (a) Candeias, L. P.; MacFarlane, D. P. S.; McWhinnie, S. L. W.; Maidwell, N. L.; Roeschlau, C. A.; Sammes, P. G.; Whittlesey, R. The Catalysed NADH Reduction of Resazurin to Resorufin. *Journal of the Chemical Society, Perkin Transactions 2***, 1998**, 2333. (b) Taneja, N. K.; Tyagi, J. S. Resazurin Reduction Assays for Screening of Anti-Tubercular Compounds against Dormant and Actively Growing Mycobacterium Tuberculosis, Mycobacterium Bovis BCG and Mycobacterium Smegmatis. *Journal of Antimicrobial Chemotherapy,* **2007**, 60, 288.

(5) Talbot, J. D.; Barrett, J. N.; Barrett, E. F.; David, G. Rapid, Stimulation-Induced Reduction of C12-Resorufin in Motor Nerve Terminals: Linkage to Mitochondrial Metabolism. *Journal of Neurochemistry,* **2008**, 105, 807.

(6) Porcal, G. V.; Previtali, C. M.; Bertolotti, S. G. Photophysics of the Phenoxazine Dyes Resazurin and Resorufin in Direct and Reverse Micelles. *Dyes and Pigments,* **2009**, 80, 206.

(7) (a) Twigg, R. S. Oxidation-Reduction Aspects of Resazurin. *Nature*, **1945**, 155, 401; (b) Xu, W.; Shen, H.; Kim, Y. J.; Zhou, X.; Liu, G.; Park, J.; Chen, P. Single-Molecule Electrocatalysis by Single-Walled Carbon Nanotubes. *Nano Letters,* **2009**, 9, 3968.

(8) Bueno, C.; Villegas, M. L.; Bertolotti, S. G.; Previtali, C. M.; Neumann M. G.; Encinas, M. V. The Excited-State Interaction of Resazurin and Resorufin with Aminesin Aqueous Solutions. Photophysics and Photochemical Reaction. *Photochemistry and Photobiol*ogy, **2002**, 76, 385.

(9) (a) Zhou, X.; Xu, W.; Liu, G.; Panda, D.; Chen, P. Size-Dependent Catalytic Activity and Dynamics of Gold Nanoparticles at the Single-Molecule Level. *Journal of American Chemical Society,* **2009**, 132, 138; (b) Chen, P.; Xu, W.; Zhou, X.; Panda D.; Kalininskiy, A. Single-Nanoparticle Catalysis at Single-Turnover Resolution. *Chemical Physics Letters,* **2009**, 470, 151.

(10) Xu, W.; Kong, J. S.; Chen, P. Probing the Catalytic Activity and Heterogeneity of Au-Nanoparticles at the Single Molecule Level. *Physical Chemistry Chemical Physics*, **2009**, 11, 2767.

(11) (a) Banks, J. T.; Scaiano, J. C. The Laser-Drop Method: A New Approach To Induce Multiple Photon Chemistry with Pulsed Lasers. Examples Involving Reactions of Diphenylmethyl and Cumyloxyl Radicals. *Journal of American Chemical Society*, **1993**, 115, 6409; (b) Scaiano; J. C.; Banks, J. T. The Laser-Drop Technique: A Semipreparative Method for the Study of Multiphotonic Processes. *Journal of the Brazilian Chemical Society,* **1995**, 6, 211.

(12) (a) Marin, M. L.; McGilvray, K. L.; Scaiano, J. C. Photochemical Strategies for the Synthesis of Gold Nanoparticles from Au(III) and Au(I) Using Photoinduced Free Radical Generation. *Journal of American Chemical Society*, **2008**, 130, 16572; (b) McGilvray, K. L.; Decan, M. R.; Wang, D.; Scaiano, J. C. Facile Photochemical Synthesis of Unprotected Aqueous Gold Nanoparticles. *Journal of American Chemical Society*, **2006**, 128, 15980.

(13) Xu, W.; Kong, J. S.;. Yeh, Y.-T. E; Chen, P. Single-Molecule Nanocatalysis Reveals Heterogeneous Reaction Pathways and Catalytic Dynamics. *Nature Materials*, **2008**, 7, 992.

(14) Pacioni, N. L.; Gonzalez-Bejar, M.; Alarcon, E.; McGilvray, K. L.; Scaiano, J. C. Surface Plasmons Control the Dynamics of Excited Triplet States in the Presence of Gold Nanoparticles. *Journal of American Chemical Society,* **2010**, 132, 6298.

(15) (a) Ao, L.; Gao, F.; Pan, B.; He, R.; Cui, D. Fluoroimmunoassay for Antigen Based on Fluorescence Quenching Signal of Gold Nanoparticles. *Analytical Chemistry,* **2006**, 78, 1104; (b) Anger, P.; Bharadwaj, P.; Novotny, L. Enhancement and Quenching of Single-Molecule Fluorescence. *Physical Review Letters,* **2006**, 96, 113002.

(16) Lakowicz, J. R. Principles of Fluorescence Spectroscopy. *Kluwer Academic-Plenum Publishers*, New York, **1999**.

(17) Turro, N. J.; Ramamurthy V.; Scaiano, J. C. Modern Molecular Photochemistry of Organic Molecules. *University Science Publishers*, New York, NY, **2010**.

(18) Montejano, H. A.; Gervaldo, M.; Bertolotti, S. G. The Excited-States Quenching of Resazurin and Resorufin by p-Benzoquinones in Polar Solvents. *Dyes and Pigments*, **2005**, 64, 117.

(19) Das, R. S.; Singh, B.; Banerjee, R.; Mukhopadhyay, S. PVP stabilized PVP stabilized Pt nano particles catalyzed de-oxygenation of phenoxazine group by

hydrazine in physiological buffer media: surfactant competes with reactants for the same surface sites. *Dalton Transactions,* **2013**, 42, 4068.

Chapter 6

Plasmon Assisted Photolithography

6.1 Introduction

Photolithography, usually denoted as lithography, is a process commonly employed in the fabrication of integrated chips or thin film in general. The technique was invented in 1826 and since then gigantic steps have been made in improving its performance and applications. A simple idea can be given by the fact that most of the electronic devices, we use daily, such as computers or cell phones, store information on components made using a photolithography technique.[1] As the name suggests, photolithography uses light to create features on a specific substrate, described as a solubility switch. Usually the substrate is coated with a polymer that presents a different solubility before and after irradiation. By using a mask it is possible to expose some areas of the polymer to the light, while other portions remain covered. After the irradiation, the film is washed with the required solvent and, according to the nature of the polymer, the exposed or the unexposed portions are dissolved to give rise to the desired feature on the film. If the irradiated part of the film is removed we have a positive image, on the other hand, a

negative image is obtained when the unexposed portions of the polymer are dissolved by the solvent (Figure 6.1).[2]

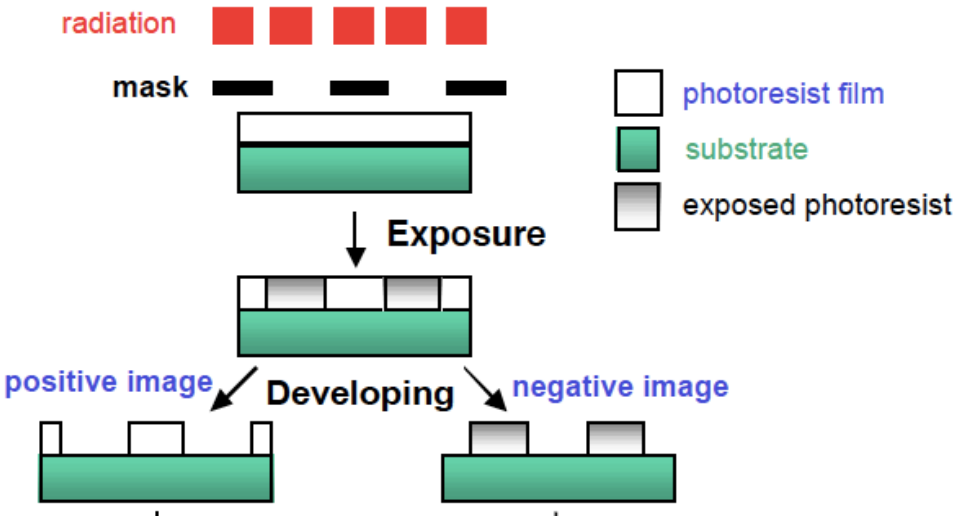

Figure 6.1 Schematic representations of the typical steps for the formation of photolithographic images.

The use of light makes this technique very versatile, however, it leads to considerable limitations, the most important being the diffraction limit. Diffraction limit appears to be limiting especially when dealing with the size and the number of features that can be put on a chip. This fundamental limitation can be mathematically expressed as:

$$D = \lambda / 2(n \sin \theta) \qquad (6.1)$$

where D represents the resolution reachable, λ is the wavelength used, n is the refractive index of the medium and θ is the incident angle. The value $(n \sin \theta)$ is also called numerical aperture. Modern technology uses light wavelength of 193 nm since, wavelengths lower than that would be absorbed by the molecules used in the polymer and therefore, undesired chemical reactions would occur. For this wavelength features with a minimum size of 96 nm would be obtained ($\sim \lambda/2$). Improvements in the optics can let us achieve features with a resolution equal to $\lambda/3 = 63$ nm. To further decrease

this value a double exposure procedure can be performed. In this case, the film is irradiated twice using a mask that is shifted after each irradiation, and employing a chemical process where only the areas that have been irradiated in both steps will give a change in solubility either negatively or positively. In this way it is possible to reduce by a half the value of the resolved feature, reaching 32 nm. The last attempt in overcoming this limit was done by using a non-linear process, such as a two photons technology. The features obtained in such a way are 22 nm in size. Attempt to reach smaller features are still in progress but not many more "tricks" can be used to overcome the diffraction limit,[3] unless we employ a non-diffraction limited process. In 1965, with a pioneering observation, Gordon Moore, one of the founders of Intel, predicted that the number of features stored in the integrated chips would double every two years (Figure 6.2).[4] This prediction is now known as "Moore's law" and it has been the driving force for the computer technology development. However, new ideas are required to overpass the limitation encountered using the conventional photolithography technique.

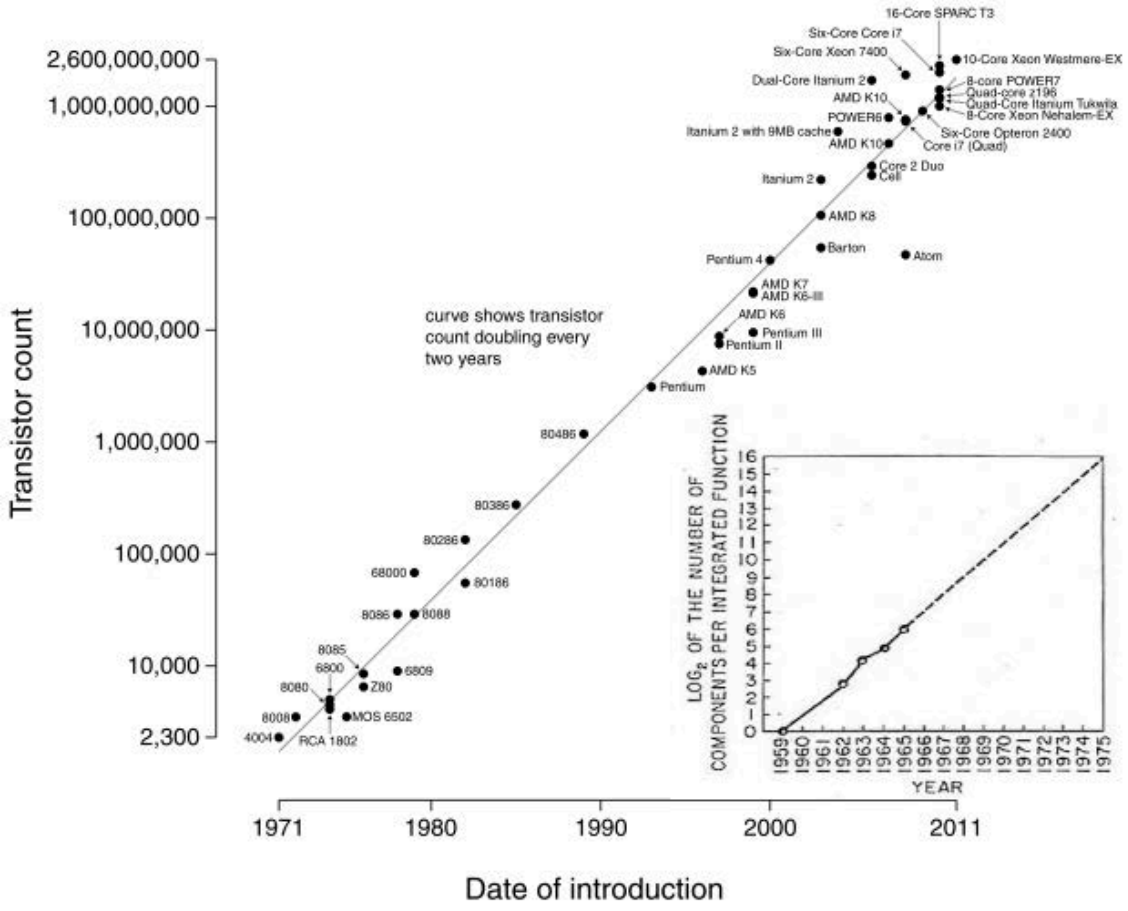

Figure 6.2 Microprocessor transistors counts from 1971 to 2011 and Moore's law (strait line). The curve shows transistor count doubling every two years. (Insert) Original Moore's prediction, in 1965, extrapolated to 1975. [Image obtained adapting the plot of transistors count vs. year, taken from http://en.wikipedia.org/wiki/Moore's_law, with the original Moore's plot from reference 4].

For this purpose, the use of plasmon assisted processes, in which the nanoparticles determine where features will be created, appears to be promising as an emerging photolithography approach.[5,6] Kevin Stamplecoskie, a previous member of the Scaiano's group, explored first this field by taking advantage of the electromagnetic field enhancement around AgNP to start a radical polymerization, using azobisisobutyronitrile (AIBN) as a free radical initiator and a triacrylate. After plasmon excitation, the triacrylate would cross-link around the AgNP creating insoluble features (Figure 6.3).[5]

This contribution represents an encouraging result, however no spatial control is achievable by adopting this procedure.

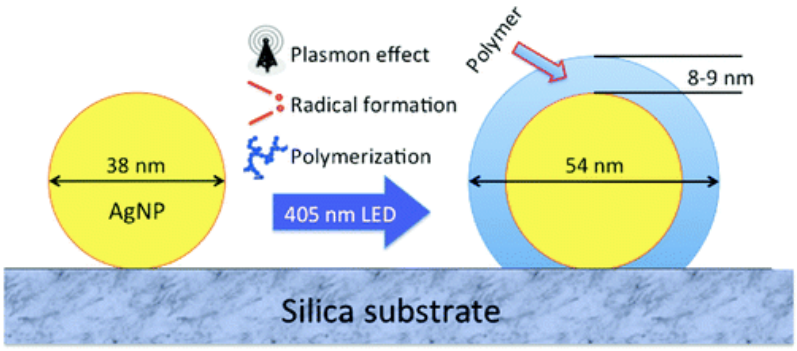

Figure 6.3 Cartoon representation of the plasmon-mediated radical photopolymerization. AgNP were synthesized and then spin-coated, in addition to triacrylate and AIBN, on a silica substrate. The electromagnetic enhancement around the AgNP makes the radial polymerization happening, creating lithographic features. No control in the spatial distribution of the particles is achieved. [Figure reproduced from ref. 5].

In order to overcome this limitation, we decided to replace the radical polymerization with a thermal one. Our intent was to synthesize AgNP *in situ*, meaning directly on the substrate, instead of randomly spin-coat them on the substrate. Since the reduction of Ag^{+} to AgNP, mediated by I-2959 is a radical process, it may interfere with a radical polymerization, as the one employed by Kevin, therefore we decided to replace it with a thermal polymerization. For this purpose, a two steps irradiation method was used, where in the first step the AgNP would be formed, followed by a second step in which the plasmon irradiation would induce the thermal polymerization. To prove our concept we decided to employ the formation of nylon-6 from caprolactam (Scheme 6.1), a process that requires temperatures above 100°C.[7,8]

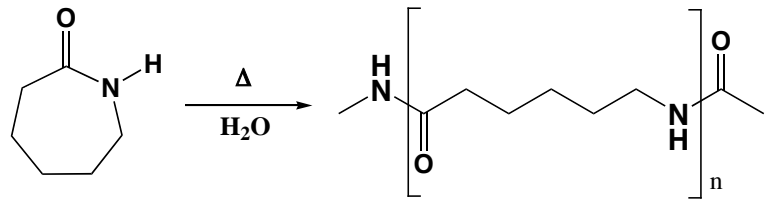

Caprolactam **Nylon-6**

Scheme 6.1 Nylon-6 formation by thermal polymerization of caprolactam.

As reported in Chapter 4, irradiation of spherical AuNP led to temperatures close to 500°C.[9] For the thermal polymerization reported above, we employed AgNP, which present a higher excitation coefficient and a more energetic plasmon band (400 nm) compared to AuNP (530 nm).[10] Therefore, a higher surface temperature should be reached when irradiating AgNP. Once the polymerization of caprolactam is completed locally around the spherical AgNP, the differences in solubility between caprolactam and nylon-6 result in localized sub-wavelength features, after washing treatments. In our method, UVA light is used to synthesize AgNP, on specific positions of a quartz disk, by using a mask. The entire disk was then irradiated using 405 nm LED, corresponding to the plasmon absorption wavelength of the AgNP formed. The irradiation of AgNP results in a localize heat release, responsible for the thermal polymerization around the particles. The schematic representation of the procedure used is reported in Figure 6.4. Adopting this methodology, the limitations due to the diffraction limit can be overcome by employing a non-diffraction limited process.

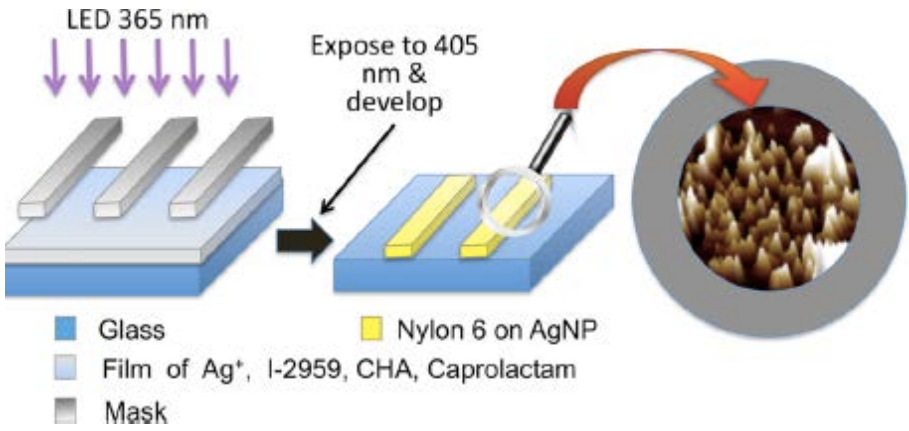

Figure 6.4 Cartoon of the dual-stage photolithography method. In the first step, a glass slide, functionalized with AgNP precursors and caprolactam, is irradiated using a 365 nm LED and employing a mask. At this point, AgNP will be selectively formed only on the irradiated portions of the slide. The following step consists in the excitation of the SPR of AgNP just formed, using a 405 nm LED. This second irradiation will induce the polymerization of caprolactam to nylon-6 only around the AgNP and therefore, ordered features will be created. [Figure reproduced from ref. 11]

6.2 Materials and Methods

6.2.1 Materials

$AgCF_3COO$, caprolactam, cyclohexylamine (CHA), poly(methyl methacrylate) (PMMA) cyclohexanone and cumarine-6 were purchased from Sigma-Aldrich and used without further purification. PMMA was used to make more homogeneous films and it is removed after the synthesis by washing. I-2959 was obtained as generous gift form BASF supplied by Dempsey Corporation Canada.

6.2.2 Precursor solution and spin coating

50 μL of a solution containing equal amounts of $AgCF_3COO$, I-2959 and cyclohexylamine at 1-2 wt%, 2 wt% PMMA, 15 wt% caprolactam and 75 wt% cylohexanone as a solvent were spin coated at 2500 rpm onto one-inch diameter quartz disks. 2 % PMMA was added to improve the adhesion of the film. The film thicknesses obtained were measured to be 991± 31 nm for several spin coated films.

6.2.3 LED irradiation

A lithographic mask was put in direct contact with the spin coated films, as shown in Figure 6.5. Subsequently, a double step irradiation was performed using a typical 365 nm LED irradiator for 30 min, followed by 405 nm LED irradiation for additional 30 min and finally, the disks were washed with ethanol. The setup used for both irradiation steps is reported in Figure 6.5, the only variable was the actual wavelength used. LED powers were 500 mW and 460 mW for the 365 and 405 nm LED respectively.

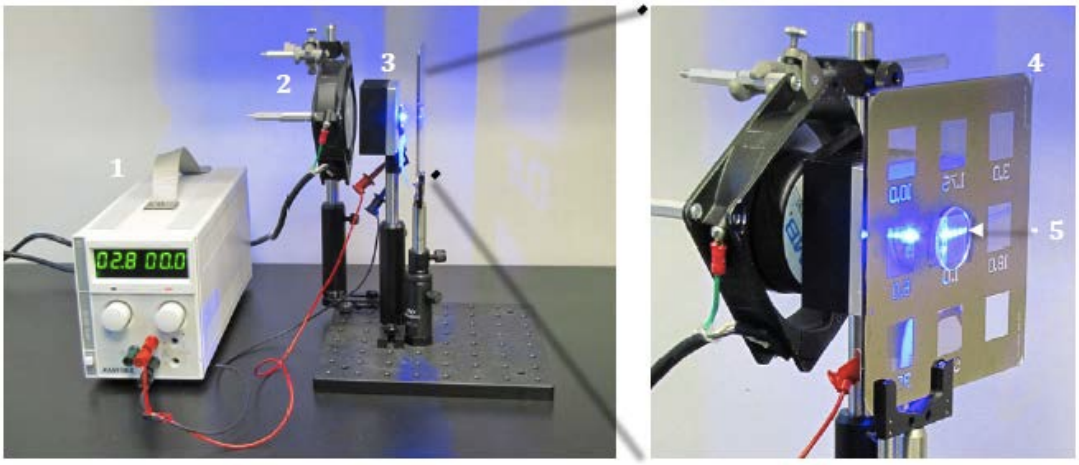

Figure 6.5 Experimental setup for irradiation of spin-coated films. 1 = power supply, 2 = cooling fan, 3 = light emitting diode mounted on an Aluminum plate and heat sink, 4=lithographic mask, and 5 = quartz disk with spin-coated film.

6.2.4 Film analysis

The analysis of the films obtained was performed using AFM, UV-vis spectroscopy, FLIM and electron microscopy. Specifications of the instruments are reported in Chapter 2, nonetheless specific conditions of the experiments are illustrated below.

AFM was performed under air on various areas of the irradiated films, working in non-contact mode. AFM probes had a resonance frequency of 150 kHz and a force constant of 5 N/m.

UV-Vis spectra of the spin-coated films were acquired at each step of the polymerization

and washing process with a CARY 50 UV-Vis spectrophotometer.

FLIM images were obtained employing a 375 nm diode laser, monitoring the emission at $\lambda > 405$ nm by using a 405 nm long pass filter.

SEM images of the AgNP with nylon-6 shells were taken using a STEM detector. COMPO mode was also used to identify the metal component from the organic material.

6.3 Hierarchical approach to subwavelength features

As mentioned in the introduction, the procedure is based on a double-step process to (1) synthesize AgNP in defined position, using a radical process, (2) use a thermal polymerization process to form insoluble nylon-6 around the particles.[11]

6.3.1 Double-stage irradiation

In the first step, AgNP were synthesized using a procedure commonly employed in our laboratory.[12,13] In this process a 365 nm LED is used to irradiate for 30 min the quartz disk attached to a lithographic mask, after spin coating of the precursor solution. The light used is able to generate ketyl radicals from I-2959 and thus, the radical formed will induce the reduction of Ag^+ to Ag^0. As mentioned in the previous chapters, this process is a proton coupled electron transfer, see Scheme 6.2, where the presence of CHA favors the nanoparticles formation by trapping the proton released.[12]

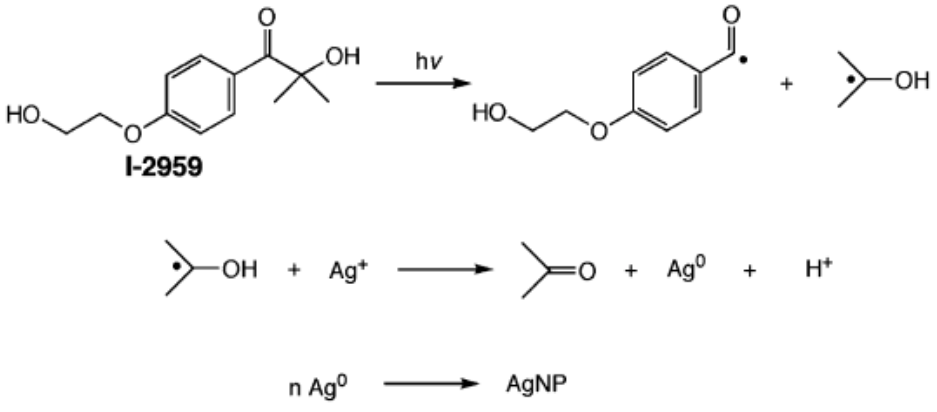

Scheme 6.2 Synthesis of AgNP using I-2959.

Using a 3 μm mask, we were able to generate compact AgNP lines on the quartz disk, as observed using microscope imaging (Figure 6.6).

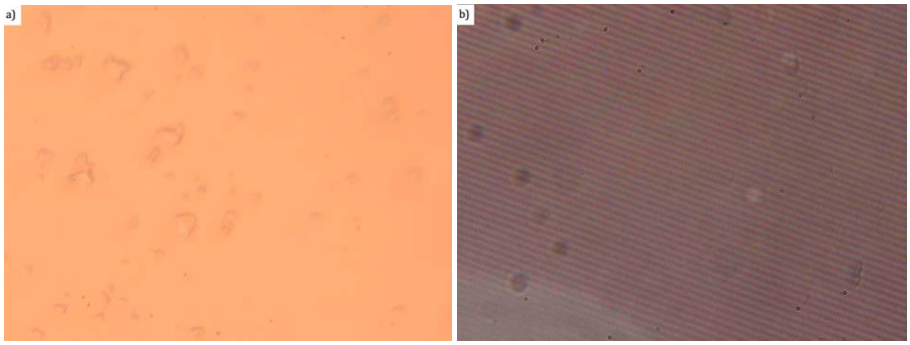

Figure 6.6 Microscope images of the film (a) before and (b) after irradiation with 365 nm LED.

The microscope images clearly show the presence of a pattern after 365 nm LED irradiation. In addition, UV-vis spectra recorded before and after irradiation confirmed the presence of an intense plasmon absorption in correspondence of the AgNP plasmon band above 400 nm (Figure 6.7).[14] The spectrum obtained presents a broad absorption probably due to the absorption of AgNP in close proximity, which lead to a shift of the usual silver plasmon absorption to longer wavelengths.[15-17]

After the AgNP synthesis, the 365 nm LED was replaced by a 405 nm LED in order to irradiate the plasmon absorption band and therefore induce a local temperature increase able to polymerize the caprolactam. UV-vis spectra were collected before each irradiation step as shown in Figure 6.7. As mentioned before, the first irradiation (using 365 nm LED) led to the appearance of a band around 400 nm, confirming the formation of AgNP. The following irradiation (using a 405 nm LED) led to a mild shift of the plasmon band, probably due to the change of the refractive index of the medium around the particles, confirming therefore the caprolactam polymerization. The intensity of the plasmon remains constant, meaning that no silver salt was left for reduction.

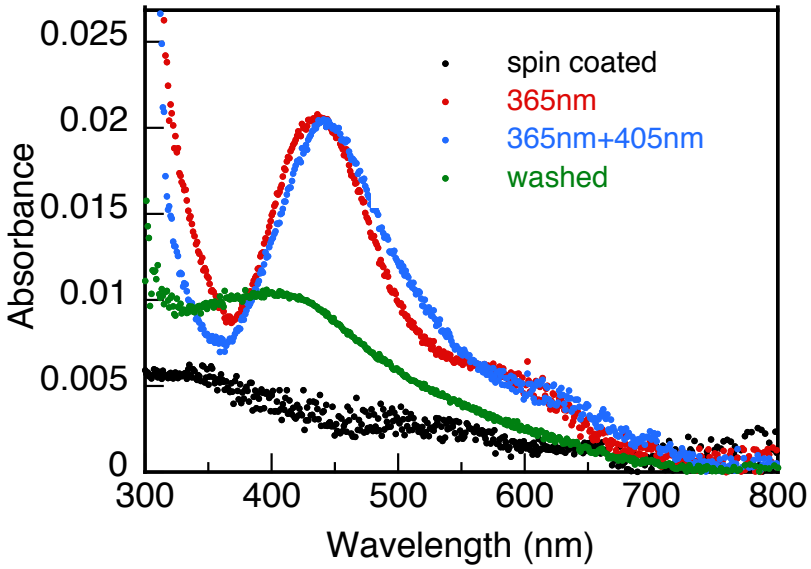

Figure 6.7 UV-vis absorption spectra of the film during the different steps: (black) after spin coating, (red) after the first irradiation step with 365 nm LED, (blue) after the second irradiation step at 405 nm, and (green) after final washing with water to remove the insoluble caprolactam.

As a comparison, the two steps of irradiation were inverted, in such a way that the spin-coated solution was first irradiated with a 405 nm LED, followed by a 365 nm irradiation. The resulting UV-spectra obtained after each step are reported in Figure 6.8. After the first irradiation at 405 nm for 30 s no AgNP were synthesized. Indeed, the surface plasmon band appears just after the second irradiation at 365 nm for 30 s. The inversion of wavelength irradiation does not induce the polymerization of caprolactam. As a result, the AgNP are not trapped by nylon-6 and thus, the disappearance of the plasmon band is observed after the final washing step.

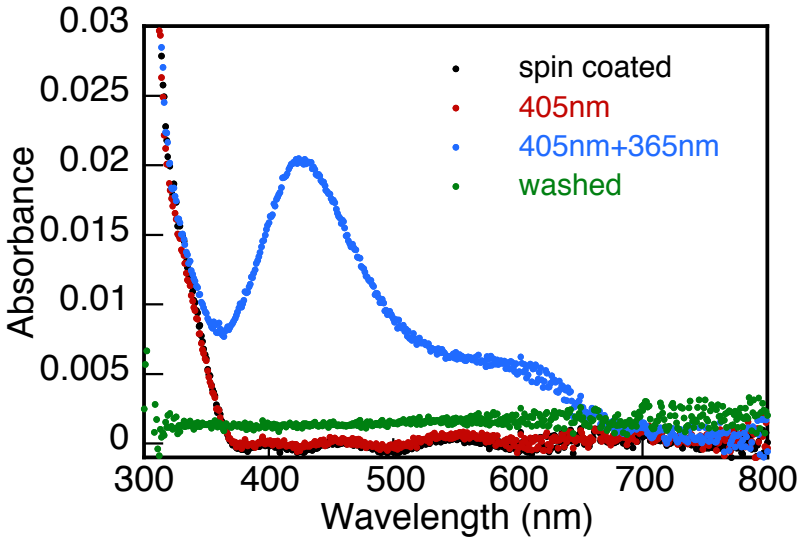

Figure 6.8 UV-vis absorption spectra of the film, inverting the wavelengths order: (black) after spin coating, (blue) after irradiation at 405 nm as first step, (red) after the second irradiation step using 365 nm LED, and (pink) after final washing.

A comparison of the absorbance at 425 nm, recorded in the two different sets of experiments, is reported in Figure 6.9.

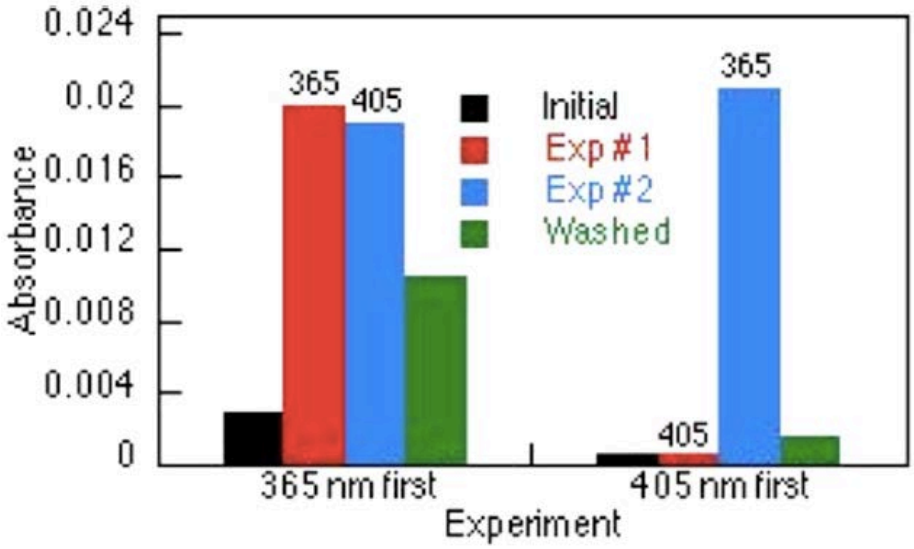

Figure 6.9 Absorbance at 425 nm recorded after each step, for the two different orders of irradiation: Exp.1= 365 nm followed by 405 nm irradiation; Exp.2= 405 nm followed by 365 nm irradiation.

With these experiments we were able to prove that the polymerization of caprolactam is actually occurring locally around the AgNP, when they are previously synthesized and then excited. Indeed, just when this order of irradiation is performed, nylon-6 is thermally formed, thanks to the high temperatures reached exciting the plasmon, and therefore, it is able to fix the particles on the disk.

Finally, the un-reacted caprolactam was removed by washing the film with water, while the insoluble nylon-6 remained on the film encapsulating the AgNP. AFM images were taken to gain more insight regarding this polymerization process and the pattern formed. Figure 6.10 shows the presence of a well-organized distribution of nylon–coated particles in correspondence of the light exposed positions, in contrast with the flat unexposed portions of the disk. With this procedure, AgNP form lines of 3 μm, which are then fixed by the formation of the water insoluble polymer around the nanoparticles. The cross-section graph (Figure 6.10, b) shows the height of the features formed, underlining the presence of single and multiple particles within the irradiated 3 μm line. From the 3-dimension image we can clearly distinguish the two levels formed on the

disk, corresponding to the portions where AgNP are encapsulated inside nylon-6 and the unexposed portions free from any debris.

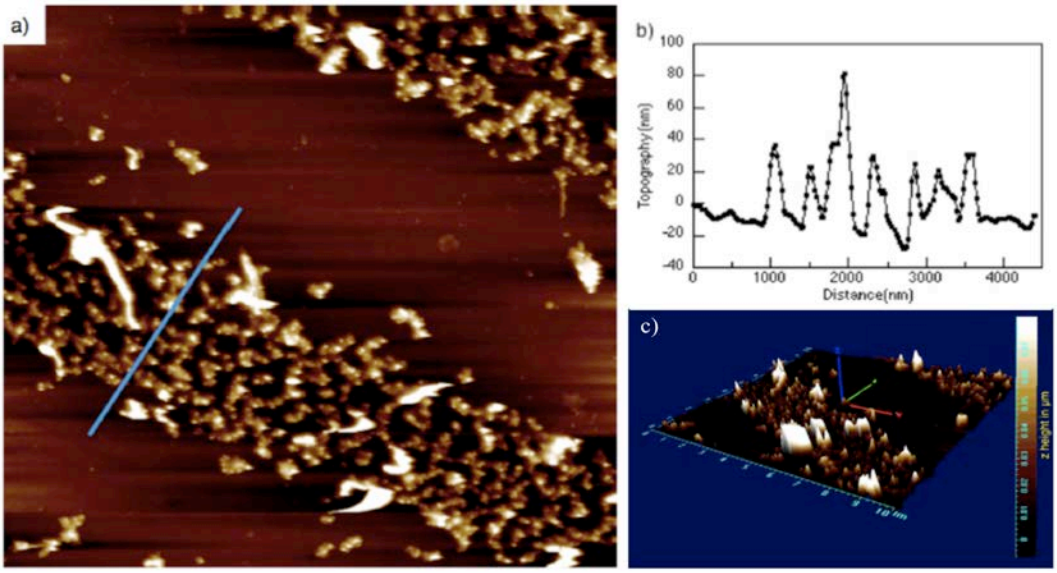

Figure 6.10 (a) AFM image of the film obtained after a complete dual stage lithography process. (b) Cross section of the height of features located in correspondence of the line shown in image (a). (c) 3-D image of the same region reported in image (a).

The analysis of the images gave an indication of the smallest features obtained, corresponding to a single AgNP coated by nylon-6 polymer and measuring 25 nm. This value is significantly smaller then the diffraction limit for the visible light used. From a statistic calculation, obtained analyzing 99 particles from several pictures, the average height of the particles measures 44 ± 13 nm. Even though these measurements show a wide polydispersity of the particles and therefore an uneven distribution of the localized heat released by the AgNP, we have proven that a non-diffraction limited photolithography procedure can be obtained by using plasmon irradiation of AgNP.

To further investigate the structures of the polymer-nanoparticles system, SEM images of a colloidal solution were taken. For this analysis, a nylon-6-AgNP composite in solution was prepared, irradiating in two steps (5 min with 365 nm and then 5 more min

with 405 nm LED) a mixture containing the same precursors employed for the film formation on the quartz disk. From the pictures obtained we can clearly identify AgNP, with an average size smaller than 20 nm (Figure 6.11). Interestingly, all darker spots, corresponding to the AgNP, are surrounded by a lighter shell, which is attributed to the organic polymer layer. This observation is confirmed by the COMPO mode images. In this configuration, materials interacting strongly with the electron beam, such as AgNP, appear brighter then materials with a lower electron density, such as the surrounding coating of nylon-6. The images obtained highlight how the thermal polymerization happens locally around the particles and underline the absence of un-functionalized AgNP.

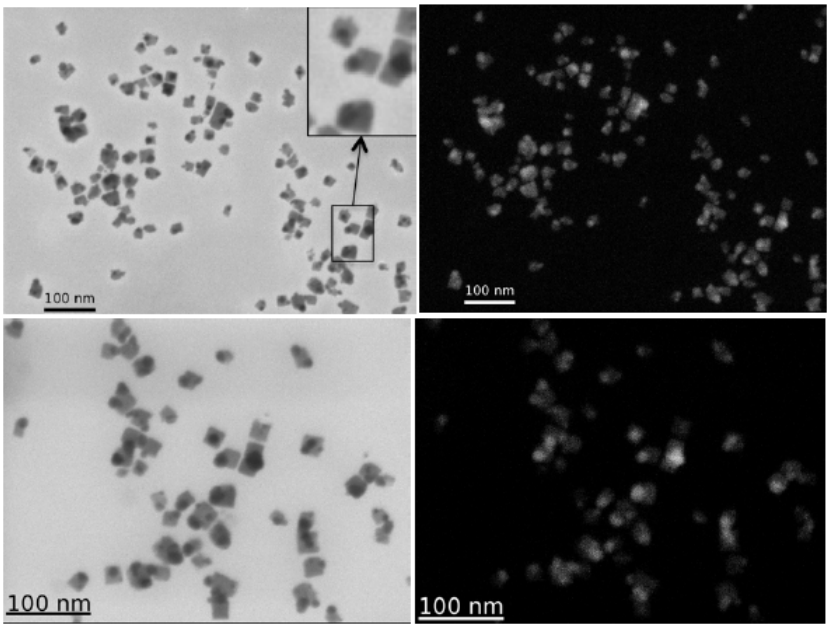

Figure 6.11 SEM images of AgNP-nylon-6 composite with a lower (top) and higher (bottom) magnification. The images on the right are obtained using COMPO mode. In the top-left image an enlargement of a selected section was made.

6.3.2 Nylon-6 polymer imaging using FLIM

The formation of nylon-6 encapsulating AgNP was also studied using a fluorescent lifetime image microscope by adding <1% of cumarin-6 to the precursors solution prior

irradiation.[18] The solution was spin coated and irradiated first with 365 nm LED and after with 405 nm LED. For this experiment, a lithographic mask of 6 μm was chosen, in order to have a sufficient amount of lines visible with a single scan, capturing emission signals above 405 nm. A schematic representation of the procedure used is reported in Figure 6.12.

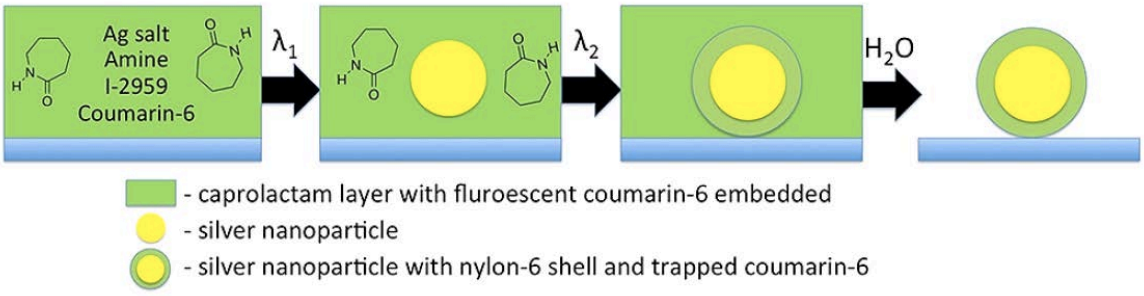

Figure 6.12 Schematic representation of the film preparation for the FLIM experiment. The system is shown after spin-coating of the precursor solution. In the first step AgNP are formed, after 365 nm irradiation. The second step led to the polymerization of nylon-6 after plasmon irradiation. During this step cumarin-6 is trapped inside the polymer. The final step consists on the washing of the film. [Figure reproduced from ref. 11]

In this experiment, the presence of cumarin-6 is required to ensure the possibility of visualizing the features obtained, by measuring its fluorescence. As described before, the caprolactam polymerization, induced by SPR irradiation of AgNP, results in the selective formation of nylon-6 around the nanoparticles. In this way, after washing the slide with water, cumarin-6 can be trapped only on the portions of the slide where the polymer is formed. FLIM images, illustrated in Figure 6.13, clearly show lines of 6 μm, which are distinguishable thanks to the cumarin-6 trapped in the nylon-6 shell surrounding AgNP.

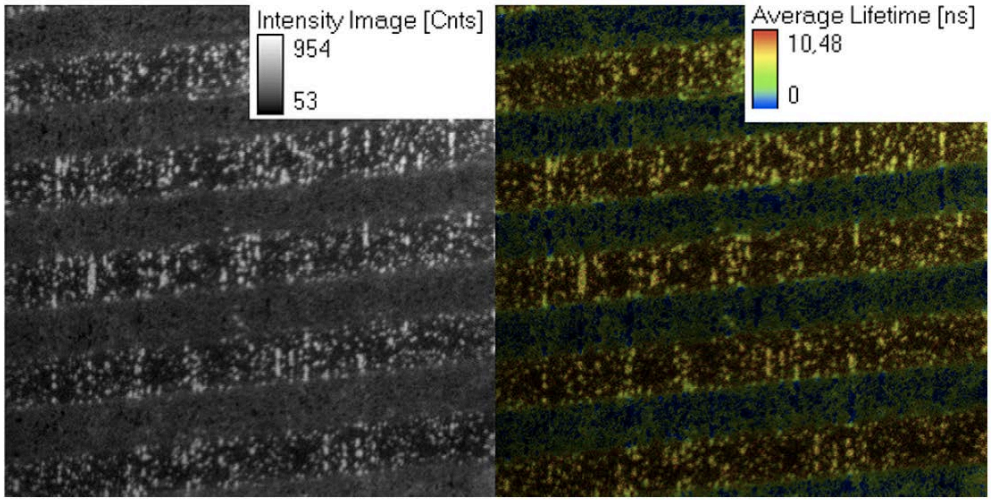

Figure 6.13 FLIM images of the film obtained in presence of cumarin-6. Intensity image (left) and lifetime image (right) of the film irradiated using a 6 μm mask. In both cases the area scanned is 80 x 80 μm^2.

From the analysis of the lifetime, we found a two-components decay, having 3.3 ns and 1.4 ns lifetimes (Figure 6.14, left). The lifetimes obtained are based on the FLIM images, as in Figure 6.13. The cumarin-6 lifetime measured in a PMMA film is 7.8 ns, and therefore longer than both values measured in our film. However, nylon-6 presents a much lower glass-transition temperature compared to PMMA, a parameter that can affect the lifetime measured.[19] In addition, the values obtained appear reasonable if we consider that cumarin-6 has a lifetime of 3.3 ns in acetonitrile.[20] The shorter component with a lifetime of 1.4 ns counts for a 40% of the emission and it can be attributed to the quenching effect of the silver nanoparticle on the cumarin-6.[21,22] Indeed, when the particles are not present, cumarin-6 presents just a single lifetime component, as shown in Figure 6.14 (right).

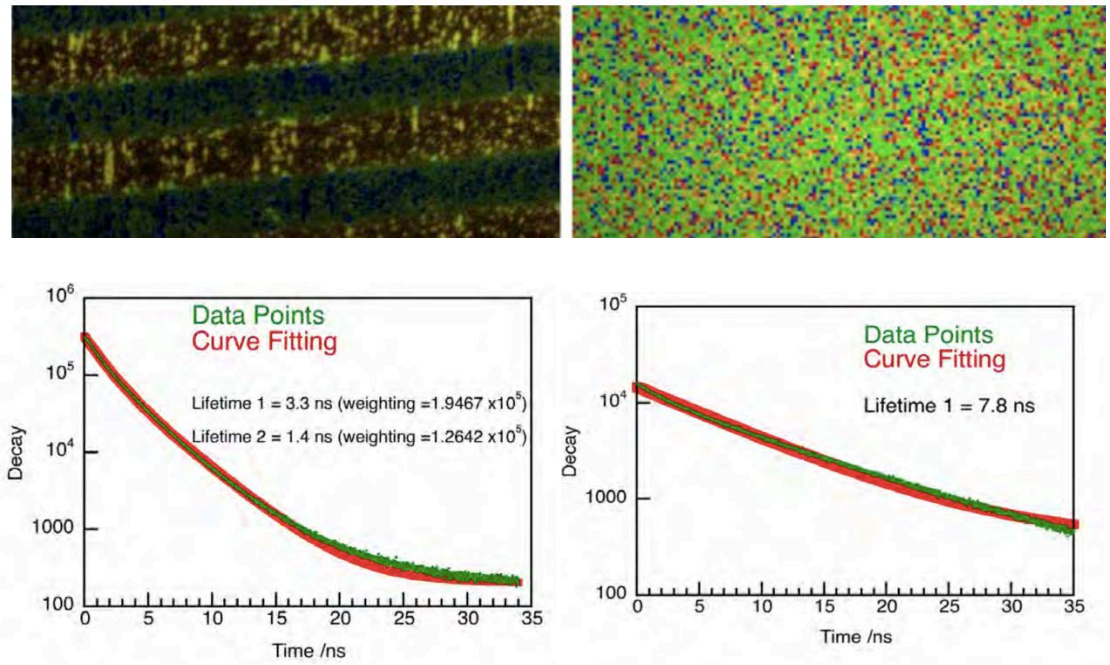

Figure 6.14 Lifetime trace of cumarin-6 trapped in nylon-6-AgNP composite (left) or in PMMA (right). On top the corresponding FLIM images are reported.

Summary

In conclusion, we developed a sub-wavelength dual-stage lithography process, where AgNP were used to induce the thermal polymerization of caprolactam by plasmon irradiation. The AgNP absorption in the visible makes the process inexpensive and convenient, in addition to the favorable high cross section. A macroscopic control of the features was obtained by the controlled reduction of Ag^{+} to AgNP, through a radical process, occurring in the exposed portions of a quartz disk coupled to a micrometric mask. The generation of sub-diffraction limit features was then possible by plasmon-induced polymerization of caprolactam around the irradiated particles.

This project represents an interesting proof-of concept when considering the use of plasmon as an alternative to commonly employed diffraction limited lithographic processes. In addition we moved a step forward in the localization of the features obtainable, compared to previous attempts in using plasmon as tool for lithography.

6.5 References

(1) Okoroanyanwu, U. Chemistry and Lithography. *SPIE and John Wiley and Sons*, **2010**.

(2) Jaeger, R. C. Lithography. *Introduction to Microelectronic Fabrication* (2nd ed.), **2002**.

(3) Hallett-Tapley, G. L.; Wee, T.-L.; Tran, H.; Rananavare, S. B.; Blackwell, J. M.; Scaiano, J. C. Single Component Photoacid/Photobase Generators: Potential Applications in Double Patterning Photolithography. *Journal of Materials Chemistry C*, **2013**, 1, 2657-2665.

(4) Moore, G. E. Cramming more Components onto Integrated Circuits. *Electronics*, **1965**, 38(8), 1-4.

(5) Stamplecoskie, K.G.; Pacioni, N. L.; Larson, D.; Scaiano, J.C. Plasmon-Mediated Photopolymerization Maps Plasmon Fields for Silver Nanoparticles. *Journal of American Chemical Society,* **2011**, 133(24), 9160–3.

(6) Deeb, C.; Bachelot, R.; Plain, J.; Baudrion, A.-L.; Jradi, S.; Bouhelier, A.; Soppera, O.; Jain, P. K.; Huang, L.; Ecoffet, C.; Balan, L.; Royer, P. Quantitative Analysis of Localized Surface Plasmons Based on Molecular Probing. *ACS Nano*, **2010**, 4, 4579−4586.

(7) Greenley, R. Z.; Stauffer, J. C.; Kurz, J. E. The Kinetic Equation for the Initiated, Anionic Polymerization of η-Caprolactam. *Macromolecules*, **1969**, 2, 561−567.

(8) Reimschuessel, H. K. Caprolactam Polymerization. *Journal of Polymer Science***, 1959**, 41, 57−466.

(9) Fasciani, C.; Bueno Alejo, C. J.; Grenier, M.; Netto-Ferreira, J. C.; Scaiano, J. C. High-Temperature Organic Reactions at Room Temperature Using Plasmon Excitation: Decomposition of Dicumyl Peroxide. *Organic Letters*, **2011**, 13(2), 204–207.

(10) Tanabe, K. Field Enhancement Around Metal Nanoparticles and Nanoshells: A Systematic Investigation. *Journal of Physical Chemistry C*, **2008**, 112(40), 15721–15728.

(11) Stamplecoskie, K. G.; Fasciani, C.; Scaiano, J. C. Dual-Stage Lithography From a Light-driven, Plasmon-Assisted Process: A Hierarchical Approach to Subwavelength Features. *Langmuir*, **2012**, 28(30), 10957–10961.

(12) Scaiano, J. C.; Hallett-Tapley, G. L.; Stamplecoskie, K. G. Photochemical

Norrish Type I Reaction as a Tool for Metal Nanoparticle Synthesis: Importance of Proton Coupled Electron Transfer. *Chemical Communications,* **2012**, 48, 4798–4808.

(13) Maretti, L.; Billone, P. S.; Liu, Y.; Scaiano, J. C. Facile Photochemical Synthesis and Characterization of Highly Fluorescent Silver Nanoparticles. *Journal of American Chemical Society,* **2009**, 131, 13972−13980.

(14) Stamplecoskie, K. G.; Scaiano, J. C. Light Emitting Diode Irradiation Can Control the Morphology and Optical Properties of Silver Nanoparticles. *Journal of American Chemical Society,* **2010**, 132(6), 1825–1827.

(15) Quinten, M. The Color of Finely Dispersed Nanoparticles. *Applied Physics B: Lasers and Optics,* **2001**, 73, 317−326.

(16) Mulfinger, L.; Solomon, S. D.; Bahadory, M.; Jeyarajasingam, A. V.; Rutkowsky, S. A.; Boritz, C. Synthesis and Study of Silver Nanoparticles. *Journal of Chemical Education,* **2007**, 84, 322.

(17) Encina, E. R.; Coronado, E. A. Plasmon Coupling in Silver Nanosphere Pairs. *Journal of Physical Chemistry C,* **2010**, 114, 3918−3923.

(18) Scaiano, J. C.; Laferriere, M.; Ivan, M. G.; Taylor, G. N. A Protocol for the Verification of Acid Generation in 157 nm Lithography. *Macromolecules,* **2003**, 36, 6692−6694.

(19) Ye, J. Y.; Hattori, T.; Nakatsuka, H.; Maruyama, Y.; Ishikawa, M. Microscopic Dynamics of the Glass Transition Investigated by Time Resolved Fluorescence Measurements of Doped Chromophores. *Physics Review B,* **1997**, 56, 5286−5296.

(20) Jones, G., II; Jackson, W. R.; Choi, C.-Y.; Bergmark, W. R. Solvent Effects on Emission Yield and Lifetime for Coumarin Laser Dyes. Requirements for a Rotatory Decay Mechanism. *Journal of Physical Chemistry.* **1985**, 89, 294−300.

(21) Anger, P.; Bharadwaj, P.; Novotny, L. Enhancement and Quenching of Single-Molecule Fluorescence. *Physical Review Letters,* **2006**, 96, 113002.

(22) Pacioni, N. L.; González-Béjar, M.; Alarcón, E.; McGilvray, K. L.; Scaiano, J. C. Surface Plasmons Control the Dynamics of Excited Triplet States in the Presence of Gold Nanoparticles. *Journal of American Chemical Society,* **2010**, 132, 6298−6299.

Chapter 7

Plasmon-Mediated ssDNA Dynamic Release from Gold Nanoparticles

7.1 Introduction

Light to heat conversion occurring after plasmon irradiation of metal nanoparticles has been successfully investigated, not only in the fields of catalysis and photolithography, but also for bio-applications, for therapeutics[1] and for sensing purposes.[2] Indeed, plasmon-mediated heating can have potential uses in processes such as polymerase chain reaction (PCR), eliminating external heating sources and keeping the bulk solution at temperatures near ambient temperature values. These advantages are possible since, as mentioned in the previous chapters, the heat released after plasmon irradiation of metal nanoparticles is extremely localized.[3] Halas et al.[4,5] and Branda et al.[6] investigated the use of light to induce chemical and biochemical release. Moreover, particular interest has been reversed on the study of DNA nanoparticles conjugates adopting several methodologies, such as electrochemical methods,[7] gel electrophoresis,[8] analytical centrifugation,[9] to name a few. Interestingly, the number of publications on this field is

increasing due to the need of having a better understanding of the thermoplasmonic release dynamics. A particular appealing method to investigate the ssDNA release after plasmon irradiation employs fluorescence spectroscopy techniques. The possibility of fluorescently label the dsDNA with specific dyes makes the system suitable for the investigation of the release procedure. Successful attempts were made in this direction.[4,5,10,11] Therefore, our contribution was aimed to study the ssDNA release *in situ*, using high–resolution microscopy with a subcellular dimension resolution.

Fluorescence lifetime imaging microscopy and total internal reflection microscopy were used to spatially identify the ssDNA release after plasmon irradiation, as schematized in Figure 7.1. The ssDNA could be tracked by fluorescence analysis of a labeling dye, ATTO 550, attached to the complementary DNA strand. The ATTO 550 fluorescence is quenched when the two DNA strands are coupled, but its emission increases when the DNA melts. Another dye, Cy5, was placed on the DNA strand covalently linked to the AuNP, just as a control.

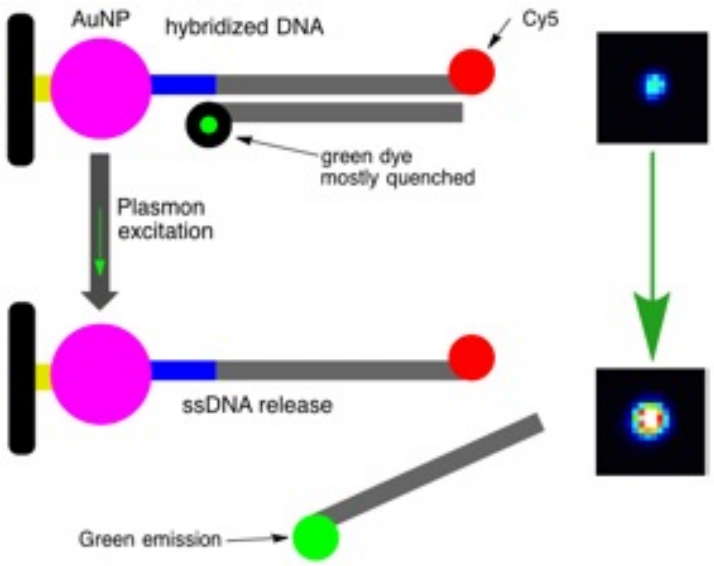

Figure 7.1 Schematic representation of the ssDNA release and corresponding fluorescence emission images of the ATTO 550 dye, after AuNP plasmon irradiation. dsDNA is attached through an amide bond between the bonded strand, Cy5 labeled, and the lipoic acid (in blue) functionalized AuNP. The glass surface (black bars on the left) is functionalized with APTES (yellow). Upon plasmon excitation, release of the ssDNA label with ATTO 550 takes place with a concomitant increase in the fluorescence intensity.

The designed system has furnished precious information regarding the plasmon potential in the DNA melting of DNA-AuNP conjugates, and therefore it represents a small step forward for its possible use in "real life" application.

7.2 Material and Methods

7.2.1 Materials

Tetrachloroauric acid (III) trihydrate ($HAuCl_4 \cdot 3H_2O$), hydrogen peroxide (H_2O_2, 50 wt. %), trisodium citrate, sulfo-*N*-hydroxysulfosuccinimide (sulfo-NHS), α-lipoic acid, NaH_2PO_4, Na_2HPO_4, MES, NaCl, phosphate buffered saline solution (PBS) and (3-aminopropyl) triethoxysilane (APTES) were purchased from Sigma-Aldrich. 1-Ethyl-3-(3-dimethylaminopropyl) carbodiimide (EDC) was purchased from Advanced Chemical Technologies (Oklahoma City, USA). H_2SO_4 (96%) was purchased from Honeywell Chemicals. Glass cover slips (24 x 40 x 0.15 mm) used for gold nanoparticles functionalization experiments were from Fisher Scientific. DNA experiments were performed with freshly prepared solutions in sterilized ultra pure water filtered through PTFE 0.22 μm pore size. Phosphate buffer (pH 7.4) was prepared using NaH_2PO_4 and Na_2HPO_4. DNA Duplex (Cy5 5-labeled sequence: 5'-5AmMC6AACACAAACACACTTAAACACAAACACACC-3Cy5Sp-3', ATTO550 5-labeled sequence: 5'-5ATTO550N-GGTGTGTTTGTGTTTAAGTGTGTTTGTGTT-3') was purchased from Integrated DNA Technologies and suspended in PBS (pH 7.4, [NaCl] = 10 mM). The DNA solution was divided in aliquots and the vials were kept at -80°C. The melting temperature for the oligo nucleotides employed here varies from 43 to 74°C for 10 to 1200 mM Na^+ concentration, respectively.[12] Amino modified ATTO550 dye was purchased from ATTO-TEC (Siegen, Germany) and suspended in anhydrous DMSO.

7.2.2 Nanoparticle Synthesis

Gold nanoparticles were synthesized according to the Turkevich method.[13] In this procedure 5 ml of trisodium citrate (1.0% w/v) are added to 95 ml of tetrachloroauric acid (25 mM) solution and left stirring for 30 minutes at 100ºC. The particles obtained have an average diameter of 22 ± 3.0 nm and an estimated concentration of 2.0 nM.

7.2.3 Glass Slides Functionalization

Prior functionalization the coverslips were cleaned in piranha solution (H_2O_2:H_2SO_4, 1:3) for 1 h and then rinsed thoroughly with water. After carefully drying the slides using N_2 flow, the surface was immersed in a 4% v/v aminopropyltriethoxysilane (APTES) toluene solution for 1 h. The coverslips were then washed with acetone, ethanol and milliQ water and then dried. At this point the AuNP functionalization was performed placing 1.3 ml of the AuNP stock solution on top of each coverslip for 25 min. The slides were finally rinsed with milli-Q water and dried. Figure 7.2 shows a schematic representation of this functionalization step, where the APTES acts as a bridge between the glass slide and the AuNP.

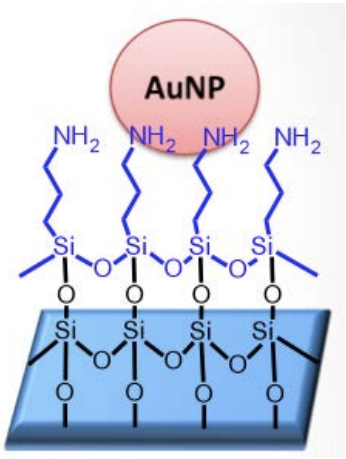

Figure 7.2 Schematic representation of coverslip functionalized with APTES and AuNP.

The following step consists in the interaction between the AuNP and lipoic acid, obtained by placing 2 ml of a lipoic acid solution (1 mM) on the slide for 2 h. This time was sufficient to allow the interaction between the AuNP and the two atoms of sulfur. Finally the solution was rinsed with water and the coverslips were dried with N_2.

7.2.4 DNA Functionalization

To perform the dsDNA functionalization, the amine group in the dsDNA was coupled to the free carboxylic acid group of the functionalized AuNP-lipoic acid slides. 1.3 ml of a solution mixture of dsDNA (10 nM), EDC (20 mM), sulfo–NHS (15 mM), MES buffer (0.1 M, pH = 6.0) and NaCl (1.0 M) were placed onto the lipoic acid AuNP functionalized coverslips, and incubated in a humidity chamber at 4°C for 3.5 h. After this time, the remaining solution was removed and stored at −80°C for further characterization. The slide obtained was washed with PBS (pH 7.4; [NaCl] = 10 mM), dried and immediately used for the imaging experiments.

7.2.5 Amino modified ATTO550 dye Functionalization (ATTO550@AuNP)

Control experiments using the amino modified ATTO550 dye onto the AuNP functionalized slides were performed with slides prepared following the same protocol as the DNA fictionalization, but using 10 nM amino-ATTO550 instead of the dsDNA.

7.2.6 dsDNA Melting Temperature Determination

In order to determine the melting temperature (**T_m**) of the free dsDNA and the dsDNA@AuNP construct, emission spectra of ATTO550-ssDNA release were recorded, placing the system in a thermo-regulated bath at different temperatures. The experiments were conducted by using a clean 1.0 cm length quartz cuvette filled with 1.5 ml of dsDNA (10 nM, phosphate buffer, [NaCl] = 10 mM; pH 7.4) for the experiment related to free dsDNA. Instead, in the case of dsDNA@AuNP system, the quartz cuvette was first functionalized with AuNP, lipoic acid and dsDNA, following the same procedure

reported in the previous paragraph, and then 2.5 ml of phosphate buffer (pH 7.4; [NaCl] = 10 mM) were added into the cuvette. The cuvettes were placed in the water bath and heated gradually. Emission spectra were collected from 550 to 700 nm after 10 min for each set temperature exciting at 530 nm. The integrated area under the curve was plotted as a function of temperature. Finally the T_m was obtained by the corresponding Gaussian fit of the first derivative of the intensity as a function of temperature.

7.2.7 LED irradiation experiments

ssDNA release was monitored measuring the fluorescence intensities of the ATTO550 and Cy5 labels after 10 min of 532 nm LED irradiation (0.31 W/cm^2) of a PBS drop (pH 7.4; [NaCl] = 10 mM), placed over the DNA-AuNP conjugates. Aliquots of 500 µl were collected for several experiments until a final volume of 1.5 ml was obtained. The ssDNA release was quantified by comparing the fluorescence intensities obtained with a standard fluorescence calibration curve for each dye.

7.2.8 Fluorescence microscopy experiments

Real time experiments were carried out using TIRF and FLIM microscopes. The functionalized coverslips were placed on top of the oil immersion objective (Figure 7.3) and fluorescence emission images and spectra were recorded in the range of 561-609 nm or 640-676 nm after excitation at 543 and 633 nm respectively, using a He-Ne CW laser.

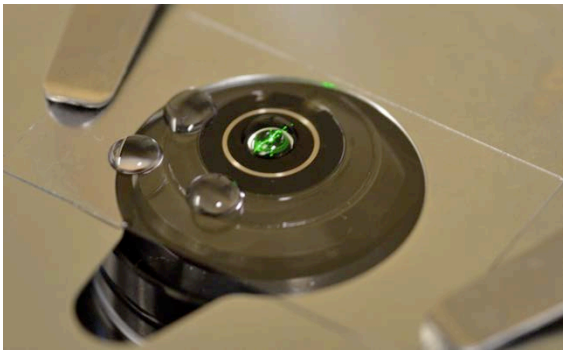

Figure 7.3 Picture of a functionalized glass slide placed on top of the oil immersion objective. TIRF and FLIM images were collected using this setup.

The density power of the excitation laser in the sample was estimated to be 14 W/cm^2 or 40 W/cm^2 (100%) for 543 and 633 nm respectively. Specification of the TIRF and FLIM instrumentation are reposted in Chapter 2.

7.3 Fluorescence microscopy imaging of the ssDNA release

We designed a system in which a quartz coverslip was functionalized with APTES, in such a way that the ethoxysilane portions could interact with the slide and the amino groups could trap the AuNP. Cryo –SEM images showed particles with a mean diameter of 22 ± 3 nm (Figure 7.4).

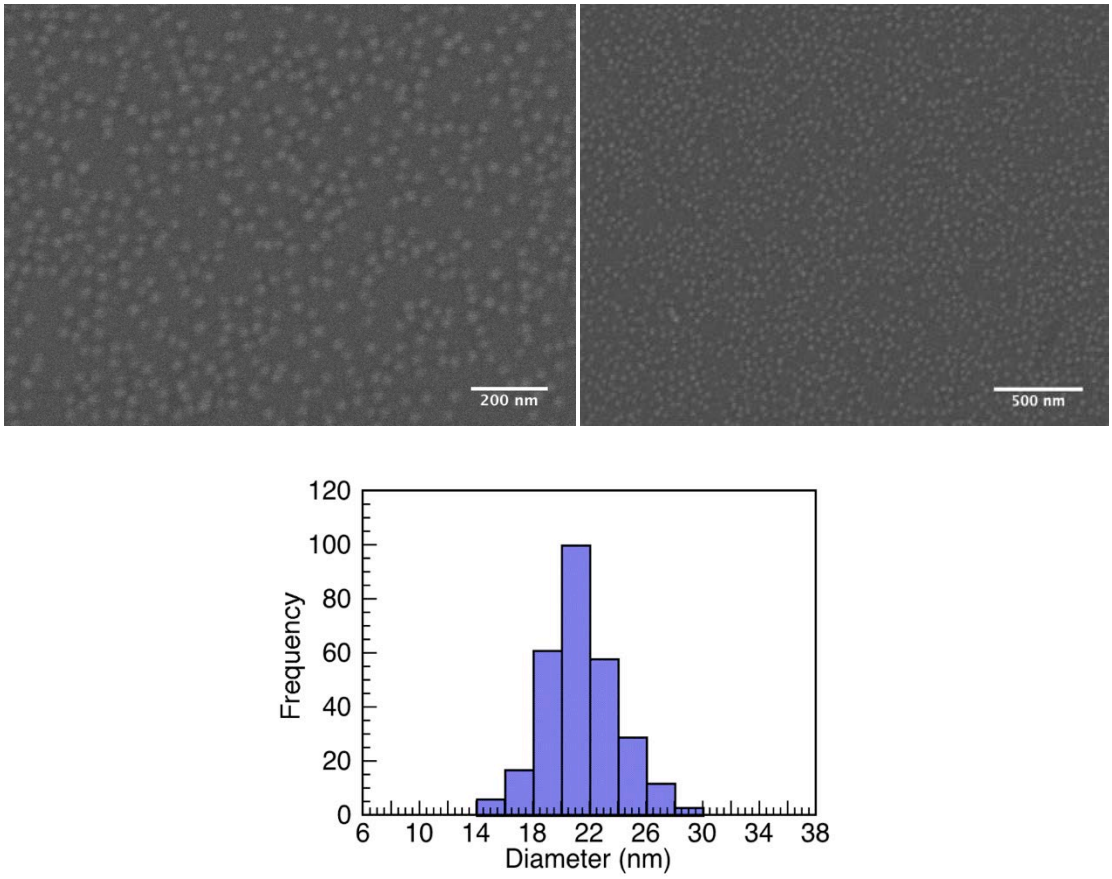

Figure 7.4 (Top) Cryo-SEM pictures of a cover slip functionalized with AuNP. (Bottom) Histogram of the AuNP size distribution.

A 30 bp dsDNA was then anchored to AuNP by the lipoic acid sulfur "feet" and a six-carbon spacer. A schematic representation of the anchor/linker used is reported in Figure 7.5. In this designed system only one of the two strands of DNA is covalently linked to the AuNP, therefore the ssDNA release does not involve the cleavage of a covalent bond. Moreover, the use of lipoic acid ensures a stable linkage between DNA and AuNP. Branda reported a threshold of 0.5 W/cm^2 for the breaking of S-Au bond when using a single SH anchor.[11] Respect to monothiol linkers, lipoic acid has been shown to increase the stability of the DNA-AuNP conjugates.[10,14]

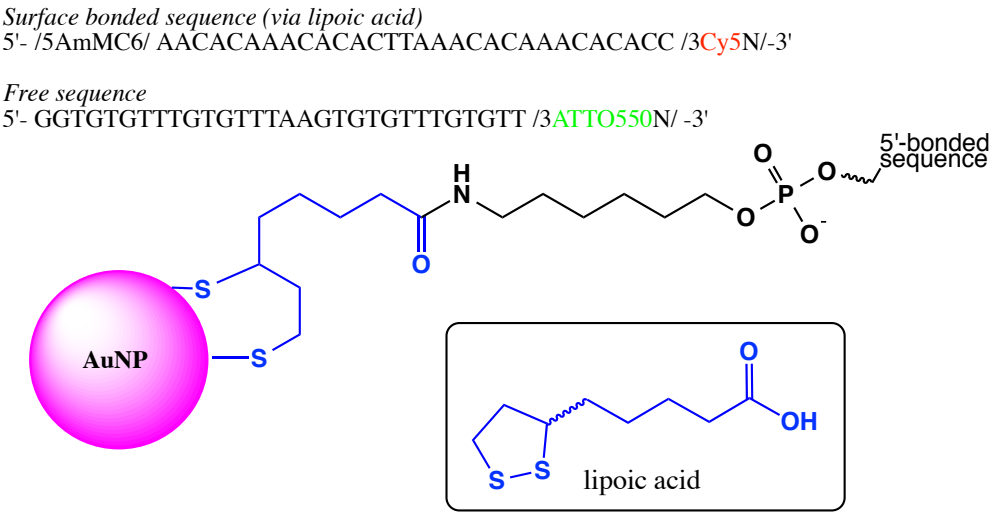

Figure 7.5 Schematic representation of the AuNP functionalized with lipoic acid and DNA sequence.

The slide functionalization results in a surface coverage of ~ 46 %. This value was measured comparing the emission of unattached dsDNA (λ_{exc} = 520 nm; λ_{em} = 540 - 650 nm, R=0.9972) collected after incubation of the dsDNA solution on the lipoic acid functionalized AuNP slips, with a calibration curve of dsDNA stock solution, using the same incubation conditions.

As mentioned before, the DNA strands were labeled with two different fluorescent dyes. Cy5 was used to label the strand directly linked to the AuNP, while ATTO550 was employed for the complementary strand. The choice of the two dyes was made based on the respective excitation and emission spectra (ATTO 550: λ_{exc} = 550 nm, λ_{em}= 575 nm;

Cy5: λ_{exc}= 633 nm, λ_{em}= 670 nm), reported in Figure 7.6, which appear to be suitable for our experimental setup.

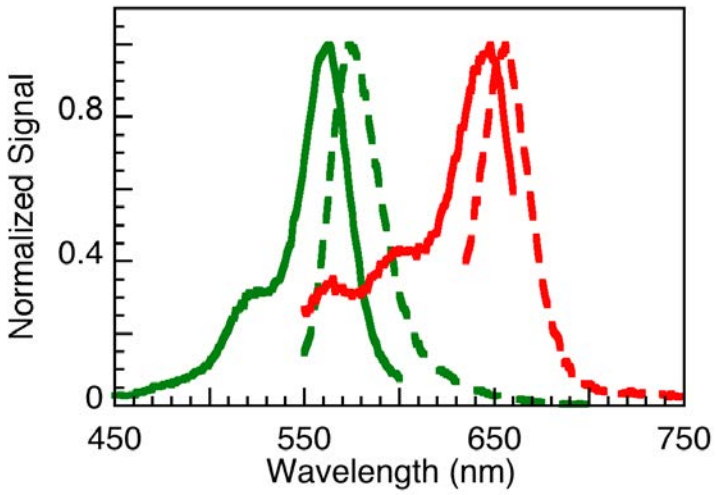

Figure 7.6 Excitation (full line) and emission (dashed line) spectra of the dsDNA labeled with ATTO550 (green) and Cy5 (red) (100 nM dsDNA in phosphate buffer; [NaCl] = 10 mM; pH 7.4) at 25.0 ± 0.5˚C.

A quantification of the quenching effect exerted by the AuNP on the two dyes was done using a simplified analytical model described by Novotny.[15] The proximity between a fluorophore and a metal particle can result in an increase of the excitation and emission or it can promote non-radiative energy transfer from the molecule to the particle. Equation 7.1 shows the gain in brightness (GB) resulting from those interactions:

$$GB = \left| 1 + 2\frac{1}{\left(1+\frac{h}{a}\right)^3}\frac{\varepsilon(\omega_{exc}) - \varepsilon_m}{\varepsilon(\omega_{exc}) + 2\varepsilon_m} \right|^2 \frac{\Phi}{\Phi^0} \qquad (7.1)$$

where Φ^0 is the intrinsic molecule quantum yield, h is the distance between the fluorophore and the nanoparticles, a is the radius of the NP, $\varepsilon(\omega_{exc})$ is the frequency-dependent particle dielectric constant at the excitation wavelength and ε_m is the

dielectric constant of the surrounding medium. The resulting plots of the GB *vs.* the distance between the fluorophore and the AuNP are shown in Figure 7.7.

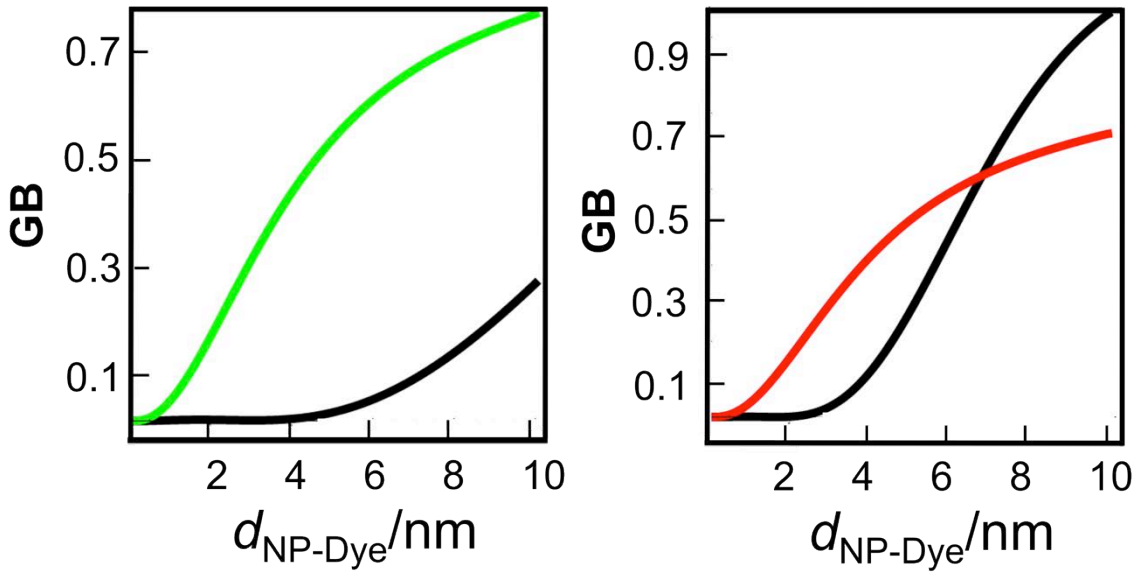

Figure 7.7 Calculated gain in brightness for (left) ATTO 550 (λ_{exc} = 543 nm) and (right) Cy5 (λ_{exc} = 633 nm) with emissions at 575 and 670 nm respectively as a function of the AuNP surface−fluorophore distance. Both scenarios parallel (colored line) and perpendicular (black line) dipole orientation with respect to the incident light have been included.

The fluorescence of the ATTO 550 attached at the complementary strand of the DNA, results quenched for the 80-95% of its intensity, due to the fact that the dye is located 2 nm far from the AuNP surface. Meanwhile, Cy5 is placed at 8 nm from the particle surface and therefore maintains most of its brightness (70-90% of the initial value).

Once the system has been characterized, we proceeded with the performance of a real time thermoplasmonic release of ssDNA, monitored by TIRF microscopy. The functionalized coverslips were excited using 543 or 633 nm CW laser and the resulting images were taken up to 250 s. Figure 7.8 shows the emissions spots, after 543 nm excitation, at different times and using different irradiances. As expected, the emission spectra and the lifetimes of the fluorescent spots obtained exciting at 543 nm correspond to those of ATTO 550.

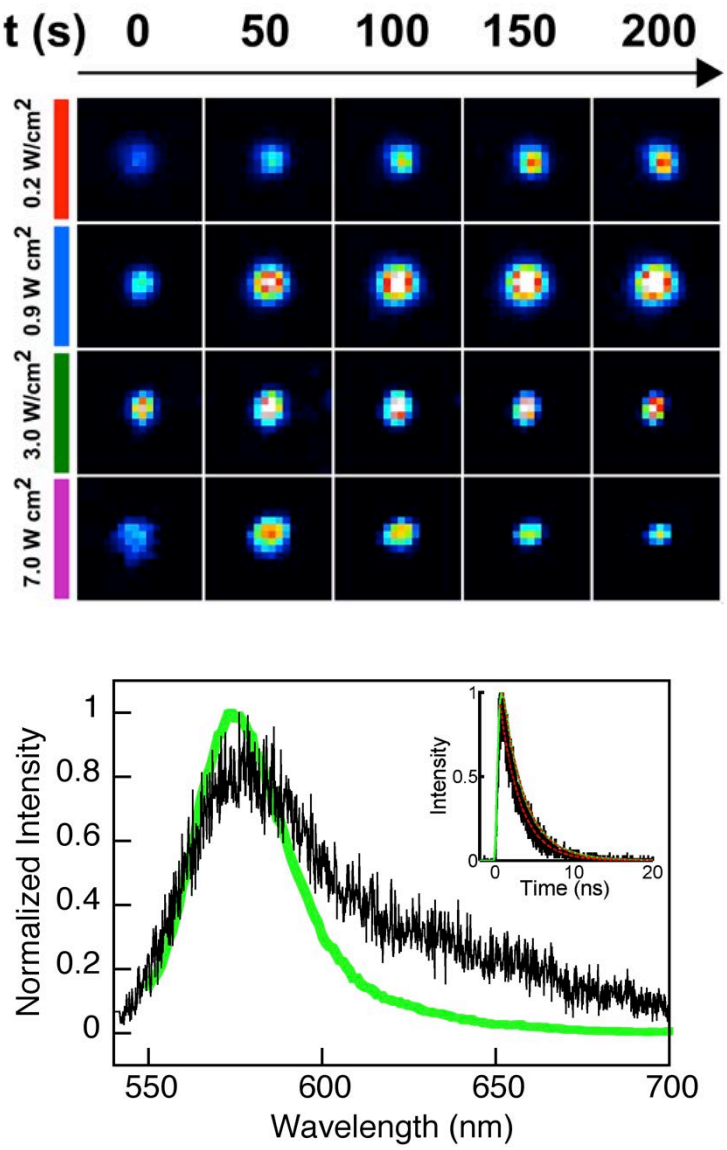

Figure 7.8 (Top) Fluorescence intensity images of ssDNA-ATTO550 release as a function of the irradiation time and the irradiance. The area of each image is 9 μm^2 (pixel size 156 nm). The image uses a LUT false color scheme to represent the intensity of the fluorescence signal. (Bottom) Comparison of the emission spectra for ATTO550 in solution (green) and ATTO550 released from dsDNA-AuNP conjugates (black) upon plasmon excitation. Insert: ATTO550 fluorescence decay under the same experimental conditions ($\tau_f \sim 2.5$ ns).

Interestingly, the emission intensity changes according to the energy power used. For the lower irradiances used (0.2 W/cm^2 and 0.9 W/cm^2), we noticed an increase of the emission intensities proportional to the time of irradiation. The ssDNA release after

plasmon irradiation allows the ATTO550 to escape from the quenching zone and thus, it produces an increase of the fluorescence intensity. However, when using irradiances of 3.0 W/cm^2 or 7.0 W/cm^2, the emission increases during the first 50 s for then decreasing during the following 150 s. In the latter cases, we are probably looking at bleaching processes happening after the first 50 s, due to the high values of the power used. Moreover, equivalent experiments conducted irradiating at 633 nm, corresponding to the excitation wavelength of the Cy5, show exclusively a decrease of the emission intensity, due to the bleaching of the dye. The results obtained are comparable to those recorded for the DNA-Cy5 in solution. (Figure 7.9)

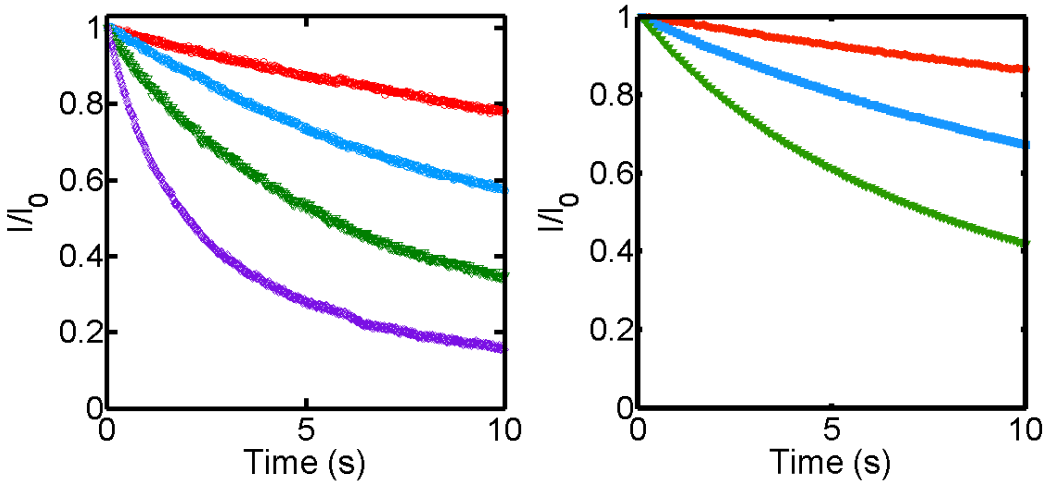

Figure 7.9 (Left) Average relative fluorescence intensities events of ssDNA-Cy5 attached to the AuNP (phosphate buffer, [NaCl] = 10 mM, pH 7.4) as a function of the exposure time and the power intensity (λ_{exc} = 633 nm, CW): 0.6 W/cm^2 (red), 2.4 W/cm^2 (blue), 8.0 W/cm^2 (green), 20.0 W/cm^2 (violet). (Right) Average relative fluorescence intensities events of DNA-Cy5 free in solution using the same conditions.

To establish if the ATTO550 emission was consistent with the ssDNA release, a blank experiment was prepared analyzing a lipoic acid-AuNP glass slide functionalized with amino-ATTO550 (see paragraph 7.2.5). In this system the ATTO550 is covalently linked to the AuNP, therefore an increase of the emission would not be due to the photothermal ssDNA release. The results of this experiment are reported in Figure 7.10 and the only

effect we noticed was the decrease of the ATTO550 emission due to photobleaching process.

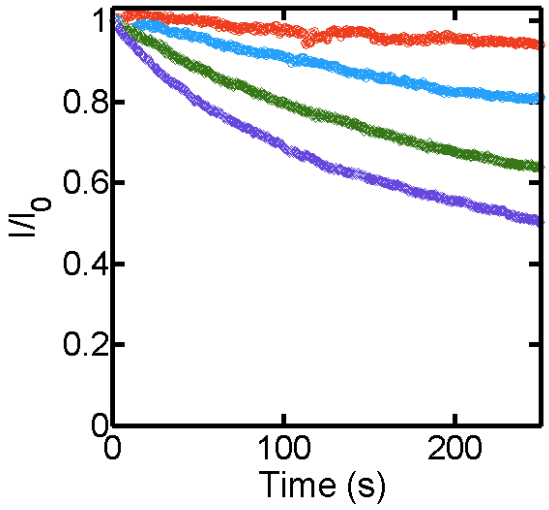

Figure 7.10 Average relative fluorescence intensities events of AuNP@ATTO550 conjugates (phosphate buffer, [NaCl] = 10 mM, pH 7.4) as a function of the exposure time and the power intensity (λ_{exc} = 543 nm, CW): 0.2 W/cm^2 (red), 0.9 W/cm^2 (blue), 3.0 W/cm^2 (green), 7.0 W/cm^2 (violet). The set sample size is between 50-90 detected events for each of the power intensities.

In order to further prove that we are releasing the ssDNA and not breaking the Au-S bonds, LED irradiation experiments were performed (530 nm, 0.31 W/cm^2). In those experiments a drop of PBS (pH 7.4; [NaCl]=10 mM) was placed over a dsDNA functionalized AuNP slide. As reported in paragraph 7.2.7, aliquots were taken after 10 min of irradiation and the resulting emission was analyzed. The only emission signal detected corresponded to the ATTO550, while no Cy5 emission was measured above the detection limit of 0.30 nM. These observations rule out the possibility that the dsDNA could be detached from the AuNP, after plasmon excitation.

Another plausible event could be the physical desorption of the oligo nucleotides from the AuNP functionalized slide. To investigate this possibility, the system was incubated with 10 mM PBS (pH 7.4) for 24 and 36 h. The fluorescence analysis confirmed that no emission is detected without plasmon irradiation.

The results obtained by TIRF analysis, performed irradiating at 543 nm and using four different power light intensities (0.2 W/cm^2, 0.9 W/cm^2, 3.0 W/cm^2 and 7.0 W/cm^2), suggested a different temporal performance of the system at each power used. Indeed, a variation of the initial slope of the fluorescence intensities as a function of exposure time was observed for the four experiments. Apparently, the ssDNA release appeared faster when increasing the laser irradiances, as shown in Figure 7.11.

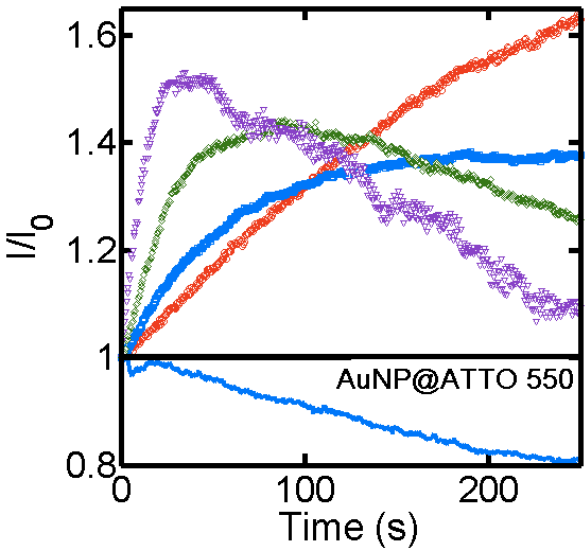

Figure 7.11 Average relative fluorescence intensities events monitored in-situ in a TIRF microscope of ssDNA-ATTO550 release from the AuNP (phosphate buffer, pH 7.4, [NaCl] = 10 mM) as a function of the exposure time and the power intensity (λ_{exc} = 543 nm, CW): 0.2 W/cm^2 (red), 0.9 W/cm^2 (blue), 3.0 W/cm^2 (green), 7.0 W/cm^2 (violet). AuNP@ATTO 550 conjugates were also tested as a control experiment (bottom). The set sample size is between 50-90 detected events for each of the power intensities.

However, if we consider the total energy delivered we will notice that the fluorescence enhancement depends only on the total energy and not on the rate of delivery, with the only exception being at low irradiance values. (Figure 7.12) At low energy, indeed, the emission increase appears faster probably due to presence of an excess of not hybridized ATTO labeled chains. Nonetheless, this effect appears too small to affect the results when using higher irradiances.

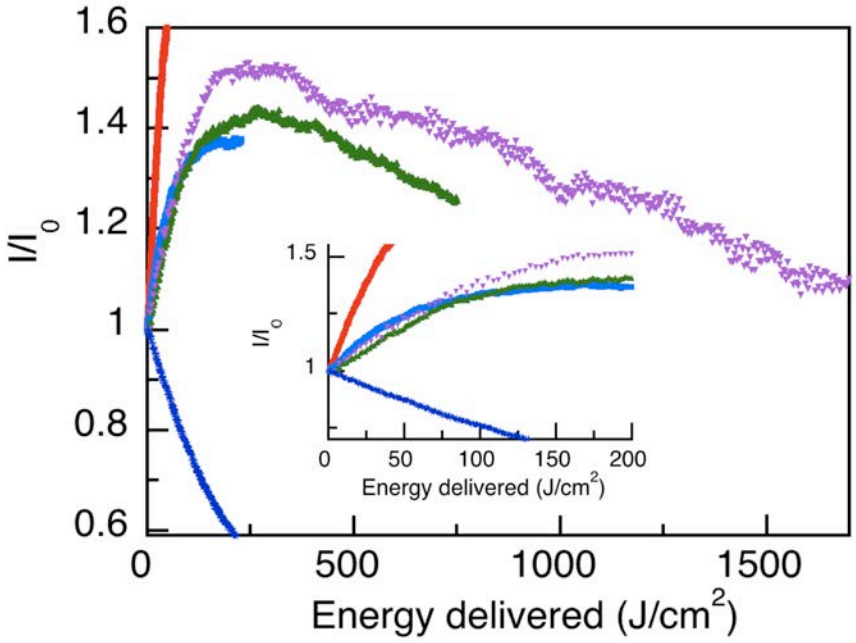

Figure 7.12 Fluorescence intensity enhancement for ssDNA-ATTO550 release events as a function of total energy delivered. Average between 50-90 intensity vs. time curves measured over single bright spots (see Figure 7.8) are plotted for each of the irradiances (red for 0.2, blue for 0.9, green for 3.0 and purple for 7.0 W/cm^2). ATTO550@AuNP conjugates were also tested as a control experiment (blue, 0.9 W/cm^2, showing only emission decrease). (Insert) Expansion of the low energy region.

The dependence of the ssDNA release process on the total energy rather than on the rate of energy delivery, makes this process suitable to be performed with convenient light sources such as LED, as an alternative to expensive lasers.

7.4 dsDNA melting temperature and plasmon heating

The dsDNA chosen for our study has a melting temperature of 52 ± 2°C at 10 mM NaCl, as reported in Figure 7.13. In previous studies,[5] it has been established that the DNA melting temperature increases when it is coupled to the surface of a gold nanoparticle. Indeed, by measuring the melting temperature of the dsDNA in our system we found that its value increases to 66 ± 1°C (Figure 7.13).

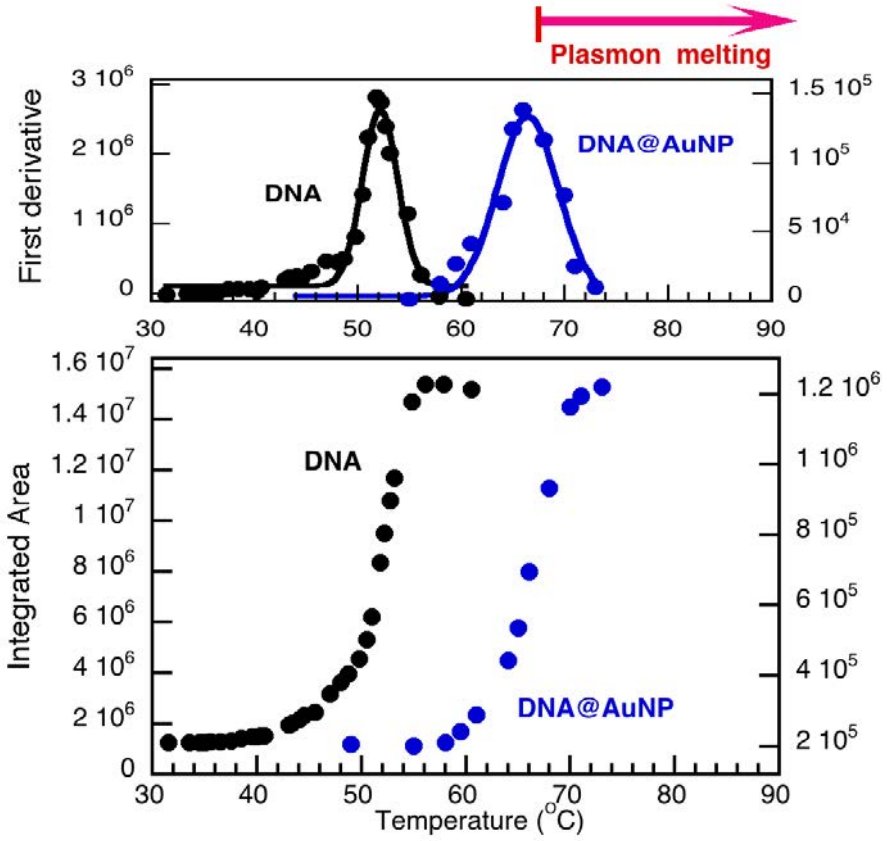

Figure 7.13 Melting curves for dsDNA in solution and when bound to AuNP. The top panel shows the first derivative plots. The data correspond to the fluorescence increase as the temperature is raised and the right axis is for DNA@AuNP. Note that the intensity values are smaller for DNA@AuNP, a measure of the low amount of DNA available at the surface and the difficulties of this measurement.

This indication suggests that in order to have a ssDNA release the plasmonic excitation should led to values of localized temperatures that exceed 66°C. Baffou and Quidant demonstrated that the irradiation of spherical AuNP (20 nm) in water, using a 530 nm light source with an irradiance of 1 mW/μm^2, would determine an increase of the bulk solution temperature of 5ºC.[3] Therefore, the increase in steady state temperature that we should expect in our system are much lower, due to the lower irradiances employed. This observation clearly discards the possibility of dsDNA melting favored by an increase of the overall solution temperature and therefore it strengthens the hypothesis of a localized plasmon-mediated ssDNA release.

7.5 Summary

With this project we were able to monitor the thermoplasmonic ssDNA release upon plasmon irradiation *in situ,* by measuring the fluorescence emission of labeling dyes employing TIRF technique. Our findings indicate that irradiation of metal nanoparticles led to the release of heat, which is able to promote the dsDNA melting. In the previous chapters, we described how the plasmon heating effect could have promising application in catalysis and photolithography, with this project we proved that its potential could be extended to bio-applications. The possibility to explore this direction is even more encouraging if we consider the spatial and temporal selectivity that a photodynamic process could bring to the common PCR methodology.

Moreover, another interesting aspect is related to the rate of the ssDNA release, which resulted dependent only on the total energy dose and not on the rate with which this energy is delivered. Therefore, these processes can be triggered either by expensive lasers or by more affordable and convenient light sources, such as LED.

My contribution in this specific project was aimed to the design and the analysis of the experimental setup to follow the dehybridization process. The TIRF experiments were run in collaboration with Sabrina Simoncelli, a visiting student from Argentina and Hasita Weerasekera as part of his honor project.

7.6 References

(1) (a) Huang, X.; El-Sayed, I. H.; Qian, W.; El-Sayed, M. A. Cancer Cell Imaging and Photothermal Therapy in the Near-Infrared Region by Using Gold Nanorods. *Journal of American Chemical Society,* **2006**, *128*, 2115-2120; (b) Huang, X. H.; Jain, P. K.; El-Sayed, I. H.; El-Sayed, M. A. Determination of the Minimum Temperature Required for Selective Photothermal Destruction of Cancer Cells with the Use of Immunotargeted Gold Nanoparticles. *Photochemistry and Photobiology,* **2006**, *82*, 412-417.

(2) Coll, C.; Bernardos, A.; Martínez-Máñez, R.; Sancenón, F. Gated Silica Mesoporous Supports for Controlled Release and Signaling Applications. *Accounts of Chemical Research,* **2013**, *46*, 339-349.

(3) (a) Baffou, G.; Quidant, R. Thermo-Plasmonics: Using Metallic Nanostructures as Nano-Sources of Heat. *Laser & Photonics Reviews***, 2013**, *7*, 171-187. (b) Baffou, G.; Quidant, R.; GarcÃıa de Abajo, F. J. Nanoscale Control of Optical Heating in Complex Plasmonic Systems. *ACS Nano,* **2010**, *4*, 709-716. (c) Cororado, E. A.; Encina, E. R.; Stefani, F. D. Optical Properties of Metallic Nanoparticles: Manipulating Light, Heat and Forces at the Nanoscale. *Nanoscale,* **2011**, 3, 4042-4059.

(4) Barhoumi, A.; Huschka, R.; Bardhan, R.; Knight, M. W.; Halas, N. J. Light-Induced Release of DNA from Plasmon-Resonant Nanoparticles: Towards Light-Controlled Gene Therapy. *Chemical Physics Letters,* **2009**, *482*, 171-179.

(5) Huschka, R.; Zuloaga, J.; Knight, M. W.; Brown, L. V.; Nordlander, P.; Halas, N. J. Light-Induced Release of DNA from Gold Nanoparticles: Nanoshells and Nanorods. *Journal of American Chemical Society,* **2011**, *133*, 12247-12255.

(6) (a) Bakhtiari, A. B. S.; Hsiao, D.; Jin, G.; Gates, B. D.; Branda, N. R. An Efficient Method Based on the Photothermal Effect for the Release of Molecules from Metal Nanoparticle Surfaces. *Angewandte Chemie International Edition,* **2009**, *48*, 4166-4169; (b) Yan, B.; Boyer, J.-C.; Habault, D.; Branda, N. R.; Zhao, Y. Near Infrared Light Triggered Release of Biomacromolecules from Hydrogels Loaded with Upconversion Nanoparticles. *Journal of American Chemical Society,* **2012**, *134*, 16558-16561.

(7) Steel, A. B.; Herne, T. M.; Tarlov, M. J. Electrochemical Quantitation of DNA Immobilized on gold. *Analytical Chemistry,* **1998**, 70, 4670–4677.

(8) Pellegrino, T.; Sperling, R. A.; Alivisatos A. P.; Parak, W. J. Gel Electrophoresis of Gold-DNA Nanoconjugates. *Journal of Biomedicine and Biotechnology,* **2007**, 2007, 26796.

(9) Falabella, J. B.; Cho, T. J.; Ripple, D. C.; Hackley V. A.; Tarlov, M. J. Characterization of Gold Nanoparticles Modified with Single-Stranded DNA Using Analytical Ultracentrifugation and Dynamic Light Scattering. *Langmuir*, **2010**, 26, 12740–12747.

(10) Guerrini, L.; Barrett, L.; Dougan, J. A.; Faulds, K.; Graham, D. Improving the Understanding of Oligonucleotide–Nanoparticle Conjugates Using DNA-Binding Fluorophores. *Nanoscale*, **2013**, 5, 4166–4170.

(11) Poon, L.; Zandberg, W.; Hsiao, D.; Erno, Z.; Sen, D.; Gates, B.; Branda, N. Photothermal Release of Single-Stranded DNA from the Surface of Gold Nanoparticles through Controlled Denaturating and Au-S Bond Breaking. *ACS nano,* **2010**, *4*, 6395-6403.

(12) Owczarzy, R.; Moreira, B. G.; You, Y.; Behlke, M. A.; Walder, J. A. Predicting Stability of DNA Duplexes in Solutions Containing Magnesium and Monovalent Cations. *Biochemistry,* **2008**, *47*, 5336-5353.

(13) Turkevich, J.; Stevenson, P. C.; Hillier, J. A Study of the Nucleation and Growth Processes in the Synthesis of Colloidal Gold. *Discussion of the Faraday Society,* **1951**, *11*, 55-75.

(14) Barrett, L.; Dougan, J. A.; Faulds, K. Graham, D. Stable Dye-Labeled Oligonucleotide-Nanoparticle Conjugates for Nucleic Acid Detection. *Nanoscale*, **2011**, 3, 3221–3227.

(15) (a) Anger, P.; Bharadwaj, P.; Novotny, L., Enhancement and Quenching of Single-Molecule Fluorescence. *Physical Review Letters,* **2006**, *96*, 113002; (b) Bharadwaj, P.; Novotny, L. Spectral Dependence of Single Molecule Fluorescence Enhancement. *Optics Express,* **2007**, *15*, 14266-14274.

Chapter 8

Functionalization of Graphene Oxide with Metal Nanoparticles

8.1 Introduction

In the final part of my PhD, I had the chance of working with carbon-based materials, such as graphene and graphene oxide. The interest on those particular materials started in occasion of a three months exchange period at the "Instituto de Tecnología Química" en Valencia, for a collaboration project with Prof. Hermenegildo Garcia. During those months, I had the opportunity to work with researchers with a high expertise in the synthesis and use of graphene and other carbon materials in a wide range of fields. My principal interest at that point was based on the acquisition of a basic practical knowledge, for then explore the possibility of modifying and functionalizing those materials using techniques and procedures developed in the Scaiano's group.

In the last few years graphene (G), graphene oxide (GO) and reduced graphene oxide (rGO) have received considerable attention due to their electrical, thermal and

mechanical properties, making these materials promising for many applications.[1] Exploring outstanding physical and chemical properties of graphene and its derivatives and understanding their response to various experimental conditions are an indispensable step in developing graphene-based devises for high performance applications. Owing the extraordinary chemical structure (known as the Dirac fermion system)[2] of graphene, extremely high thermal conductivity (3080 to 5150 W m^{-1} K^{-1}),[3] high carrier mobility (15 000 cm^2 $V^{-1}s^{-1}$ at room-temperature)[4], and high optical transmittance (~ 97.7%)[4] have been found as exceptional properties of graphene. Mechanical properties of graphene are indeed more astonishing; the elastic modulus is about 0.25 TPa and intrinsic strength of a defect-free monolayer graphene is 130 GPa.[4] Despite having extraordinary properties, for many applications it is often required to chemically or physically (e.g. morphology) modify the graphene to achieve the best outcome.

For instance Koratka et al. demonstrated that creating microscale pores, cracks, and voids in graphene paper enables efficient intercalation kinetics for lithium ions at ultrafast charge/discharge rates.[5] A lithium battery fabricated using this cracked graphene paper displayed the highest capacity for a pure carbon anode without any additives. Beyond conventional approaches (*e.g.* graphene-ligand covalent and non-covalent interactions or deposition of metal oxide nanoparticles), a wide range of methods and techniques have been developed to structurally modify graphene and its derivatives; including metal-mediated etching,[6] hydrothermal method[7] and photochemical engineering under UV irradiation (nanopores formation),[8] to name a few.

Moreover, on top of the morphological modification, chemical modification has also been used as a tool to make new and promising graphene based materials, with a specific composition. As a simple example, the oxidation of graphene led to the formation of GO. Compared to graphene, GO presents peculiar physical and mechanical properties in addition to the different chemical composition. Recently GO has been applied in fields such as biology,[9] catalysis[10] and solar cells;[9] several reports focus on the use of GO as substrate for nanocomposite materials,[11] since it has a surface functionalized with oxygen groups, which enables the dispersion of this material in water and suitable sites to interact with other molecules.[12] Hybrid materials made with GO and metal

nanoparticles could be used for chemical sensing, optoelectronics or biology.[11] For example, gold nanoparticles (AuNP) or silver nanoparticles (AgNP) can improve the physical properties of GO. The incorporation of different nanoparticles on GO or graphene has been achieved in several ways, using covalent, non-covalent and direct deposition.[9-11]

Therefore, understanding the importance of modifying the graphene morphology and composition, my work was focused on the application of techniques and procedures commonly used in the Scaiano's group to obtain carbon-based materials with specific properties.

8.2 Materials and Methods

8.2.1 Materials

Silver nitrate and $HAuCl_4 \cdot 3H_2O$ were purchased from Sigma Aldrich and used as received. Irgacure 2959 was a gift from BASF supplied by Dempsey Corporation Canada and it was recrystallized from ethyl acetate. Graphene oxide was synthesized at the ITQ (Institudo de Tecnologia Quimica) as part of our collaboration with the research group of Prof. Hermenegildo Garcia. GO was prepared according to the Hummers procedure.[13]

Each solution was prepared using Millipore water (resistivity 18.2 MΩ at 25°C).

8.2.2 Functionalization of graphene oxide sheets with silver nanoparticles (AgNP@GO)

For the one pot procedure, the experiment was performed adding I-2959 (2 mM) and $AgNO_3$ (2 mM) to 3.5 ml of a suspended solution of GO (1.5 mg of GO in 18 ml of Millipore water). The solution was purged under nitrogen for 30 min and irradiated for 10 min with a 16 lamps UVA photoreactor (Luzchem).

For the sequential procedure, I-2959 (2 mM) was initially added to 3.5 ml of the aqueous GO solution, described above. The mixture was purged under nitrogen for 30 min and irradiated for 10 min under the same conditions described for the one pot method.

Immediately after irradiation $AgNO_3$ (2 mM) was added in the dark.

The samples were analyzed using UV-Vis spectroscopy and scanning electron microscopy before and after irradiation and addition of each component.

8.3 Selective functionalization of graphene oxide with AgNP

The functionalization of graphene oxide with metal nanoparticles was obtained using a photochemical methodology and avoiding the use of any linker. To do so, the AgNP were prepared directly on the GO sheets by reduction of Ag^+ in the presence of GO, using I-2959 as a source of electrons. (see Scheme 8.1) This procedure leads to the formation of AgNP decorated GO (i.e., AgNP@GO).

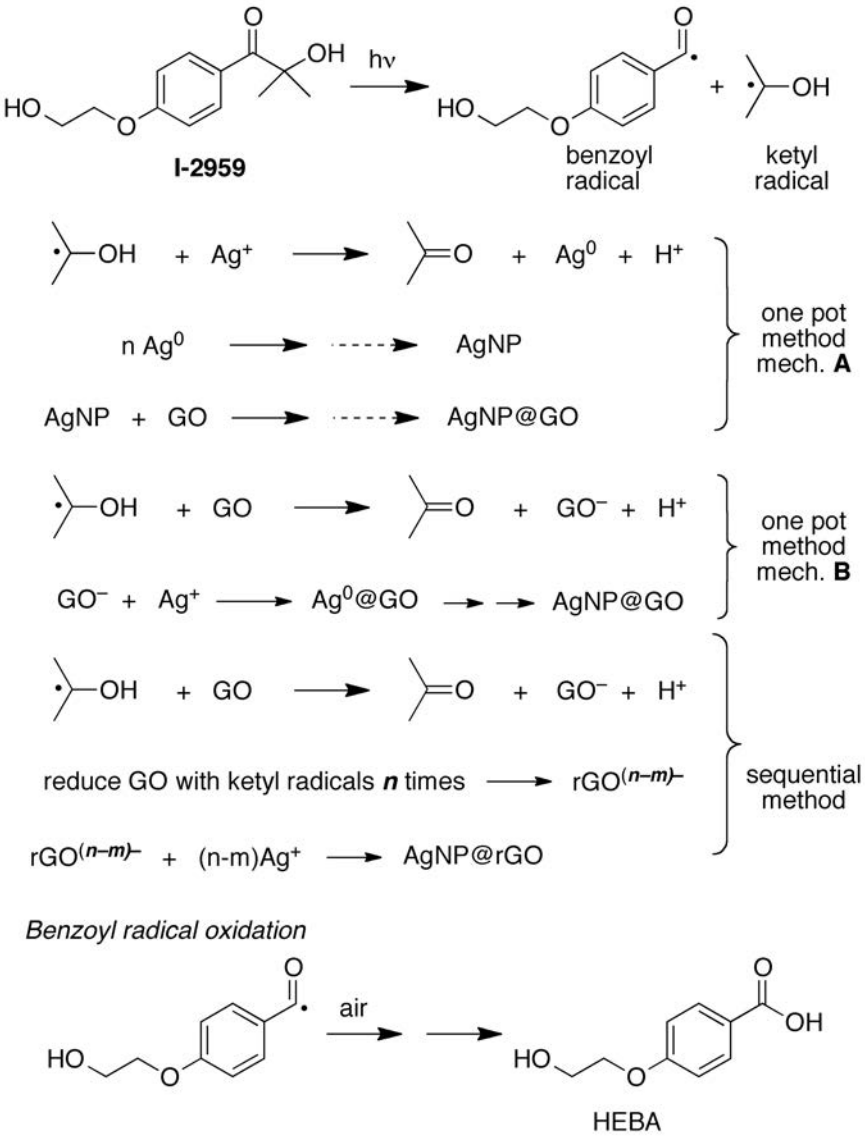

Scheme 8.1 Photochemical mechanisms for the formation of AgNP@GO and AgNP@rGO.

The reaction can be performed in either "one pot approach", which means that all the compounds ($AgNO_3$, GO and I-2959) are present from the beginning, or sequentially, which consist in irradiating just GO and I-2959 and adding afterwards $AgNO_3$. In other words, during the sequential procedure electrons are delivered to GO where they are stored and Ag^+ (or $AgNO_3$) is added right after irradiation, following the photodecomposition of I-2959. There is literature evidence for the accumulation of electrons in GO.[14] In the sequential method the addition of $AgNO_3$ is done immediately

following the irradiation of the GO and I-2959 solution; after this addition, the solution assumes the same color we obtained using the one pot method, where the solution presents a more intense tint after irradiation (see insert Figure 8.1). In both cases the reducing species is the $(CH_3)_2C^{\bullet}OH$ radical (ketyl radical) produced upon photodecomposition of I-2959 under UVA irradiation according to the mechanism of Scheme 8.1.[15] To our surprise, this technique leads to some GO sheets heavily occupied by AgNP, while others remain as vacant GO sheets. Figure 8.1 shows the UV-Vis spectra recorded before and after 10 min UVA irradiation following the one pot procedure. After irradiation the formation of the characteristic surface plasmon band of AgNP is evident. No changes in the UV absorption were noticed after days.

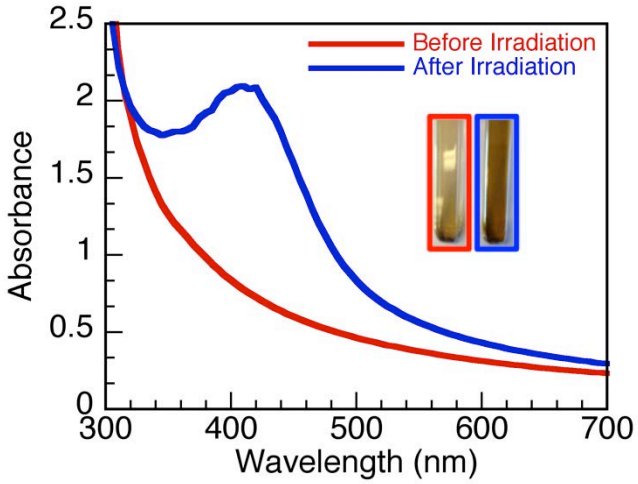

Figure 8.1 UV-Vis absorption spectra of GO, $AgNO_3$ and I-2959 solution before irradiation (red trace) and after 10 min UVA irradiation (blue trace). Insert: Pictures of the solution before and after irradiation.

The mechanism of Scheme 8.1 shows ketyl radicals reaction exclusively with Ag^+ in the one pot method mechanism A, while in the case of the sequential method ketyl radicals transfer the electron to GO. Those electrons are partially stored (n-m) and in part used to reduce GO (m). The need for a second mechanism (B) in the one pot method will become apparent later on, and relates to the fact that spectral evidence is different for the one pot and sequential methods. In the sequential method we label partially reduced GO as rGO. The experiment does not yield the relative values of "m" and "n", but it is clear

that "m" cannot be zero since there are differences between the AgNP decorated materials produced by both methods. The condition n=m is also impossible, given that many electrons lead to Ag^+ reduction. Given the efficient formation of AgNP, we believe that n>>m applies, i.e., most electrons are stored, rather than used to reduce GO in the time scale of this experiment.

The most striking observation in these experiments is that AgNP extensively populates some GO sheets, whereas others remain totally devoid of AgNP. This is true of both, the one-pot and the sequential methodology, and is illustrated in Figure 8.2. It is remarkable that electrons would favor deposition in GO sheets that have already been the subject of significant reaction with ketyl radicals (see Scheme 8.1). We assume that the initial electron deposition is a stochastic process with no real preference for a given sheet.

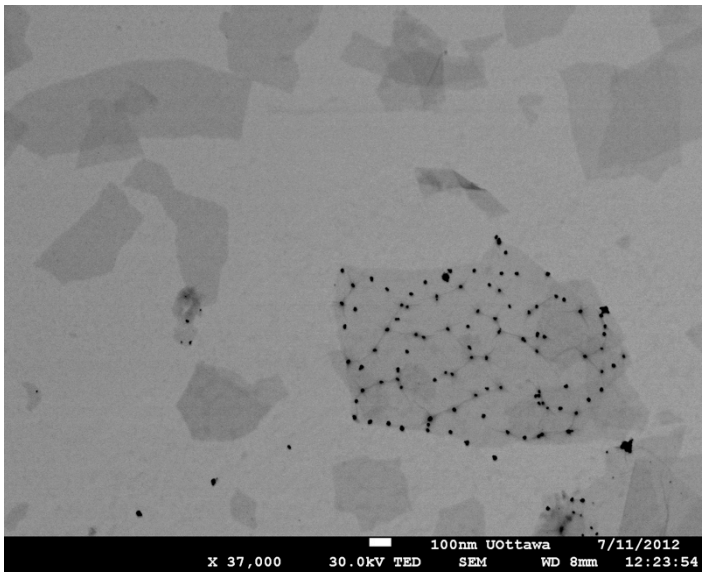

Figure 8.2 SEM picture of AgNP selectively deposited on GO using the sequential method. The scale bar is 100 nm.

We may ask why electrons would prefer to home on GO sheets that are already negatively charged. Further, if some of the electrons have already been used to reduce GO, then, these partially reduced sheets will not be as good as electron acceptors as the original GO sheets.

We propose that reaction of ketyl radicals with GO provides another example of proton coupled electron transfer (PCeT).[16] In a recent publication from our group it has been proposed that reduction of metal ions by ketyl radicals (as in the reaction with Ag^+ in Scheme 1) should be interpreted as a case of multisite PCeT.[17] Thus, the electron is only delivered if and when the proton has a home. As an example, ketyl radicals are very sluggish reducing Ag^+ in toluene or THF, but the reaction occurs efficiently upon addition of traces of amines, as these readily accept the proton.[18] In the case of GO the electron transfer cannot be strictly described as multisite, but rather, the electron simply follows the proton, that shows a preference for negatively charged surfaces. Thus, as GO gets charged negatively it becomes an increasingly better "home" for the protons and, as a result the site where the electrons from the ketyl radicals are deposited. In other words, in this example of PCeT it is the proton that controls the transfer of electrons and the reaction kinetics, even if it is likely that ultimately some of the protons simply dissociate from GO and be stabilized in water. There is precedent in the literature for examples where proton transfer controls the kinetics.[19]

One may ask if water is not enough to stabilize the ketyl radical in aqueous media. Of course, the radical will be hydrogen bonded in this media, but transfer of an electron also requires the electron acceptor, i.e., the GO sheets. The unusual preference for pre-charged sheets suggests that delivery of the proton, or at least anchoring the ketyl radical at the charged GO sheet, is rate controlling. It is also unusual that 'empty' GO sheets are generally totally unoccupied. It is possible that the first few electrons received by GO sheets are used to reduce the most active sites in GO and thus not available as electron storage; this would effectively create a switch or threshold below which the GO sheet is not negatively charged and thus some tolerance for receiving electrons, yet not yielding AgNP.

We note that the pattern of selective deposition is also observed in the one pot method. We find that it would be hard to explain how this occurs if mechanism A (Scheme 8.1) was dominant, as deposition would occur once AgNP have already formed. Instead, we believe that mechanism B is favored. Of course, these are competitive processes and the fact that one is favored does not imply that other reactions are totally prevented.

In order to determine how many available electrons (i.e., n-m in Scheme 8.1) could be stored by GO, we selected a representative image obtained by the sequential method. This particular sheet of AgNP@GO is shown in Figure 8.3, where we have selected a different image than in Figure 8.2, to illustrate how general the phenomenon is.

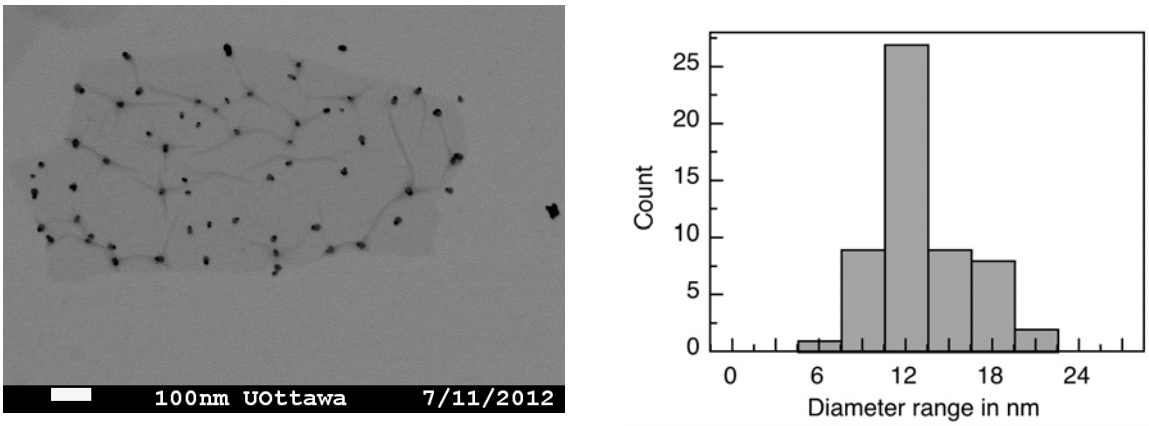

Figure 8.3 SEM image of AgNP@rGO prepared by the sequential method. Average particle size is 12.7 ± 3.2 nm; image analysis was performed on 56 AgNP on the surface.

The surface of the GO sheet (or more correctly rGO) is 5.14 x 10^5 nm^2. Image analysis of the 56 AgNP detectable on its surface yields a total volume for metallic Ag of 71980 nm^3. Assuming the same density as for bulk metallic silver, this yields 4.22 x 10^5 silver atoms. If we assume that each Ag^+ consumed one electron, this is also the number of electron initially stored in rGO and available for Ag^+ reduction. If the electrons are stored in the rGO surface, this corresponds to one electron per 1.22 nm^2; this is likely to be the case, as assuming that storage occurs on the perimeter would yield 162 electrons per nm.

8.4 AgNP@GO *vs.* AuNP@GO

In order to establish if the selective functionalization of GO was or not dependent on the metal ion used, we apply the same procedure to functionalize GO sheets with AuNP. Also in this case, the UV-Vis spectra obtained before and after irradiation showed the successful formation of AuNP (Figure 8.4), however, we could not see the same

selective behavior observed in the case of AgNP functionalized GO, as demonstrated by SEM analysis. (Figure 8.4, right)

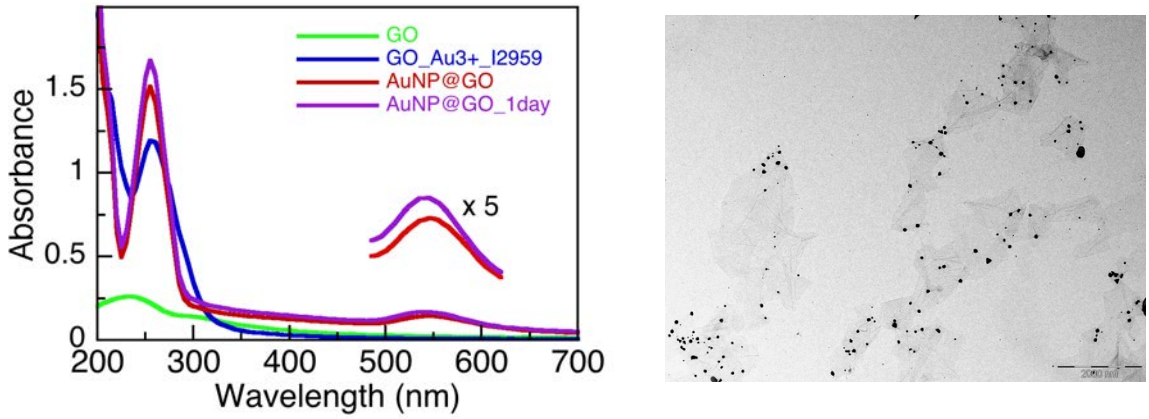

Figure 8.4 (left) Uv-Vis absorption of: GO solution (green trace); GO, $HAuCl_4$ and I-2959 solution before irradiation (blue trace); GO, $HAuCl_4$ and I-2959 solution after 30 min UVA irradiation (red trace); GO, $HAuCl_4$ and I-2959 solution after 30 min UVA irradiation recorded after 1 day (purple trace); (right) Representative SEM picture of AuNP@GO solution.

In the case of AuNP@GO, indeed, we noticed a non-selective deposition of AuNP on all the GO sheets, which appears to be consistent if we employ a "one-pot" or a "sequential" procedure, as reported in the previous section. The most probable reason of these different results between the two metals is probably imputable to the need of a higher number of electrons in the case of the AuNP formation, compared to the Ag^+ reduction (Scheme 8.2). In the case of silver, indeed only one electron is required to reduced Ag^+ to Ag^0 and therefore, as soon as the Ag^+ encounters the electron on the GO surface, it is reduced to Ag^0. On the other hand, the formation of AuNP, is preceded by a sequence of Au^{3+} disproportionation, which can happen on all the GO sheets indiscriminately, as schematically reported in Scheme 8.2.

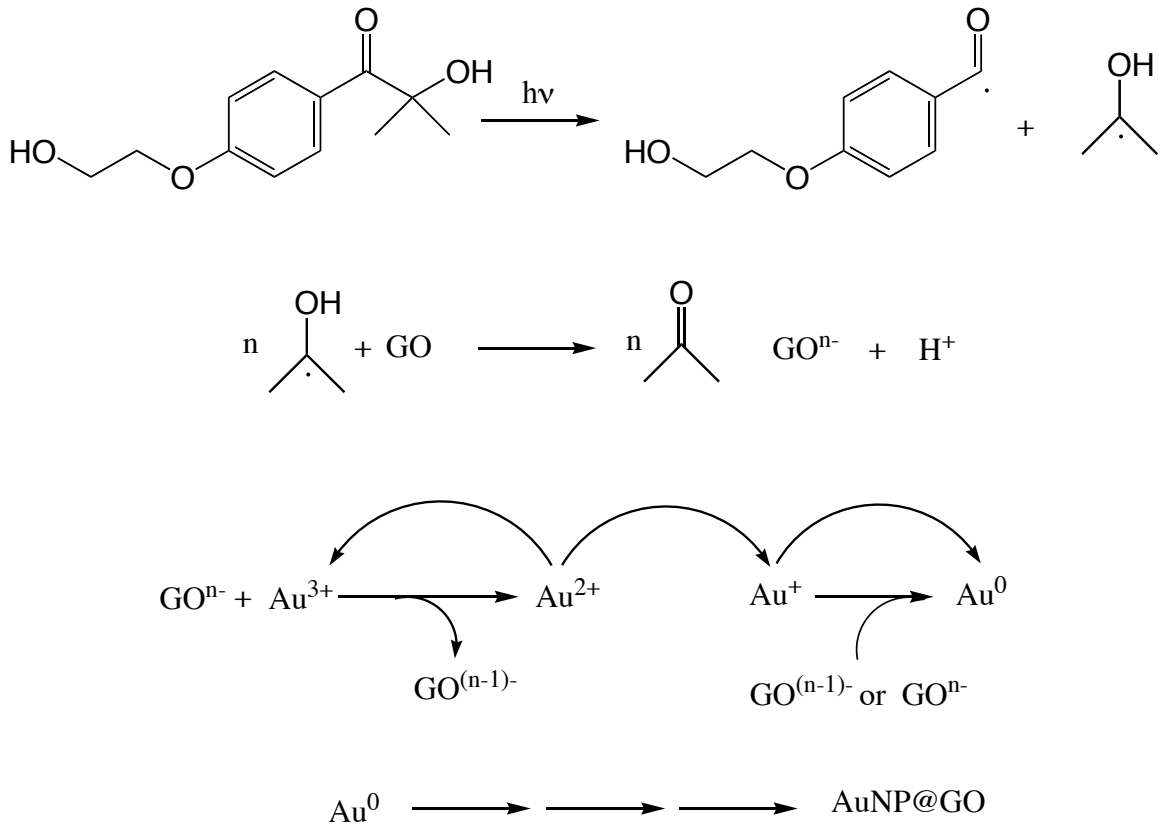

Scheme 8.2 Photochemical mechanisms for the formation of AuNP@GO using I-2959. Species shown as Au^{n+} for convenience, note that all Au species are negatively charged, *i.e.* Au^{3+} is $AuCl_3^-$.

The number of electrons available on the surface of a certain GO sheet may not be sufficient to reduce Au^{3+} to Au^0, thus the complete reduction may occur with the assistance of other GO sheets, that provide the remaining electrons required.

In addition, while the Ag^+ is a positive ion, and therefore it has affinity for the negatively charged GO surface, all the intermediate ions derived from $AuCl_4^-$ are negatively charged. Thus, it is probable that during the gold reduction process, the intermediate ions diffuse to the solution as a consequence of their repulsion for the GO surface. This effect explains the random deposition of the AuNP compared to the AgNP on GO.

The explanation proposed may need to be extended to other possible factors that could also play a rule, however the remaining finding is that AgNP and AuNP present a different functionalization tendency when reduced in presence of GO.

In conclusion, whether described as autocatalytic or cooperative, in the case of AgNP@GO, it is clear that electron deposition on GO follows non-random dynamics, with a preference for deposition in already electron-rich GO sheets. This phenomenon can be explained readily as a PCeT process, where the proton plays a determining and guiding role in the electron delivery. As a result we obtain a GO archipelago, in which some islands are heavily populated by AgNP, with some preference for shore locations, while others remain uninhabited.

8.5 Summary

The project presented in this chapter started as side project of my research, however the unique characteristics that carbon-based materials increasingly became part of my interests. We discovered a selective functionalization of graphene oxide with AgNP in contrast with the indiscriminate functionalization of AuNP. This observation was rationalized considering a PCeT transfer process and the distinctive behaviors of the two metals were attributed to the different number of electrons required for their reduction to the elemental state. In addition, a facile and green structural modification of reduced graphene oxide using laser ablation will be presented in the following chapter. The possible application of those modified graphene oxide compounds are countless.

In conclusion, chemically modified graphene presents incredible potential for a wide range of uses and the different behaviors that this material possess according to the morphology or the composition makes this range of application even broader.

8.6 References

(1) (a) Geim, A. K.; Novoselov, K. S. The Rise of Graphene. *Nature Materials,* **2007**, *6*, 183-191; (b) Novoselov, K. S.; Geim, A. K.; Morozov, S. V.; Jiang, D.; Zhang, Y.; Dubonos, S. V.; Grigorieva, I. V.; Firsov, A. A. Electric Field Effect in Atomically Thin Carbon Films. *Science,* **2004**, *306*, 666-669.

(2) Gomes, K. K.; Mar, W.; Ko, W.; Guinea, F.; Manoharan, H. C. Designer Dirac Fermions and Topological Phases in Molecular Graphene. *Nature,* **2012** 483, 306-310.

(3) (a) Ghosh, S.; Calizo, I.; Teweldebrhan, D.; Pokatilov, E. P.; Nika, D. L.; Balandin, A. A.; Bao, W.; Miao, F.; Lau, C. N. Extremely High Thermal Conductivity in Graphene: Prospects for Thermal Management Application in Nanoelectronic Circuits. *Applied Physics Letters,* **2008**, 92, 151911. (b) Balandin, A. A.; Ghosh, S.; Wenzhong, B.; Calizo, I.; Teweldebrhan, D.; Miao, F.; Lau, C. N. Superior Thermal Conductivity of Single Layer Graphene. *Nano Letters,* **2008**, 8, 902_907 (c) Chen, S.; Wu, Q.; Mishra, C.; Kang, J.; Zhang, H.; Cho, K.; Cai, W.; Balandin, A. A.; Ruoff, R.S. Thermal Conductivity of Isotopically Modified Graphene. *Nature Materials,* **2012**, 11, 203.

(4) Rao, C. N. R.; Sood, A. K. Graphene: Synthesis, Properties and Phenomena. *John Wiley & Sons,* **2013.**

(5) Mukherjee, R.; Thomas, A. V.; Krishnamurthy, A.; Koratkar, N. Photothermally Reduced Graphene as High-Power Anodes for Lithium-Ion Batteries. *ACS Nano*, **2012**, 6, 9, 7867-7878.

(6) Ramasse, Q. M.; Zan, R.; Bangert, U.; Boukhvalov, D. W.; Son, Y.-W.; Novoselov, Y.-W. Direct Experimental Evidence of Metal-Mediated Etching of Suspended Graphene. *ACS Nano,* **2012***,* 6, 5, 4063-4071.

(7) (a) Shen, J.; Yan, B.; Shi, M.; Ma, H.; Li, N.; Ye, M. One Step Hydrothermal Synthesis of TiO_2-Reduced Graphene Oxide Sheets. *Journal of Material Chemistry*, **2011**, 21, 3415. (b) Zhou, Y.; Bao, Q.; Tang, L. A. L.; Zhong, Y.; Loh, K. P. Hydrothermal Dehydration for the "Green" Reduction of Exfoliated Graphene Oxide to Graphene and Demonstration of Tunable Optical Limiting Properties. *Chemistry of Materials,* **2009**, 21, 2950–2956.

(8) Koinuma, M.; Ogata, C.; Kamei, Y.; Hatakeyama, K.; Tateishi, H.; Watanabe, Y.;Taniguchi, T.; Gezuhara, K.; Hayami, S.; Funatsu, A.; Sakata, M.; Kuwahara, Y.; Kurihara, S.; Matsumoto, Y. Photochemical Engineering of Graphene Oxide Nanosheets. *Journal of Physical Chemistry C*, **2012**, 116, 19822−19827.

(9) Guo, S.; Dong, S. Graphene Nanosheet: Synthesis, Molecular Engineering, Thin Film, Hybrids, and Energy and Analytical Applications. *Chemical Society Reviews,* **2011**, *40*, 2644-2672.

(10) Machado, B. F.; Serp, P., Graphene-Based Materials for Catalysis. *Catalysis Science and Technology,* **2012**, *2*, 54-75.

(11) Tjoa, V.; Jun, W.; Dravid, V.; Mhaisalkar, S.; Mathews, N. Hybrid Graphene–Metal Nanoparticle Systems: Electronic Properties and Gas Interaction. *Journal of Material Chemistry,* **2011**, *21*, 15593-15599.

(12) Dreyer, D. R.; Park, S.; Bielawski, C. W.; Ruoff, R. S. The Chemistry of Graphene Oxide. *Chemical Society Review,* **2010**, *39*, 228-240.

(13) Hummers, W. S. Jr.; Offerman, R. E. Preparation of Graphitic Oxide. *Journal of American Chemical Society*, **1958**, *80*, 6, 1339–1339.

(14) Krishnamurthy, S.; Lightcap, I. V.; Kamat, P. V. Electron Transfer Between Methyl Viologen Radicals and Graphene Oxide: Reduction, Electron Storage and Discharge. *Journal of Photochemistry and Photobiology A: Chemistry,* **2011**, *221*, 214-219.

(16) (a) McGilvray, K. L.; Decan, M. R.; Wang, D.; Scaiano, J. C. Facile Photochemical Synthesis of Unprotected Aqueous Gold Nanoparticles. *Journal of American Chemical Society*, **2006**, *128*, 15980-15981. (b) Jockusch, S.; Landis, M. S.; Freiermuth, B.; Turro, N. J. Photochemistry and Photophysics of α-Hydroxy Ketones. *Macromolecules,* **2001**, *34*, 1619-1626.

(17) (a) Mayer, J. M. Understanding Hydrogen Atom Transfer: from Bond Strengths to Marcus Theory. *Accounts of Chemical Research,* **2011**, *44*, 36-46. (b) Mayer, J. M. Simple Marcus-Theory-Type Model for Hydrogen-Atom Transfer/Proton-Coupled Electron Transfer. *Journal of Physical Chemistry Letters,* **2011**, *2*, 1481-1489. (c) Huynh, M. H. V.; Mayer, J. M. Proton-Coupled Electron Transfer. *Chemical Reviews,* **2007**, *107*, 5004-5064. (d) Hammes-Schiffer, S. Theory of Proton-Coupled Electron Transfer in Energy Conversion Processes. *Accounts of Chemical Research,* **2009**, *42*, 1881-1889.

(18) Scaiano, J. C.; Stamplecoskie, K. G.; Hallett-Tapley, G. L. Photochemical Norrish Type I Reaction as a Tool for Metal Nanoparticle Synthesis: Importance of Proton Coupled Electron Transfer. *Chemical Communications,* **2012**, *48*, 4798-4808.

(19) (a) Maretti, L.; Billone, P. S.; Liu, Y.; Scaiano, J. C. Facile Photochemical Synthesis and Characterization of Highly Fluorescent Silver Nanoparticles. *Journal of American Chemical Society*, **2009**, 131, 13972-13980. (b) Stamplecoskie, K. G.; Scaiano, J. C. Silver as an Example of the Applications of Photochemistry to the Synthesis and Uses of Nanomaterials. *Photochemistry and*

Photobiology, **2012**, 88, 762-768. (c) Stamplecoskie, K. G.; Scaiano, J. C. Kinetics of the Formation of Silver Dimers (Ag2): Early Stages in the Formation of Silver Nanoparticles, *Journal of American Chemical Society*, **2011**, 133, 3913-3920.

Chapter 9

Summary, Future Directions and Conclusion

9.1 Summary

Nanotechnology represents nowadays a promising area, offering the potential to overcome the limitations encountered in several fields of application. The use of nanomaterials in everyday life is evermore increasing and indeed, even without knowing, we are surrounded by objects containing nanomaterials. To cite a few, nanoparticles of hydroxyl apatite calcium-based mineral have been used as components in toothpaste, for remineralization of the tooth surface.[1] Another example is a nano-clay composite employed for the fabrication of tennis balls, making them more airtight and allowing them to last longer on the courts.[2] Moreover, silver nanoparticles have been used to coat band-aid in order to help the wound healing faster due to their antimicrobial properties.[3] Even though the examples reported can be considered successful applications of nanomaterials, there is still "*plenty of room in the bottom*" to be discovered.[4]

This thesis reports just the tip of the iceberg in terms of production and possible uses of nanomaterials, however, few interesting achievements have been accomplished and good applicable results have derived from this study.

First of all, elemental nanoparticles synthesis and modification, throughout a facile procedure, have been reported. In all the methodologies employed light played a predominant role. From the synthesis of Au/Ag core-shell to the modification of graphene sheets, our photochemical methods showed high morphological and dimension control of the particles formed. The major advantage of the use of light derives from the possibility to interrupt the process with a simple switch off of the light source. This aspect can appear trivial, however it shows its importance when compared to chemical methods, in which no easy control of the synthesis progress can be achieved. For instance, it has been shown that the size and elemental ratio of Ag/Au core-shells are directly dependent on the irradiance dose.[5]

A consistent portion of my work was focused on the study and application of the plasmonic properties of metal nanoparticles. Visible light was used to excite the SPR of AuNP and AgNP, a characteristic that makes this process suitable for a wide number of applications. The visible light indeed is cheaper and less harmful compared to other portions of the electromagnetic spectrum. Moreover, the possibility to convert the light-to-heat was investigated, starting from the identification of the temperatures obtainable after plasmon irradiation. For this purpose, the dissociation of dicumyl peroxide, performed irradiating spherical AuNP at 530 nm, was chosen as a model reaction. This molecule acted as a "molecular thermometer"; in such a way that, knowing the required thermodynamic parameters and applying the Arrhenius equation, temperatures values close to 500ºC at the nanoparticles surface have been obtained.[6] This indicative temperature represented a starting point for the selection of thermal processes that can be performed irradiating metal nanoparticles.

Furthermore, practical applications of the SPR of metal nanoparticles were also explored, ranging from catalysis to biochemistry.

Resazurin reduction mediated by plasmon irradiation of spherical AuNP was studied measuring the emission of the resulting product, resorufin. For this reaction LED and laser drop irradiations were employed and compared to conventional thermal methods (microwaves, thermal bath). As a result, laser drop and LED showed the best performances in terms of conversion per time. The laser drop in particular gave a quantitative conversion just after a single shot, in a time range of nanoseconds. LED irradiation otherwise represents a convenient alternative in terms of usability and cost.[7]

To further discover the potential of metal nanoparticles, a successful use for a lithographic application was investigated. In this project, the irradiation of AgNP-functionalized quartz slides triggered the thermal polymerization of caprolactam into nylon-6. Once more the use of light was paramount, in this case not only for the formation of the polymer, but also for the synthesis of AgNP in selected portions of the slide. An ordered distribution of the polymer features was obtained thanks to the localization of the heat released after plasmon irradiation. This result represents another example of how the light-to-heat conversion can favor a process that requires high precision at low dimension scale.[8] In addition, this work set the stage for the successful synthesis of self-assembled nanolasers, a project just published by a former graduate student in the Scaiano group.[9]

In addition, the melting of a ds-DNA sequence was performed after irradiation of spherical AuNP attached to one of the strands of the ds-DNA. In this project a specific design of the system was realized to be able to observe the evolution of the process. First of all, each strand of the ds-DNA was marked with a dye in order to keep track of their positions. With this design, when the DNA is in its double stranded conformation, the emission coming from the dye-ss-DNA, not directly linked to AuNP, is quenched by the particles. However, after irradiation and melting of the DNA, the thermoplasmonic release of the labeled ss-DNA can be monitored *in situ* by measuring the emission of the dye. Fluorescence microscopy techniques have been employed for this purpose.[10]

Finally, the modification and use of carbon-based material has been also object of my study, with the aim of extending my knowledge of the "nanoworld". Successful

functionalization of graphene oxide with AuNP and AgNP was performed employing a photochemical procedure. Surprisingly, a different behavior was observed for the two metal nanoparticles, with AgNP being particularly selective in the functionalization of specific graphene oxide sheets, while AuNP showing no selectivity in the deposition. A PCeT was suggested as mechanism occurring in the case of AgNP. Moreover, the diverse tendency of functionalization, observed for the two metals, was attributed to the different number of electron required to reduce silver and gold.[11]

9.2 Future directions

9.2.1 Metal nanoparticles

Due to the variety of applications described, several future directions can be explored.

The optical properties of metal nanoparticles can be used to increase the range of light absorbed by common photocatalysts, extending their absorption to the visible range.[12] In this prospective, during my PhD I have been involved in several projects where the functionalization of semiconductors, such as TiO_2, n-ZnO and Nb_2O_5 with metal nanoparticles resulted in an enhancement of the catalytic performances of those materials. The materials were prepared using the laser drop technique, a process in which AuNP were ablated prior to addition to an aqueous dispersion of the semiconductor. SEM pictures of the resulting materials are reported in Figure 9.1.

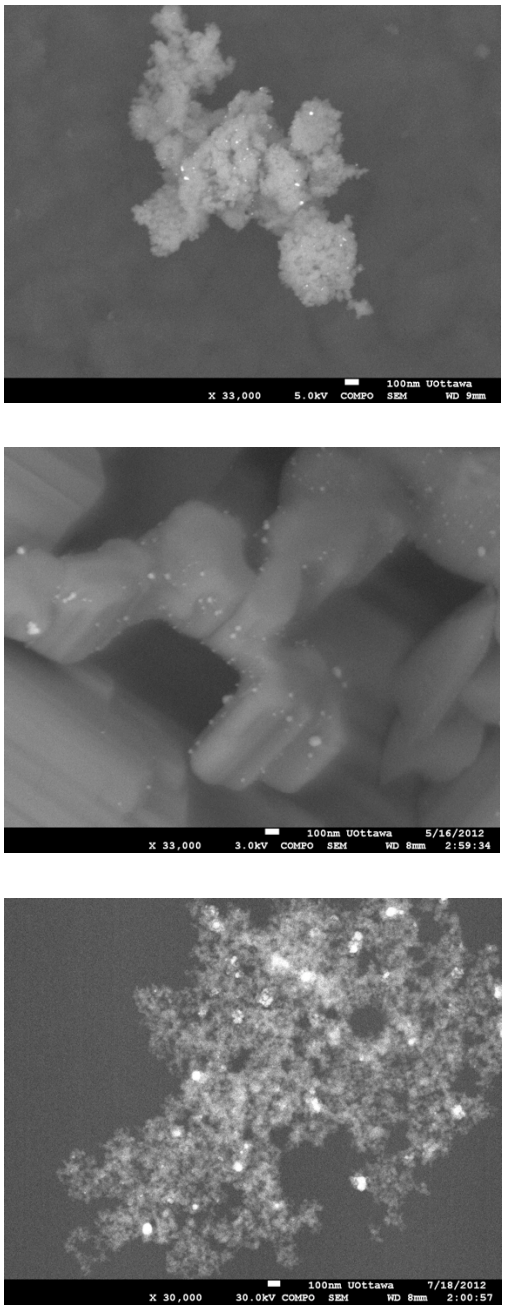

Figure 9.1 SEM pictures of the AuNP@nZnO (top), AuNP@Nb_2O_5 (center) and AuNP@TiO_2 (bottom).

The catalysts obtained were then employed for the catalysis of several reactions, such as oxidations, reductions and condensations, to name a few.[13,14] The combination of solid semiconductors with colloidal solutions of AuNP results in a catalyst that possesses the

properties of both materials, in such a way that, not only an extension of the absorption range is obtained, but also, a more convenient way to separate the nanoparticles from the reaction can be achieved, the latter advantage derives from the use of an heterogeneous support. These considerations are particularly interesting, since the composite formed result very efficient and suitable for green applications.

A prolific field where the properties of metal nanoparticles can play a predominant role is in thermal polymerization processes. A possible direction to explore in this prospective is the combination of metal nanoparticles with thermoresponsive polymers. This class of compounds assumes a different physical state in response to a thermal stimulus. A change from liquid to solid can occur increasing or decreasing the temperature around the polymer. Indeed, thermo-responsive polymers, such as poly(N-isopropylacrylamide) (PNIPAM) or poly(N,N-diethylacrylamide) (PDEAM), can undergo to a phase change if the temperature is increased above the lower critical solution temperature (LCST). Other polymers, such as acrylamide (PAAm), have a upper critical solution temperature (UCST) above which they can be converted in free-flowing liquids (Figure 9.2).[15,16]

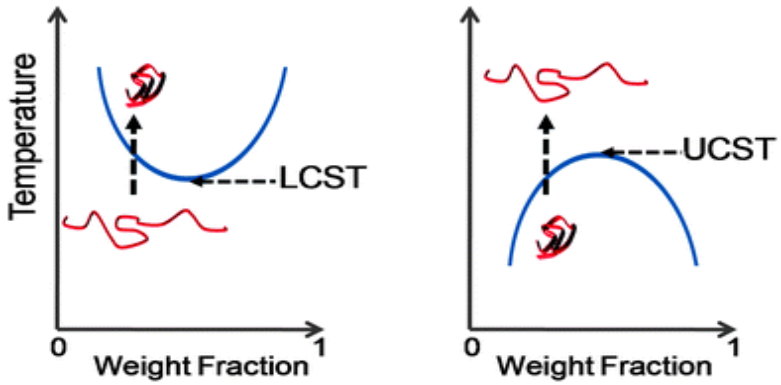

Figure 9.2 Plot reporting the temperature weight fraction for a LCST polymer (left) and a UCST polymer (right).[16]

Several application of these composites can be forecasted, one of them being the use as materials for art conservation and restoration. This topic was the object of my research

proposal and it described as the localized heat released from metal nanoparticles could be used to get a response of a polymer employed as a cleaning material, allowing an easy removal of the polymer and avoiding the use of harmful solvents.

Bio-application of nanomaterials also represents a field to continue to explore. From drug delivery to antimicrobial properties, nanoparticles can play a relevant role in several biological processes. Our DNA melting project indeed anticipates the possible application of metal nanoparticles SPB properties in important laboratory applications such as polymerase chain reaction process. Moreover, our synthesis of Ag/Au core-shell particles was aimed to the combination of silver and gold properties, an aspect that may result particularly interesting for different applications and not last for biological uses. In fact, by looking at their respective visible spectra, we can notice that, by functionalizing a gold nanoparticle with an external silver layer, a core shell structure, able to absorb from 400 nm to 600 nm, can be obtain. In addition, Ag/Au core-shells in principle maintain the antimicrobial properties of silver and the photo-thermal properties of gold.[17] In this prospective, we decided to investigate the effect of Ag/Au core-shell, irradiated with visible light, in the growth of different classes of bacteria. Two gram positive cocci strains: *Staphylococcus aureus* ATTC 25923, *Staphylococcus epidermidis* SE19 and one gram negative bacillus strain: *Escherichia coli* CF073 were chosen as representative examples of the two large groups of bacteria strains. (Figure 9.3)

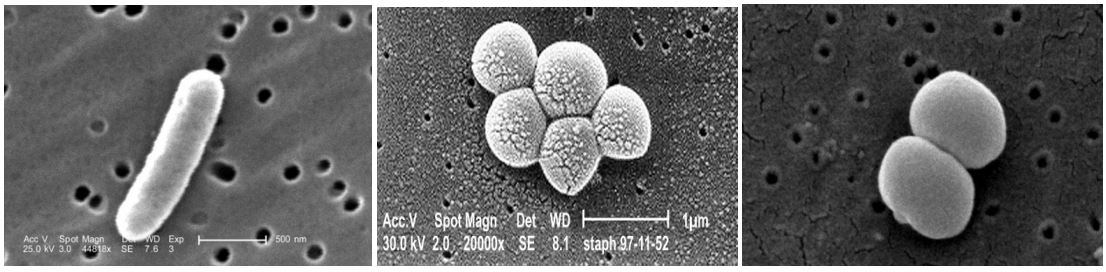

Figure 9.3 SEM pictures of: *Escherichia coli* (left), *Staphylococcus aureus* (center), *Staphylococcus epidermidis* (right).[18]

For the Ag/Au core-shells used in this project, citrate was replaced with other stabilizing agents such as LL-37, a small peptide from the cathelicidin family or, as a cheaper alternative, aspartame ($563.00/mg *vs.* $0.06/mg). (Figure 9.4)

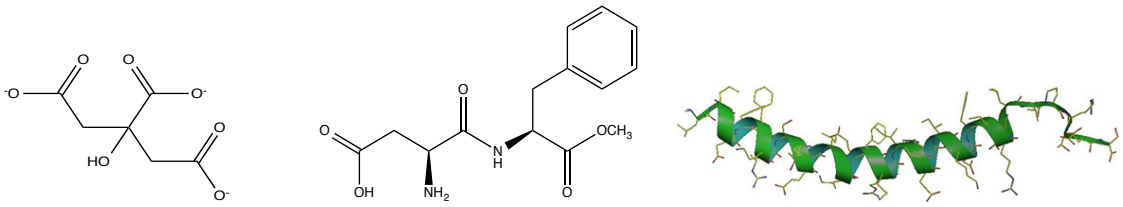

Figure 9.4 Molecular structures the stabilizing agents used: citrate (left), aspartame (center) and LL-37 protein (right).[19]

Bacteria incubation with different concentration of Ag/Au core-shells (from 13.75 μM to 0) was carried out for 18 h at 37ºC, keeping two identical plates under LED irradiation and in the dark respectively. LED irradiation was performed using a 530 nm panel customized by Luzchem and placed inside the incubator as shown in Figure 9.5.

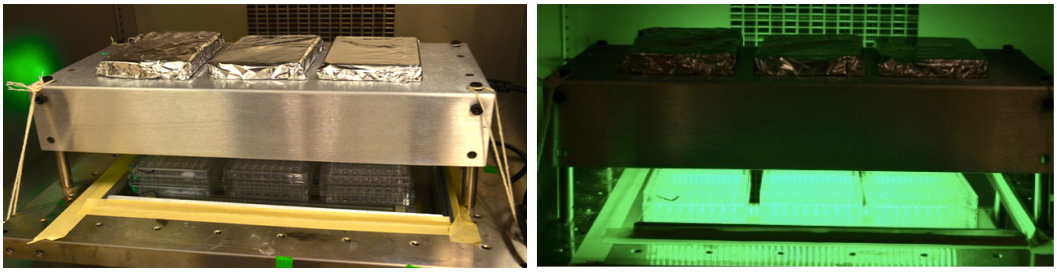

Figure 9.5 Pictures of the LED panel and set up used, before (left) and after (right) turning on the light. The well-plates to irradiate were placed on top of a mirror to maximize the light exposure. Parallel dark experiments were conducted wrapping identical well-plates with aluminum foil (shown on top of the LED panel). The system was disposed inside an incubator at 37ºC and keeping a constant agitation.

The absorbance at 620 nm, due to the light scattering produced by the microorganisms, was recorded as an indication of bacterial growth. (Figure 9.6)

The preliminary results obtained clearly indicate that in absence of light (black bars, Figure 9.6) the only antimicrobial effect is due to the known properties of AgNP. However, when 530 nm light is shined on the plate (green traces Figure 9.6) a lower minimum inhibitory concentration (MIC) of the material is required, suggesting a cooperative effect between gold and silver.

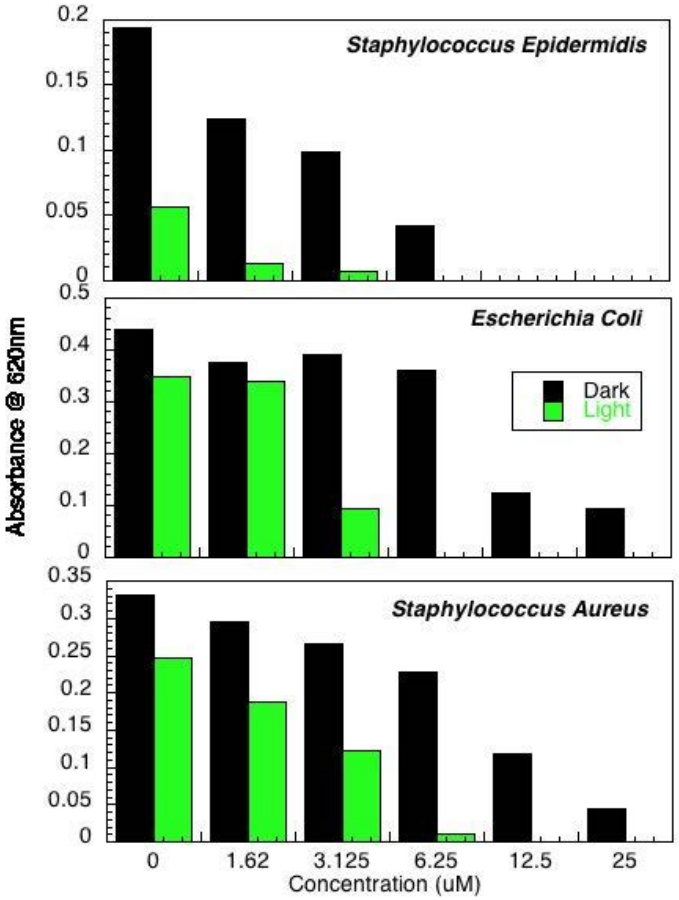

Figure 9.6 MIC results obtained incubating for 18 h the three bacterial strains: *Staphylococcus epidermidis* (top), *Escherichia coli* (center), *Staphylococcus aureus* (bottom) with aspartame@Ag/Au core-shells under irradiation (green bars) and in the dark (black bars).

Viability experiments remain to be carried out; nevertheless this represents another promising application of nanomaterials.

As shown in this last examples, different stabilizing agents can be used to achieve the desired purpose, moreover the versatility of the synthetic method used not only permit to vary the stabilizing agent used but, in principle, it can also be used for other metals reducible by ketyl radicals, extending in this way the properties of the materials produced.

9.2.2 Carbon-based materials

Several applications of carbon-based materials have emerged in the last years. A comprehensive description of all possible perspectives opened by the application of graphene base materials is the objects of several reviews.[20] In addition to the possibility of functionalizing graphene oxide with metal nanoparticles, we have preliminary explored the possibility of structurally modifying reduced graphene oxide (rGO) by laser irradiation.

In our attempt, different numbers of shots per drop were used to analyze the effect of a 532 nm beam on the rGO sheets, obtained by hydrazine reduction of graphene oxide. The solutions were collected after irradiation and analyzed. Figure 9.7 shows the change in color of the samples collected after irradiation. Increasing the number of shots per drop leads to a variation of the graphene solution color from dark black (initial solution) to clear grey (after 20 shots/drop).

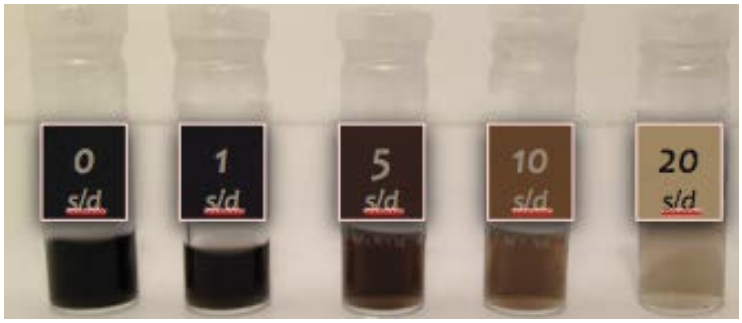

Figure 9.7 Graphene solutions before (left) and after laser irradiation (532 nm laser; 45 mJ; 1, 5, 10 and 20 shots per drop).

UV-visible absorption of the graphene solution before ablation showed an intense band

centered at 270 nm. After irradiation with just one shot per drop the absorbance started to decrease, until almost disappearing after 50 shots/drop. (Figure 9.8)

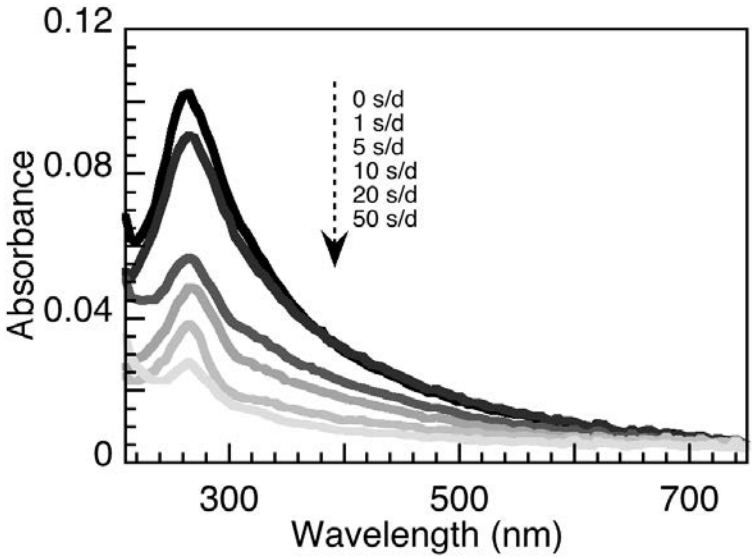

Figure 9.8 Uv-Vis spectra of graphene solutions recorded collecting the solutions after different amount of laser shots for each drop.

SEM picture of the samples before and after ablation were collected, showing a dramatic change in conformation of the graphene flakes. (Figure 9.9) Before laser irradiation the electron microscopy reveals the classical graphene sheet conformation (Figure 9.9, a), no particular shape is observed, other than possible overlapping of the planes. Just after one shot, the sample appears to have a spherical shape. (Figure 9.9, b) By increasing the number of shots per drop we observed a progressive decrease in the sizes of the graphene spherical structures, as shown in the SEM pictures sequence shown in Figure 9.9 (b-e).

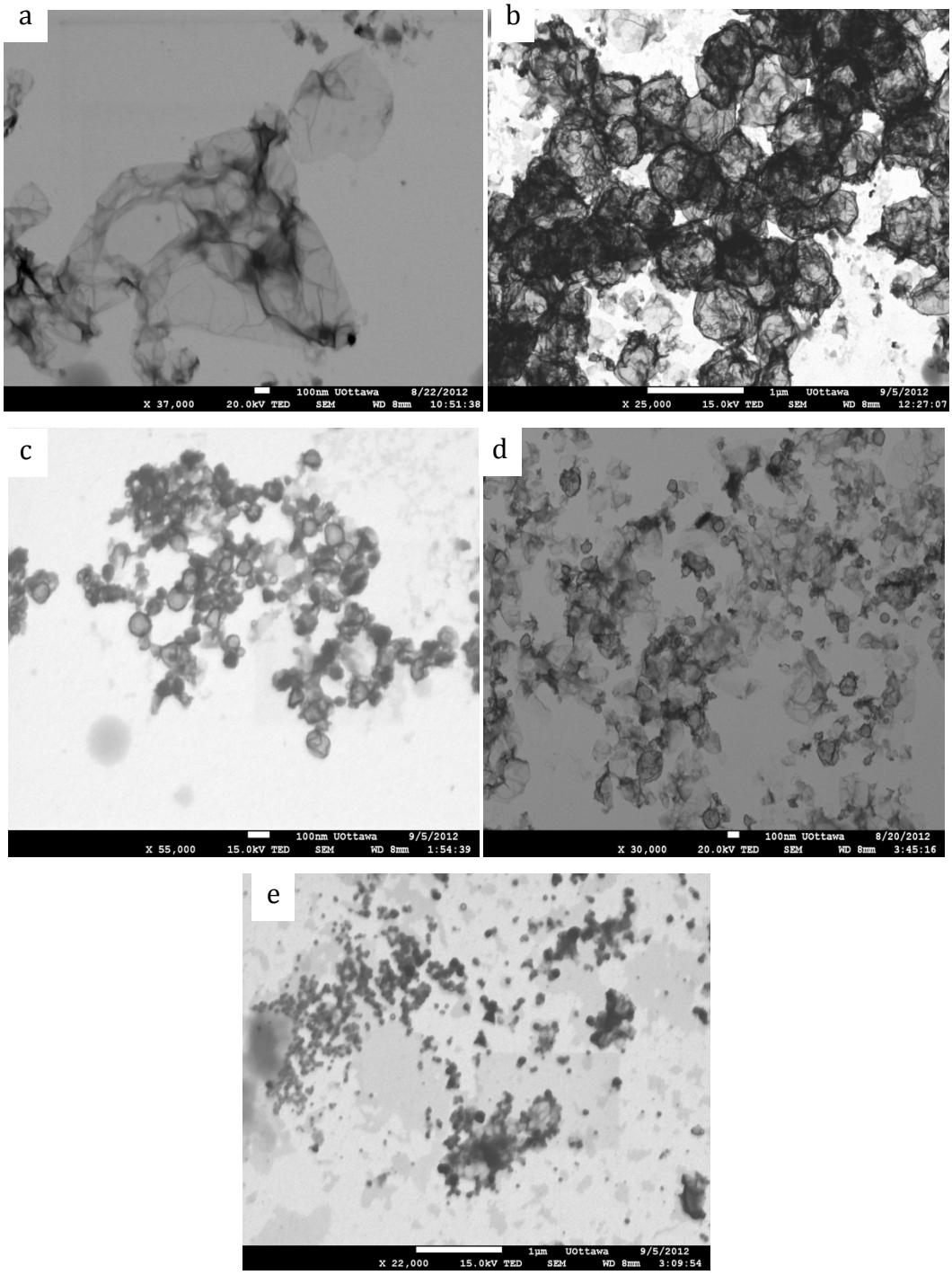

Figure 9.9 SEM pictures of graphene solutions before (a) and after 1, 5, 10, 20 shots per drop (b-e).

A high surface resolution SEM can be obtained by using the SEI mode. The pictures obtained confirm the conformational change of the graphene flakes to a spherical shape, highlighting the topography features (Figure 9.10).

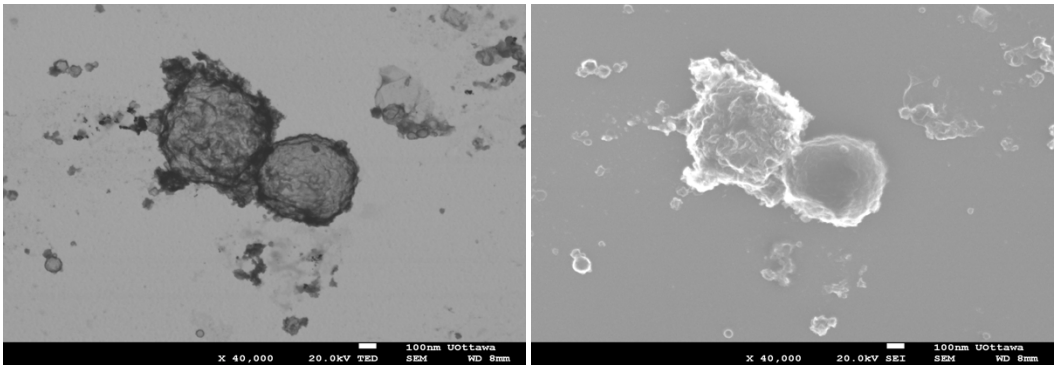

Figure 9.10 SEM images of the grephene flakes in TED (left) and SEI (right) modes.

Another indispensable tool in the graphene research is Raman spectroscopy; indeed it can furnish precious indication regarding the structure and the composition. Therefore, Raman spectra were recorded before irradiation and after different amount of shots/drop, showing a variation in the ratio between the G and D bands. The G-band is the primary mode in rGO and it represents the planar configuration sp^2 bonded carbon. The position of this band is often used to determine the rGO layer thickness, since as the layer thickness increases, the band position shifts to lower energy due to a softening of the bonds. The D-band is known as the defect band. It represents a ring mode from sp^2 carbon rings, and to be active the ring must be adjacent to a rGO edge or a defect.[21] Specifications of the Raman instrument used and analysis procedure are reported in Chapter 2, paragraph 2.2.3. In our results, the G band position remains the same even after laser ablation, however, the relative decrease of the D band indicates a reduction of the defects on the rGO conformation. In fact, before ablation the intensity of the two bands are comparable, while after 10 shots per drop the intensity of the G band increases compared to the D band, indicating that the structure is getting more ordered after irradiation. (Figure 9.11).

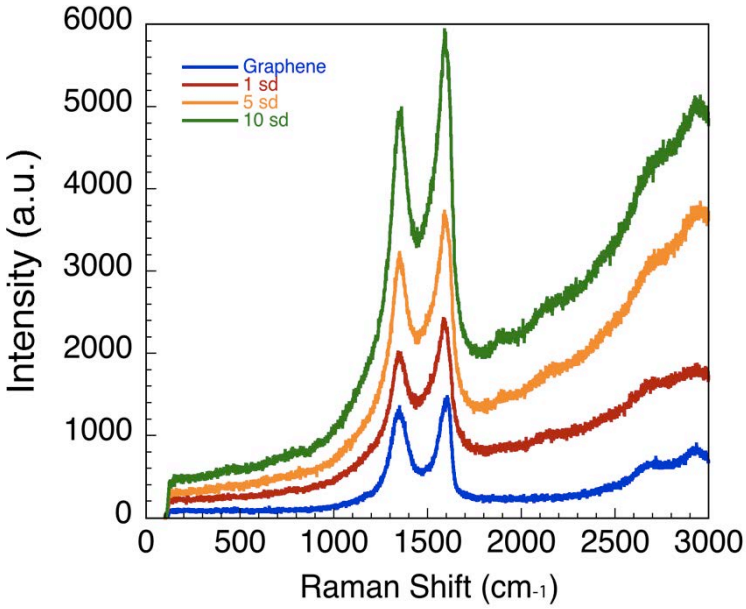

Figure 9.11 Raman spectra of the rGO solution after a different number of laser shots, obtained irradiating at 530 nm.

Additional information was obtained analyzing AFM images before and after laser irradiation. As shown in Figure 9.12 the structural variation of the rGO sample is in accordance with the SEM pictures. The sample presents plane features with several irregularities before any irradiation. After 20 shots per drop the sample appears spherical with features having higher height.

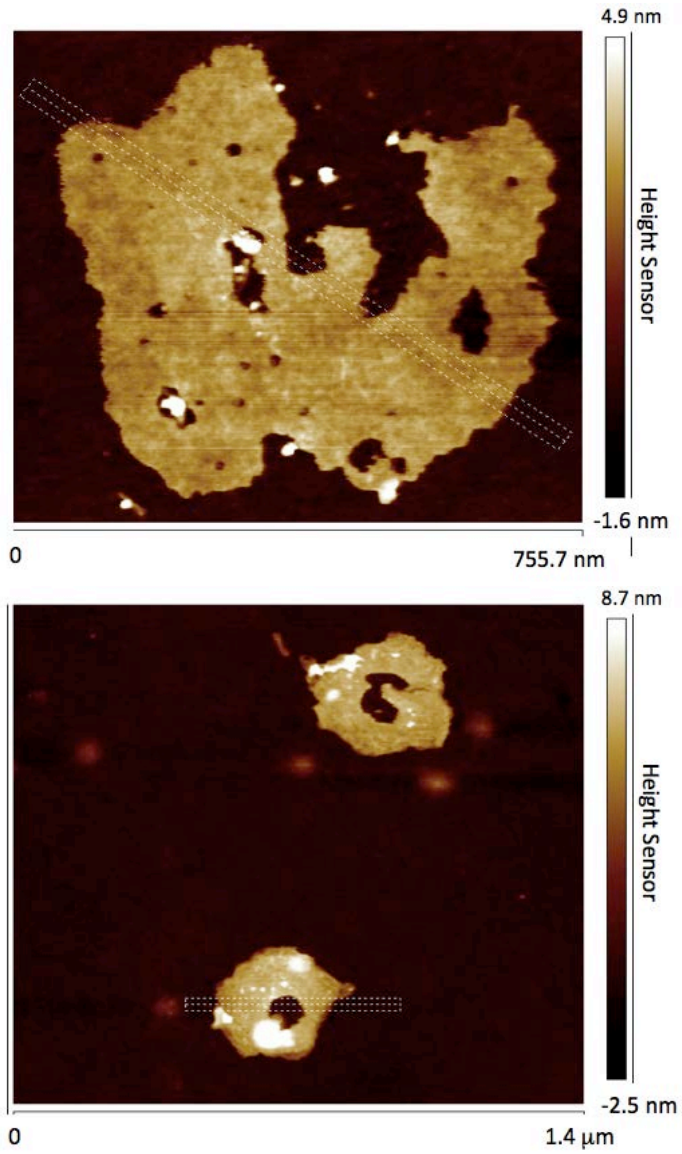

Figure 9.12 AFM images of the rGO solution before (top) and after 20 shots/drop 532 nm laser irradiation (bottom).

For comparison the same reduced graphene oxide solution was irradiated for 2 h using a quad of four 532 nm LED, no change in the absorbance nor in the rGO structure was observed by UV-Vis and SEM analysis respectively. This observation proved that laser irradiation is required to induce the changes in rGO morphology. However, the irradiation does not necessarily need to be performed on the small volume of a drop; indeed, the analysis of a rGO solution irradiated for 30 min in a 1 mm thin cuvette, keeping the irradiation wavelength and power constant (532 nm; 45 mJ), showed the

same morphological modification observed in the laser drop irradiation experiment (Figure 9.13). However, from the SEM pictures it is easy to notice how the cuvette irradiation leads to a more polydisperse sample compared to the results obtained using the laser drop system.

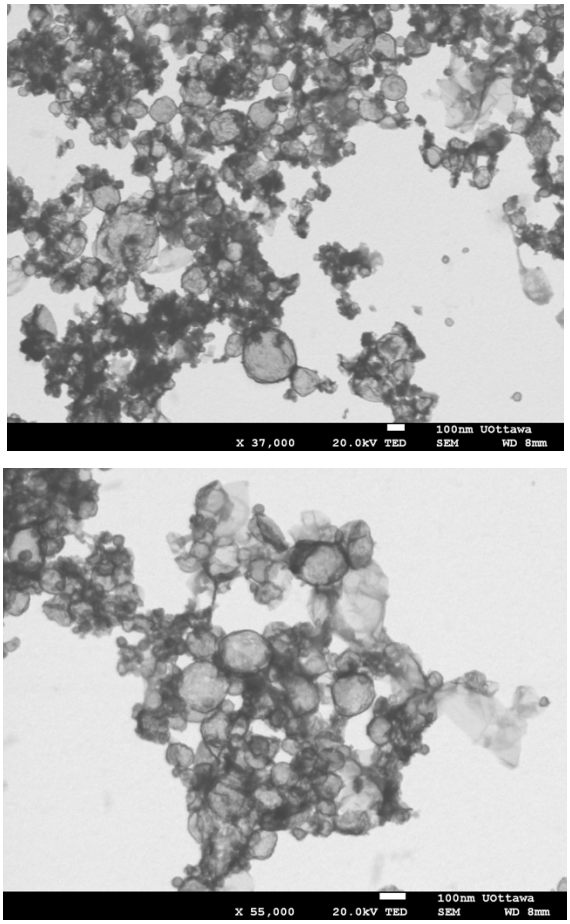

Figure 9.13 SEM pictures of the laser irradiated rGO solution in water.

After irradiation the solution presented some bubbles inside the solvent and as expected the color resulted drastically clearer. The formation of bubbles inside the solvent has also been observed by recording videos of the drop or picture of the cuvette during the laser irradiation. (Figure 9.14)

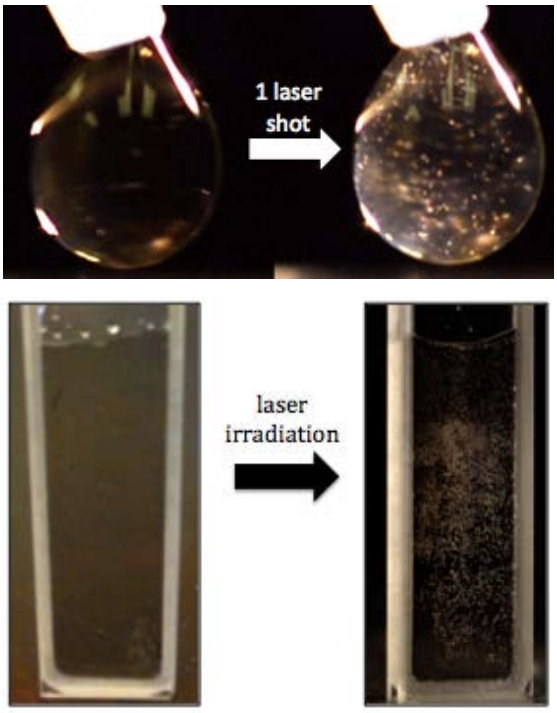

Figure 9.14. (top) Picture of the drop solution before and after 1 laser shot. (bottom) Picture of the rGO solution inside the 1 mm thick cuvette before and after 30 min of laser irradiation. The formation of bubbles inside the solution was observed in both experiments.

In order to identify what gas was being formed we repeated the irradiation using a sealed cuvette and taking aliquots of the gas portion. After the irradiation, the reaction headspace was injected into a gas chromatograph equipped with a packed column and a universal thermal conductivity detector (TCD). The injection result was compared to an injection of air. Analysis at the GC-TCD revealed that hydrogen gas, with a retention time of 4.09 min, was detected in the sample obtained after 30 min of rGO irradiation. (Figure 9.15)

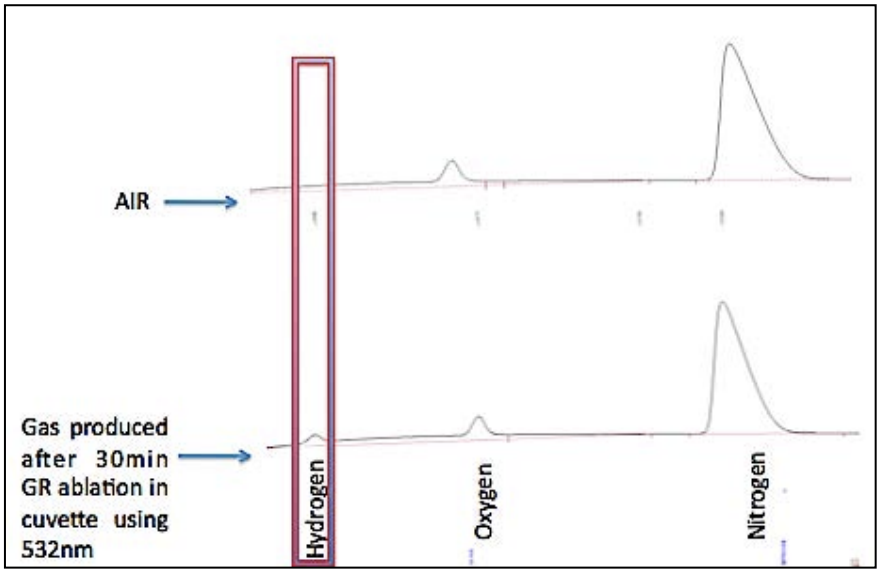

H_2 pick (4.089)	Area (μV x s)	Area %
Air sample	0	0
Gas detected after ablation	21734	2%

Figure 9.15 Comparison between gas chromatograms of an air sample and the gas produced after 30 min of rGO ablation using a 532 nm irradiation laser. H_2 areas for the two samples are reported in the table.

We were able to quantify a total amount of 13000 μmol g^{-1} h^{-1} of H_2. Two potential events could occur for the emission of H_2: the splitting of H_2O or the degradation of the rGO structure. In the first case the emission of H_2 is accompanied by the production of O_2, according to the following reaction:

$$2\ H_2O \longrightarrow 2H_2 + O_2$$

Scheme 9.1 Water spitting reaction.

On the other side, the evolution of syn gas may results from the rGO degradation, in such a way that H_2 is accompanied with the formation of CO or CO_2.

Several attempts have been made to determine which of the two events could be responsible for the H_2 formation, the most successful being the use of ^{18}O isotopically modified water. The idea behind this experiment was to monitor the release of $^{18}O_2$ or CO/CO_2 containing ^{18}O. For this purpose rGO solution in $H_2{}^{18}O$ (^{18}O 97%) was prepared in a long neck cuvette and purged with Ar for 45 min. The solution was irradiated with a 532 nm laser for 1h and the reaction headspace was analyzed using a quadrupole mass spectrometers, customized by Prof. Javier Giorgi (Chapter 2, paragraph 2.5.1). The mass analysis showed the presence of $^{18}O_2$ and the absence of any carbon oxide containing ^{18}O. The results obtained induce us to discard a possible degradation of rGO and subsequent emission of carbon oxides. Therefore, the process occurring is most likely water splitting.

As a comparison, the same experiment, using $H^{18}O$ and described in the previous paragraph, was repeated replacing the laser with a 532 nm LED irradiator system and irradiating for 1 h. From the quadrupole mass spectrometer analysis of the reaction head space no presence of ^{18}O nor CO/CO_2 containing ^{18}O was observed. In addition, when the rGO sample is irradiated with LED, its structure remains unaffected, meaning that the planar shape of the rGO is conserved. This observation led us to deduce that the gas evolution is related to the spherical rGO.

In order to strengthen this deduction, we designed an experiment based on two steps; (1) the rGO was structurally modified using 532 nm laser irradiation; (2) 532 nm LED irradiation of the spherical rGO particles was performed and the eventual gas produced was analyzed by quadrupole mass spectrometer. The first laser irradiation step was performed for 30 min, and was aimed to the modification of rGO structure from planar to spherical. After the laser irradiation, the sample was purged for 45 min with Ar to make sure that any possible gas detected after the second step was not already produced during the laser irradiation. Finally, the LED irradiation was performed for 1 h. As in the previous experiment the rGO dispersion was in $H^{18}O$.

A comparison of partial pressures of $^{18}O_2$, $C^{18}O$ and CO_2 (containing one ^{18}O) for the different experiments described is reported in Figure 9.16.

The irradiation of rGO with a 532 nm laser led to the production of ^{18}O accompanied with $C^{18}O$. The latter gas may be obtained from the partial degradation of the rGO structure due to the irradiation with the laser.

No gases containing the ^{18}O were detected in the case of the sole LED irradiation of planar rGO.

Surprisingly, within the ^{18}O labeled gases possible, an exclusive production of $^{18}O_2$ was obtained when laser irradiation followed by LED irradiation was performed in sequence. The quantification of the gases was based on their comparison with the water vapor detected after each injection. Therefore, knowing the water partial pressure at room temperature, which is 3.2 KPa, a relative quantification of the gases partial pressures could be obtained.

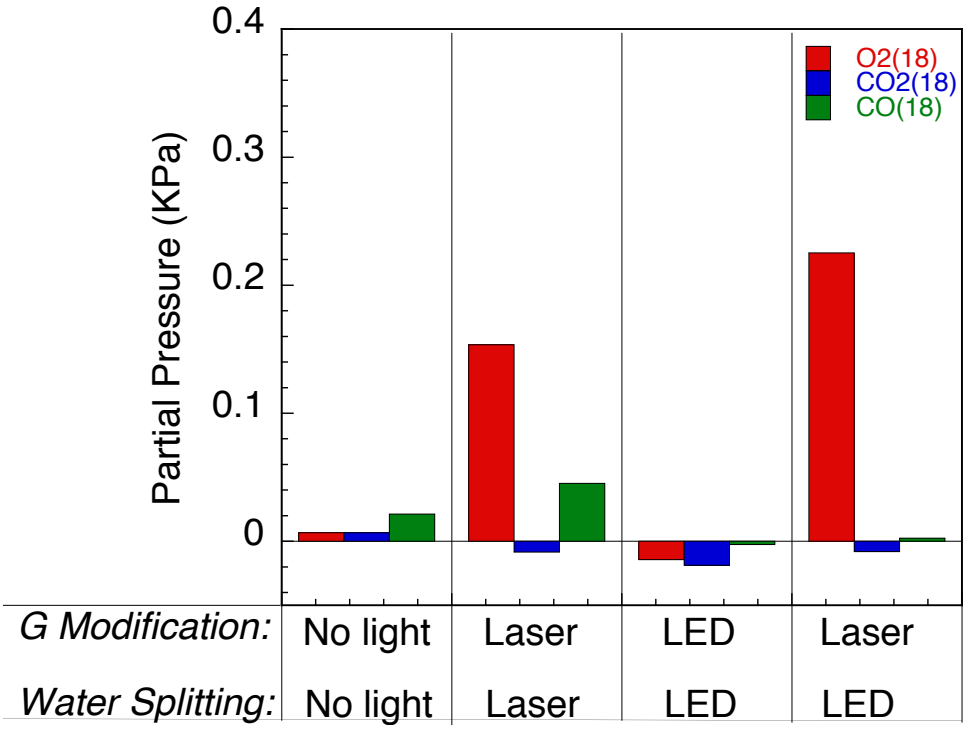

Figure 9.16 Comparison between $^{18}O_2$, C^{18}O and CO_2 (containing one ^{18}O) partial pressures of an air sample (first column); after 30 min + 30 min of laser irradiation (532 nm) of rGO (second column); after 30 min + 30 min of LED irradiation (532 nm) of rGO (third column); and after consecutive 30 min laser irradiation (532 nm) and 30 min LED irradiation (532 nm) of a rGO dispersion in H^{18}O (fourth column). The values are obtained comparing the areas of traces referred to each gas detected to the area of the trace relative to water vapor and multiplying the value obtained for the water partial pressure (3.2 KPa) at 25ºC.

Interestingly, the LED irradiation performed when the rGO was already structurally modified resulted the most efficient, giving the highest amount of $^{18}O_2$.

These results prove that our structural modification of the rGO sheets to spheres, using laser irradiation, can be promisingly used for the splitting of water. Further experiments are required to optimize the system and eventually to scale up the gas production.

9.3 Conclusion

In conclusion, the work presented herein reports the design of elemental nanoparticles and their use in different application fields. Metal nanoparticles and carbon-based materials have been morphologically modified and functionalized to achieve a better performance of their properties. Light irradiation has been employed to tune and exploit the nanomaterials properties, taking into account the convenience and the applicability of the method used. Moreover, this thesis contributed to furnish a better understating of the optical properties of metal nanoparticles, giving indication of the temperature ranges achievable after plasmon excitation, a parameter that may result useful when considering the field of applicability.

Finally, either used as catalysts, antimicrobial agents or absorbers, the results presented in this thesis gave a flavor of some of the potential use of nanomaterials.

9.4 References

(1) Jennings, D. T.; McKenzie, K. M.; Greenspan, D. C.; Clark, A. E. Quantitative Analysis of Tubule Occlusion Using NovaMin (Calcium Sodium Phosphosilicate). *Journal of Dental Research,* **2004**, Vol. 83 A.

(2) Galimberti, M. Rubber Clay Nanocomposites, Advanced Elastomers - Technology, Properties and Applications. **2012**, ISBN: 978-953-51-0739-2, InTech, DOI: 10.5772/51410.

(3) (a) Kim, J. S.; Kuk, E.; Yu, K. N.; Kim, J.-H.; Park, S. J.; Lee, H. J.; Kim, S. H.; Park, Y. K.; Park, Y. H.; Hwang, C.-Y.; Kim, Y.-K.; Lee, Y.-S.; Jeong, D. H.; Cho, M.-H. Antimicrobial Effects of Silver Nanoparticles. *Nanomedicine: Nanotechnology, Biology and Medicine***, 2007**, 3(1):95–101. (b) Schrand, A. M.; Rahman, M. F.; Hussain, S. M.; Schlager, J. J.; Smith, D. A.; Syed, A. F. Metal-Based Nanoparticles and Their Toxicity Assessment. *WIREs Nanomedicine and Nanobiotechnology*, **2010**, 2(5), 544–568.

(4) Feynman, R. P. There's Plenty of Room at the Bottom. *Journal of Microelectromechanical Systems,* **1992**, 1, 60.

(5) McGilvray, K. L.; Fasciani, C.; Bueno-Alejo, C. J.; Schwartz-Narbonne, R.; Scaiano, J. C. Photochemical Strategies for the Seed-Mediated Growth of Gold and Gold-Silver Nanoparticles. *Langmuir,* **2012**, 28, 16148−16155.

(6) Fasciani, C.; Bueno-Alejo, C. J.; Grenier, M.; Netto-Ferreira, J. C.; Scaiano, J. C. High-Temperature Organic Reactions at Room Temperature Using Plasmon Excitation: Decomposition of Dicumyl Peroxide. *Organic Letters,* **2011**, 13, 204-207.

(7) Bueno-Alejo, C. J.; Fasciani, C.; Grenier, M.; Netto-Ferreira, J. C.; Scaiano, J. C. Reduction of Resazurin to Resorufin Catalyzed by Gold Nanoparticles: Dramatic Reaction Acceleration by Laser or LED Plasmon Excitation, *Catalysis Science and Technol*ogy, **2011**, 1, 1506-1511.

(8) Stamplecoskie, K.; Fasciani, C.; Scaiano, J. C. Dual-stage Sub-wavelength Lithographic Features from a Light Driven, Plasmon Assisted Process: A Hierarchical Approach to Subwavelength Features. *Langmuir*, **2012**, 28, 10957−10961.

(9) Stamplecoskie, K.; Grenier, M.; Scaiano, J. C. Self-Assembled Dipole Nanolasers *Journal of American Chemical Society,* **2014,** dx.doi.org/10.1021/ja411696r.

(10) Simoncelli, S.; Weerasekera, H.; Fasciani, C.; Boddy, C.; Aramandia, P.; Alarcon, E. I.; Scaiano, J. C. Thermoplasmonic ssDNA Dynamic Release Revealed with High Resolution Level. (In preparation)

(11) Fasciani, C.; Garcia, H.; Scaiano, J. C. Selective Growth of Silver Nanoparticles on Graphene Oxide Mediated by Proton-Coupled Electron Transfer (PCeT). (In preparation)

(12) Scaiano, J. C.; Stamplecoskie, K. G. Can Surface Plasmon Fields Provide a New Way to Photosensitize Organic Photoreactions? From Designer Nanoparticles to Custom Applications. *Journal of Physical Chemistry Lett*ers, **2013**, 4, 1177-1187

(13) Silva, C.G.; Juarez, R.; Marino, T.; Molinari, R.; Garcia, H. Influence of Excitation Wavelength (UV or Visible Light) on the Photocatalytic Activity of Titania Containing Gold Nanoparticles for the Generation of Hydrogen or Oxygen from Water. *Journal of American Chemical Society*, **2010**, 133(3): 595–602.

(14) Hallett-Tapley, G. L.; Silvero, M. J.; Bueno-Alejo, C. J.; González-Béjar, M.; McTiernan, C. D.; Grenier, M.; Netto-Ferreira, J. C.; Scaiano, J. C. Supported Gold Nanoparticles as Efficient Catalysts in the Solventless Plasmon Mediated Oxidation of *sec*-Phenethyl and Benzyl Alcohol. *Journal of Physical Chemistry C*, **2013**, 117, 12279–12288. (b) Marin, M. L.; Hallett-Tapley, J. L.; Impellizzeri, S.; Fasciani, C.; Simoncelli, S.; Netto-Ferreira, J.C.; Scaiano, J.C. Synthesis, Acid Properties and Catalysis by Niobium Oxide Nanostructured Materials. (In preparation) (c) Fasciani, C.; McTiernan, C. D.; Hallett-Tapley, J. L.; Bueno-Alejo, C. J.; Scaiano, J.C. Efficient Oxidation of Aromatic Alcohols by Gold Nanoparticles Supported on nano-ZnO under Dark Conditions. (In preparation)

(15) (a) Seuring, J.; Agarwal, S. First Example of a Universal and Cost-Effective Approach: Polymers with Tunable Upper Critical Solution Temperature in Water and Electrolyte Solution. *Macromolecules*, **2012**, 45, 3910–3918. (b) Housini, A.; Zhao, Y. Gold Nanoparticles Functionalized with Block Copolymers Displaying Either LCST or UCST Thermosensitivity in Aqueous Solution *Langumir***, 2010**, 26 (15), 12933-12939.

(16) Gibson, M. I.; O-Reilly, R. K. To Aggregate, or Not to Aggregate? Considerations in the Design and Application of Polymeric Thermally-Responsive Nanoparticles. *Chemical Society Reviews,* **2013**, 42, 7204-7213.

(17) (a) Huang, X.; Jain, P. K.; El-Sayed, I. H.; El-Sayed, M. A. Plasmonic Photothermal Therapy Using Gold Nanoparticles. *Lasers in Medical Science,* **2008**, 23, 217- 228. (b) Li, J.-L. Gold-Nanoparticle-Enhanced Cancer Photothermal Therapy. *IEEE Journal of Selected Topics in Quantum Electronics,* **2010**, 16, 4.

(18) Picture was adapted form SEM images taken from the Centers for Disease

Control and Prevention (CDC) website. Photo credit: Carr, J. H.; McAllister, S.; Bittle, J. (1998).

(19) Schluesener, H. J.; Su, Y.; Ebrahimi, A.; Pouladsaz, D. Antimicrobial Peptides in the Brain: Neuropeptides and Amyloid. *Frontiers in Bioscience*, Scholar, **2012**, 4, 1375-1380.

(20) (a) Geim, A. K.; Novoselov, K. S., The Rise of Graphene. *Nature Materials,* **2007**, *6*, 183-191; (b) Novoselov, K. S.; Geim, A. K.; Morozov, S. V.; Jiang, D.; Zhang, Y.; Dubonos, S. V.; Grigorieva, I. V.; Firsov, A. A., Electric Field Effect in Atomically Thin Carbon Films. *Science,* **2004**, *306*, 666-669. (c) Guo, S.; Dong, S., Graphene Nanosheet: Synthesis, Molecular Engineering, Thin Film, Hybrids, and Energy and Analytical Applications. *Chemical Society Reviews,* **2011**, *40*, 2644-2672. (d) Machado, B. F.; Serp, P., Graphene-Based Materials for Catalysis. *Catalysis Science & Technology,* **2012**, *2*, 54-75. (e) Tjoa, V.; Jun, W.; Dravid, V.; Mhaisalkar, S.; Mathews, N., Hybrid Graphene–Metal Nanoparticle Systems: Electronic Properties and Gas Interaction. *Journal of Materials Chemistry,* **2011**, *21*, 15593-15599.

(21) (a) Ferrari, A. C.; Meyer, J. C.; Scardaci, V.; Casiraghi, C.; Lazzeri, M.; Mauri, F.; Piscanec, S.; Jiang, D.; Novoselov, K. S.; Roth, S.; Geim, A. K. Raman spectrum of graphene and graphene layers. *Physical Review Letters***, 2006**, 97, 187401. (b) Malard, L. M.; Pimenta, M. A.; Dresselhaus, G.; Dresselhaus, M. Raman spectroscopy in graphene. *Physics Reports,* **2009**, 473, 51-87.